Dissertation zur Erlangung des Doktorgrades
der Fakultät für Chemie und Pharmazie
der Ludwig-Maximilians-Universität München

Enhanced Photovoltaic Performance and Stability of Mixed-Dimensional Lead-based Perovskite Solar Cells through Utilization of Organic Cations

Ali SEMERCİ

aus

Altındağ, Turkey

2024

Erklärung

Diese Dissertation wurde im Sinne von § 7 der Promotionsordnung vom 28.November 2011 von Frau Prof. Dr. Tayebeh Ameri betreut von der Fakultät für Chemie und Pharmazie vertreten.

Eidesstattliche Versicherung

Diese Dissertation wurde eigenständig und ohne unerlaubte Hilfe bearbeitet.

München, 12.06.2024

_____
____

Ali SEMERCİ

Dissertation eingereicht am:	12.06.2024
Erstgutachter:	Prof. Dr. Tayebeh Ameri
Zweitgutachter:	Assoc. Prof. Saim Emin
Mündliche Prüfung am:	27.06.2024

Acknowledgement

I think sometimes people find it hardest to write down their own feelings. I really don't know how to start. Who knows how many times I have thought about when and with what feelings I would write these lines. ... Who knows what I have thought about writing. The future I've been dreaming about, the difficulties, the joy I feel when I obtain a good experimental result, and much more My memories and my imagination, my friends and my family are with me on this journey. There were people who accompanied me on this journey. What really made this journey worthwhile was their company along with my experiences and experiments. And the moments that I will never forget have left their mark on my memory. I don't want to write down the names of the people I mentioned and thank them individually because there might be someone I forgot, and I don't want to offend anyone. Instead, I would like to express my gratitude to all of you. Many of you will continue to exist for the rest of my life.

Then, I would like to thank my supervisor Prof. Dr. Tayebeh Ameri, who contributed to my journey, who provided me with all kinds of material, moral, and scientific support, Prof. Dr. Thomas Bein, who opened his laboratory to us and allowed us to experience my dream with experiments, Assoc. Prof. Saim EMIN, who always supported me in my academic development. In addition, Thank you to the entire AK BEIN group. Furthermore, I would like to thank the Study Abroad Postgraduate Education Scholarship (YLSY) awarded by the Ministry of National Education, Republic of Turkey, for providing me with financial support in this adventurous journey.

I would like to thank one person in particular: my mother. Mom, your unwavering love, support, and encouragement have been the cornerstone of my journey. You have been my confidant, and my greatest cheerleader, always believing in me even when I doubted myself. Your wisdom and guidance have shaped me into the person I am today, and for that, I am eternally grateful. Even if I were to gather all the words in the world, I could never fully express my gratitude to you for giving my life meaning and for being the incredible person you are. Thank you from the depths of my heart, Mom, for always being my greatest source of motivation. This thesis is as much a testament to your love and support as it is to my academic efforts.

Dürüstlük pahalı bir mülktür, ucuz insanlarda bulunmaz.

Hz. Ömer (R.a.)

Abstract

In conjunction with renewable energy sources, energy-efficient technologies are required to meet and reduce the global energy demand. Sunlight is the most ubiquitous and readily available member of the renewable energy sources. Present endeavors are predominately focused on photovoltaic technologies based on silicon. However, due to the inherently sluggish and energy-intensive nature of silicon deployment, the development of new technologies is urgently required.

In recent times, hybrid organic-inorganic lead-based perovskites (OIHP) have garnered significant interest in photovoltaic (PV) applications, surpassing all other semiconductor materials. This is due to their exceptional optoelectronic characteristics and straightforward synthesis processes. Solar cells composed of these materials have successfully attained power conversion efficiencies (PCE) of up to 26% in less than a decade. These materials exhibit remarkable characteristics such as direct and adjustable bandgaps, high mobility of charge carriers, and robust light absorption capabilities. The convergence of these remarkable attributes facilitates the advancement of thin-film optoelectronic devices with superior performance, which can be produced utilizing economical methodologies, particularly solution-based approaches.

On the other hand, it has been discovered that the PCE of optoelectronic devices is significantly influenced by the morphology of perovskite thin films, in addition to other factors. However, due to its low-temperature processing techniques and intrinsic chemical and structural properties, this material inevitably develops detrimental defects at both the grain boundaries (GBs), surface and bulk structure of the polycrystalline framework of the perovskite. The presence of these defects may substantially compromise the PCE and overall stability of the material.

The principal objective of this thesis was to undertake an exhaustive examination of the defects in the three-dimensional (3D) structure of methylammonium lead iodide (MAPI) perovskite materials. The presence of these defects substantially impairs the functionality and durability of PV devices constructed from such materials. To resolve these structural defects in the perovskite thin films, we investigated several prospective materials and concepts as potential remedies. The utilization of low-dimensional perovskites (LDP) within 3D MAPI perovskite structure is a strategic passivation method. By incorporating LDP, mixed-dimensional (3D/LDP) perovskite solar cells (PSCs) are designed to counteract defects in the perovskite lattice.

The first chapter of this thesis begins by outlining the theoretical foundations of the relevant

subject field. The chapter opens with an overview of semiconductors and then details into its practical applications, with a focus on solar cells. Following that, it discusses an alternate and promising material utilized in solar cells: lead-based perovskite materials. Continuing within this class, focus is on more stable subcategories, particularly low dimensional perovskite (LDP) such as 2D and 1D variations. The second chapter provides introductory information on the characterization approaches that are widely used in this field.

In chapter 3, we present the use of a new organic cation, 2-(thiophene-2yl-) pyridine-1-ium iodide (ThPyI), on the surface of 3D methylammonium lead iodide (MAPI) perovskite films and its integration into the bulk structure. ThPyI can serve as a passivator on top of 3D MAPI, fabricating surface-passivated films with a stable 1D perovskite structure formed by unreacted surface PbI_2 and organic cation, or as an additive to accomplish bulk passivated 3D MAPI. In both methods ThPyI improves PCE and increases solar cell stability. Cutting- edge characterization techniques, such as Grazing Incidence Wide-Angle X-ray Scattering (GIWAXS), show that ThPyI trigger to the preferred orientation of bulk MAPI slabs, improving charge transfer. The bulk-passivated 3D arrangement is highly stable, maintaining 84% PCE after 2000 hours of exposure without encapsulation. This paper presents novel methodologies for using organic cations with various binding patterns and passivation approaches to address faults in hybrid 3D/1D perovskite solar cells.

Finally In Chapter 4 , we utilize the formamidinium cation (FA+) employing 3,5-difluorobenzene-1-carboximidamidium iodide (2F), 4-(trifluoromethyl)benzene-1-carboximidamidium iodide (3F), and 2,3,4,5,6-pentafluorobenzene-1-carboximidamidium iodide (5F) organic spacers as passivation layer in 3D/LDP OIHP solar cells. Fluorine atom position and quantity in organic spacers change the optoelectronic characteristics of the perovskites, enhancing hydrophobicity, facilitating LDP formation, and augmenting dipole moments, thereby facilitating charge separation processes. PV performance analysis reveals that 3F-treated 3D/LDP devices achieve the highest efficiency of 19.22%. Experimental results and density functional theory (DFT) studies attribute the higher performance of 3F-modified devices to effective LDP formation, enhanced passivation of defect states at perovskite surfaces and grain boundaries, the highest dipole moment and lowest band gap among the evaluated spacers. The stability tests show that, after 1000 hours, 3F- and 5F-modified 3D/LDP OIHP devices retain over 85% of their initial efficiency. This research opens novel avenues for designing appropriate organic spacers to attenuate defects in 3D/LDP PSCs.

Table of Contents

Contents

List of Abbreviations

A	Absorbance
BSE	Back-scattered electrons
CB	Conduction band
CBM	Conduction band minimum
CIGS	Copper indium gallium selenide
DFT	Density functional theory
E	Energy
EF	Fermi level energy
Eg	Band gap energy
EK	Kinetic energy
EQE	External quantum efficiency
ETL	Electron transport layer
F	Flourine
FA	Formadinium
FF	Fill factor
FS	Forward scan
FTO	Fluorine-doped tin oxide
GBs	Grain boundaries
HI	Hysteresis index
HTL	Hole transport layer
HTM	Hole transporting material
ITO	Indium tin-oxide
J_{MPP}	Current density at maximum point
J_{sc}	Short-circuit current
J-V	Current-voltage

LDP	Low dimensional perovskite
MA	Methylammonium
MACl	Methylammonium chloride
MAPbI3	Methylammonium lead iodide
MAPI	Methylammonium lead iodide
MPP	Maximum power point
OIHPs	Organic-inorganic lead halide perovskites
Pb	Lead
PCE	Power conversion efficiency
P_{in}	incident light power
PL	Photoluminescence
PSC	Perovskite solar cell
PV	Photovoltaic
PXRD	Powder X-ray diffraction
RH	Relative humidity
RMS	Root-mean-square
RS	Reverse scan
SE	Secondary electrons
SEM	Scanning Electron Microscopy
Si	Silicon
SRH	Shockley-Read-Hall
S-Q	Schockley-Queisser
T	Transmission
TCSPC	Time-Correlated Single Photon Counting
TEM	Transmission Electron Microscopy
UPS	Ultraviolet Photoelectron Spectroscopy
UV-Vis	Ultraviolet-Visible

VBM	Valence band maximum
V_{MPP}	Voltage at maximum power point
V_{oc}	Open-circuit voltage

1. Introduction

1.1 Global Energy Market and Outlook for Solar Energy

The global energy consumption is rapidly increasing on a near-daily basis, leading to an energy crisis and environmental damage. The sustainability of energy derived from fossil fuels is at risk due to their finite and depleting reserves in the next decades, as well as its adverse environmental effects, including global warming.[1-2] As a result, the need for environmentally friendly and long-term sustainable alternative energy sources such as wind, hydrogen and solar energy is increasing day by day.

Solar power is notable among renewable energy sources due to its scalability, allowing it to be utilized on both an industrial level and for individual households. The solar energy potential is estimated to exceed 23,000 terawatt-years (TWy). Given that the global energy consumption in 2022 amounts to roughly 25.5 TWy, it is feasible to satisfy the world's energy requirements solely through solar energy.[3]

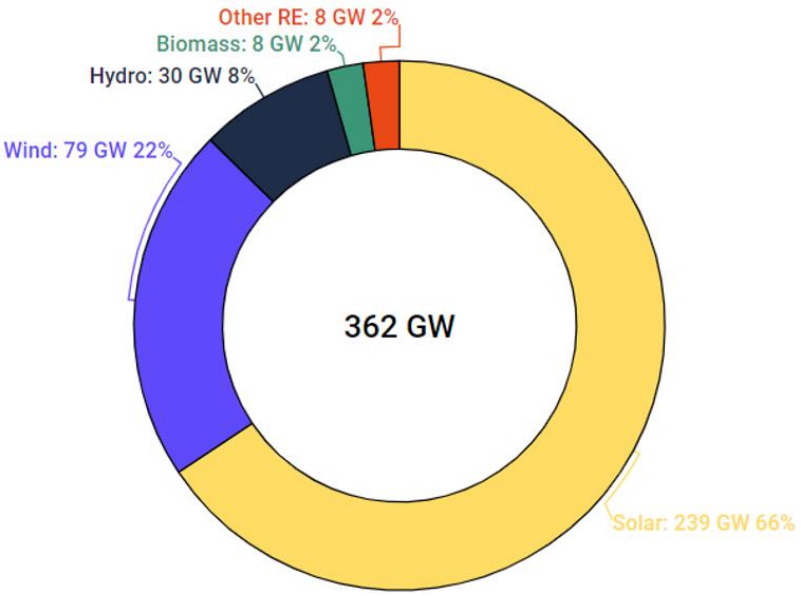

Figure 1.1 Schematic illustration of net renewable power generating quantity installed in 2022.[3]

Photovoltaics (PV) is the process by which light energy from the sun is converted immediately into electrical energy. In 2022, the worldwide cumulative capacity of photovoltaic systems attained a value of 1.18 terawatts (TW).[4] A cumulative of 362 gigawatts (GW) of additional renewable energy capacity was put into operation in 2022. The amount of energy generated from solar systems will be 239 GW in 2022, which corresponds to 66% of the total amount

generated from renewable energy sources).[5] However, solar power continues to constitute a negligible proportion of global electricity consumption, accounting for a mere 4.5% of global power generation in 2022. The percentage has exhibited a positive trajectory, increasing from 3.7% in comparison to the preceding year. The aforementioned growth rate exceeds that of alternative renewable energy sources, which, when integrated, supplied approximately 25.4% of worldwide electricity production. It is evident from these details that the increased efficiency and decreased manufacturing expenses of silicon-based solar cells have established this system as a leading PV technology.[6] Furthermore, numerous PV technologies have been developed in line with silicon solar cells over the past few decades to overcome the global energy crisis.

Second-generation thin film-based PV technologies, such as Cadmiumtelluride (CdTe) or Copper indium gallium selenide ($Cu(InGa)Se_2$ or CIGS), have been identified as very competitive alternatives to silicon (Si)-based PV.[7-8] These technologies are also compatible with scale manufacturing methods. Nevertheless, these devices are either excessively poisonous or consist of relatively scarce elements such as indium, which is far less abundant and more challenging to extract than Si, hence impeding widespread implementation.

The main reason behind the advancement of third-generation PV technologies was primarily the potential for large-scale production without the need for high-temperature annealing and high vacuum conditions during synthesis. The development of a highly efficient and solution-processable technology for solid-state thin-film PV applications using hybrid perovskite materials appears to be inevitable. The morphology and microstructure of the perovskite material exert a substantial impact on the PV performance. Hence, a comprehensive examination of their impact and subsequent optimization is imperative.

1.2 Semiconductors

The conductivity of materials is a fundamental property that determines their ability to carry an electric current. Materials are categorized based on their property of electrical conductivity, resulting in three classifications: conductors, semiconductors, and insulators.[9] The values of electrical conductivity (σ) and resistivity ($\rho = 1/\sigma$) for several materials within these three classes are shown in Figure 1.2.[10]

The initial exploration into semiconductors took place in 1874 when the rectifier, an AC-DC converter, was developed. This was achieved with the development of a prototype transistor made of germanium at Bell Labs in 1947.[11]

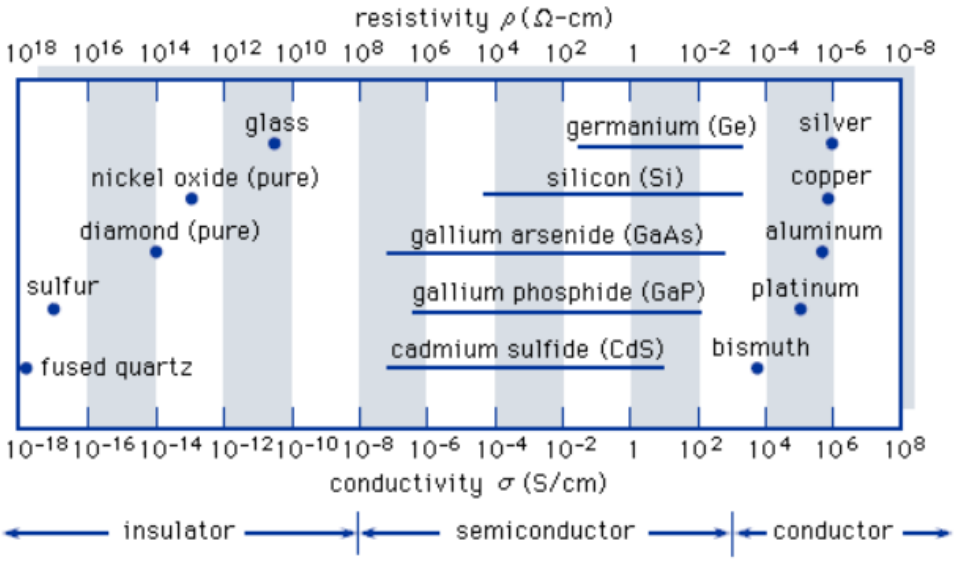

Figure 1.2 The typical range of conductivities for insulators, semiconductors, and conductors.[10]

The many characteristics of semiconductor materials have facilitated major technological advancements in the past century. Specifically, numerous implementations of semiconductor devices have emerged as the fundamental support of contemporary technology. Smartphones and computers, which contain numerous minuscule transistors composed of this substance, as well as power sources, integrated circuits, and automobiles, are just a few examples of the technology that are part of our everyday lives.

The origins of Si may be traced back to the 1960s, when it emerged as a viable substitute and effectively replaced germanium (Ge) as the predominant semiconductor material. Due to its low heat conductivity and strong thermal stability, Si is highly favored among other semiconductor materials. Furthermore, it is highly feasible to manufacture this product in significant volumes, and the capacity to achieve competitive pricing for the end product is a further noteworthy aspect in terms of cost-efficient production when compared to alternative semiconductors. Given the aforementioned characteristics, Si has become a highly researched material and Si technology has surpassed all other semiconductor technologies in terms of advancement and practicability.

1.2.1 Energy Band of Semiconductors

According to their electrical conductivity, materials were categorized as conductors, semiconductors, or insulators, as stated in the preceding section. Indeed, this categorization relies on the variations in the electronic structure properties of distinct substances, which are determined by the types of bonds (ionic, covalent, and so forth) that exist between the

constituent atoms. Put simply, the categorization of substances based on their electronic configuration is grounded in the principles of band theory.[12] It is a practical method for virtualizing their differences.

The three categories of solid materials are identified as conduction band (CB) and valence band (VB), in accordance with the principles of band theory, as illustrated in **Figure 1.3**. A region that defines energies that the electrons cannot have in the solid state separates these bands. Consequently, this area is referred to as the forbidden gap, or band gap (Eg), denoting the difference in energy levels between the conduction band minimum (CBM) and the valence band maximum (VBM).[13-14]

The Fermi level (E_F) is another significant parameter in band theory. The E_F is defined as an energy level where there is filled with electrons in a material with a probability of 50%.This energy level that are lower than this value are typically occupied by electrons, whereas levels that are higher than this number are typically unoccupied. The E_F is the highest energy level that electrons can occupy at 0 K.

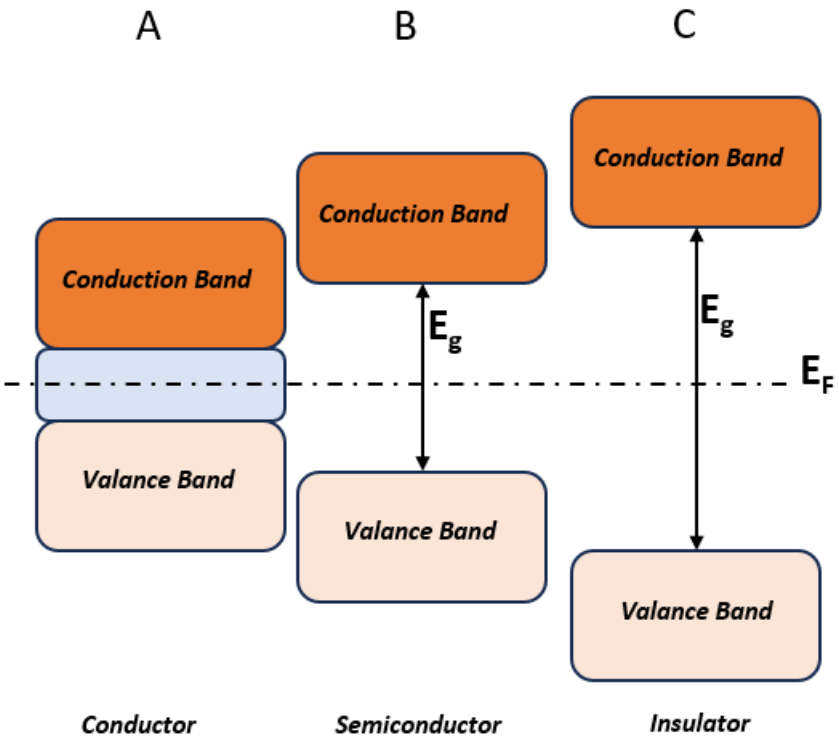

Figure 1.3 Schematic illustration of the CB and VB in a) a conductor, b) a semiconductor, and c) an insulator. The dashed area indicates the region where the VB and CB overlap in the conductor.

A material is classified as a conductor if its E_F falls within a band. Conversely, if the E_F is

located between two widely spaced bands, the substance will exhibit insulating properties. On the other hand, A material is defined as a semiconductor when the E_F falls within closely separated energy bands.[14] Figure 1.3 displays the illustration of the energy bands in these materials.

Insulators have a significant energy gap that prevents electrons from reaching the CB at standard temperatures. In contrast, conductors do not have an Eg because the VB and CB overlap, as shown by the dashed rectangular area in Figure 1.3. Unlike the principles mentioned above, semiconductors have a narrow band gap. This enables thermal energy to bridge Eg for only a minor portion of electrons, resulting in limited conductivity for the semiconductor.[15]

There are two types of semiconductors: intrinsic semiconductors and extrinsic semiconductors as depicted in Figure 1.4. An intrinsic semiconductor refers to the pure form of a semiconductor that is free from impurities. In Figure 1.4a, the E_F for the intrinsic semiconductor is positioned at the midpoint between the VB and CB. In an intrinsic semiconductor, the VB is fully occupied, whereas the CB is entirely unoccupied. They possess neither good conductivity nor insulation properties, and their ability to conduct is mostly influenced by temperature.

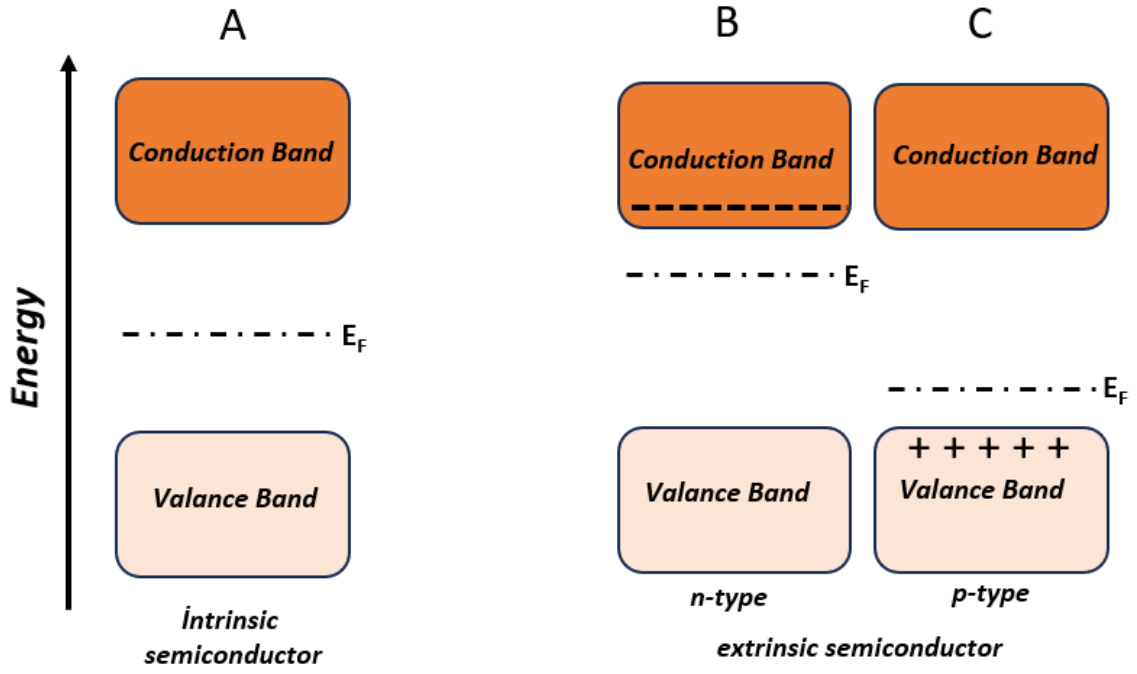

Figure 1.4 Illustration of Energy band diagram of a) intrinsic, b) n-type, and c) p-type extrinsic semiconductors.

This non-conductivity of intrinsic semiconductors can be overcome by various processes. The well-known method is doping.[16] Dopants, which are foreign compounds or impurities into

crystals, can be introduced into pure semiconductors to modify their characteristics and enhance their electrical conductivity. Semiconductors which doping material is added are called extrinsic semiconductors. Extrinsic semiconductors can be classified into two distinct categories based on the doping element: n-type and p-type semiconductors.

In n-type semiconductors, the intrinsic material is intentionally doped with V group elements (P, Bi, etc.) to introduce donor impurities. This results in the existence of unbounded extra electrons that become free to pass into the CB. In this case, the probability of an electron being in CB is higher than the probability of a hole being found in VB. Thus, E_F is positioned close to CB. In n-type semiconductors, the abundance of free electrons surpasses the number of holes by a wide margin. Consequently, the flow of current is mostly facilitated by these electrons, which are referred to as the majority charge carriers. On the other hand, holes, which are present in less quantities, act as the minority charge carriers.[16]

P-type semiconductors are doped with acceptor impurities, such as elements from the III group (B, Al, etc.), to modify the pure material. Introducing an acceptor impurity results in the generation of a significant quantity of holes within the VB. The quantity of vacancies in the VB exceeds the quantity of electrons in the CB. Therefore, the likelihood of energy levels being occupied by holes in the VB is higher than the likelihood of energy levels being occupied by electrons in the CB. Due to this rationale, the E_F is situated close to the VB. P-type materials are characterized by a majority of charge carriers in the form of holes, whereas electrons are present in smaller numbers as minority carriers.[14]

Compared to insulators, the band gap energies of standard semiconductor materials are small enough to excite electrons in PV devices with an external source such as visible light. Given this fact, the excitation of electrons from VB to CB is considered as an alternative method. The energy needed for the excitation process depends on both the characteristics and the energy level of the Eg. The bandgap's characteristics are dictated by the relative positions of the VBM and the CBM. The classification of Eg can be broadly categorized as direct and indirect, as illustrated by the energy (E)- momentum (k) diagram in Figure 1.4. The k vector represents the momentum of an electron within the semiconductor. When the two extreme points are positioned diametrically opposite one other in k space, indicating that they possess identical momentum, and the bandgap is defined as direct, as seen in Figure 1.4a, the electron can be exclusively stimulated by the incoming light from the VB to the CB without any alteration in momentum. When the two extreme points shift to each other, resulting in differing k values, an indirect bandgap is created. This indicates that the electron needs an extra change in

momentum to be excited into the CB, as depicted in Figure 1.4.b.[17] Therefore, the energy required to excite the electron in the direct bandgap semiconductors is than indirect band gap counterparts.[18]

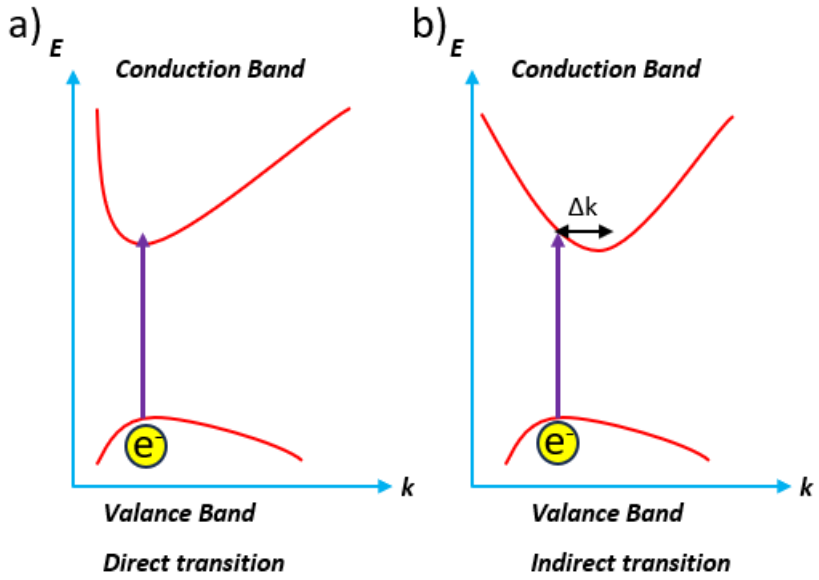

Figure 1.5 The provided diagram depicts a) direct and b) indirect bandgaps in semiconductors.

1.3 Working Principle of Solar Cells

In the year 1839, Alexandre-Edmond Becquerel was the first person to observe the PV effect. Following that, in 1946, Russell Ohl was the one who came up with the idea for the first modern solar cell that was composed of Si.[19] The term "solar cell" refers to a type of electrical device that utilizes the PV effect to transform light energy into electrical energy. A solar cell is constructed using two distinct types of semiconductors, namely p-type and n-type, which are also referred to as p-n junction semiconductors.

The process of charge separation takes place at the where n-doped and p-doped merge in standard solar cells as shown in Figure 1.6a. This occurs when photogenerated charges flow into the respective materials, thus establishing the junction. The excess electrons from the n-doped zone undergo diffusion towards the p-doped region, whereas the excess holes migrate in the opposite (reverse) direction. The electrons and holes unite at the contact area, forming an electron-hole pair, which results in the formation of a depletion region devoid of any mobile charges. The migration of electrons in the n-doped side results in the creation of the positively charged zone, while the p-doped side acquires a negative charge in the depletion region. The disparity in charge between the two entities gives rise to an electric field at the region of the

junction where mobile charges are absent. Consequently, this leads to the generation of a built-in voltage, commonly referred to as a potential difference. The fundamental importance of this built-in voltage across the junction lies in its ability to hinder the movement of both holes and electrons across the junction, which is why it is also referred to as the potential barrier. A free charge necessitates additional energy to overcome with the barrier that now obstructs its ability to pass through the depletion region. Given that the potential difference is dependent on the bandgap, it can be asserted that as the bandgap expands, the amount of energy needed for free carriers to surmount this obstacle will also rise, whereas a decrease in the bandgap will result in a drop in the required energy.[20-21] Theoretically, the (I/V) curve observed at the output of a standard solar cell is obtained by superimposing the dark responses of a diode and the photogenerated current linearly.[21]

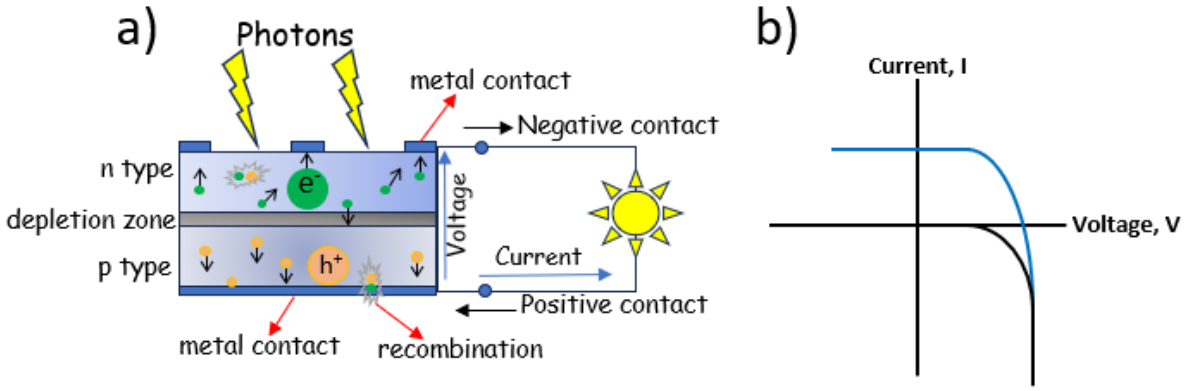

Figure 1.6 a) Illustration of working principle of standard solar cell. b) Classic I-V characteristic of a solar cell in the dark (black line) and in illumination (blue line).

In practice, the solar cell absorbs incident photons with energies greater than the Eg of the semiconductor. Consequently, the electric field creates a separation between the electron-hole pair in the depletion region. The direction of flow of the free electrons is designated by the electric field. Thus, the formed free electron reaches contact after going through the depletion region. Following its passage through the external circuit, the electron produces an electric current.[22]

So far, silicon solar cells have dominated the PV market due to their stability, the material's PCE in large-scale solar modules being already quite high, and the abundant availability of the precursor material SiO_2. Si, on the other hand, possesses an indirect bandgap that necessitates relatively thick layers for adequate absorption. This results in the demand for additional material and more stringent manufacturing techniques to attain the necessary high purity for

enough charge carrier mobility. Consequently, the fabrication process of solar cells based on Si is notably intricate and energy intensive.[23] Perovskite solar cells (PSCs) are a novel category of thin-film photovoltaics that emerged within the past decade. By virtue of being solution-processable at low temperatures, this material exhibits considerable potential in terms of cost-effectiveness, lightweight construction, and exceptional performance. Consequently, it establishes a paradigm shift in the PV industry.[24]

1.4 Perovskite Solar Cell

Organic- inorganic Halide perovskites (OIHP) have gained significant attention in the scientific community due to their potential in numerous optoelectronic applications. It has in particular launched in an epoch characterized by cost-effectiveness and superior efficiency in solar cells. Their exceptional PV performance can be attributed to their distinctive characteristics, which include long charge carrier diffusion lengths, a high charge transport mobility, and a small exciton binding energy.[25-32]

OIHP have lately made significant advancements in the field of PV. Over the past decade, perovskite solar cells (PSCs) have shown great progress in PCE compared to other thin film PV technologies.[33-35] The breakthrough made highlights the considerable potential of OIHP in the solar energy industry. The PCE of PSCs has increased significantly from 3.8% to 25.73% (certified), which brings it closer to the Shockley-Queisser (S-Q) limit (~ 31%).[36-41]

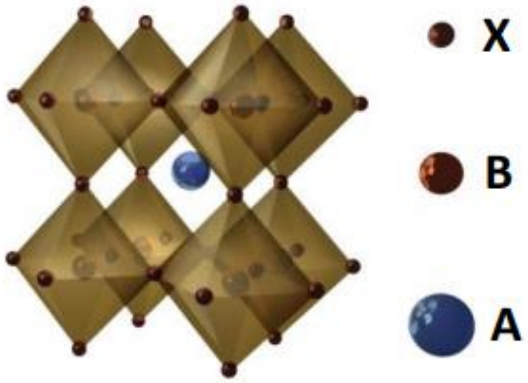

Figure 1.7 Schematic illustration of perovskite crystalline structure.[42]

The substance known as "perovskite" was called after the mineralogist Lew Alexejewitsch Petrowski and its crystal structure type, $CaTiO_3$, which was first found in 1839. The crystal structure in question typically exhibits the chemical formula ABX_3, as illustrated in Figure 1.7.

A refers to cations having a large atomic radius, such as $CH_3NH_3^+$ (MA^+), $NH_2CH{=}NH^{2+}$ (FA^+), Cs^+, whereas Pb^{2+}, Sn^{2+} are other cations with a small atomic radius. The symbols X are used to represent anions, namely Cl^-, Br^-, and I^-.[43-44] The B cation is surrounded by the X anion in an octahedral coordination arrangement through corner-sharing which form extended framework. The A cations fill the voids (cuboctahedral spaces) which are in the center of the eight corner-sharing BX_6 octahedra within the structure.[45-46]

The capacity to alter the arrangement encompasses the capability to change both positively charged ions (cations) and negatively charged ions (anions). The stability of the structure is defined by the electrostatic interactions between the positively charged cations situated at the A-site and the negatively charged framework consisting of B-X.[47]

Materials having the composition ABX_3 can exhibit many crystal forms, which are determined by the size and interaction of the A cation and the corner-sharing BX_6 octahedra. The Goldschmidt tolerance factor (t) is a dependable empirical indicator used to forecast the preferred formation of a certain structure. Additionally, it serves as an indication of the structural stability.[48] The Goldschmidt tolerance factor is determined by the ionic radii of the atoms, which may be computed using the following expression: where r_A represents the radius of the A cation, r_B represents the radius of the B cation, and r_X represents the radius of the X.

$$t = \frac{rA+rX}{\sqrt{2(rB+rX)}} \tag{1.1}$$

Materials exhibiting a tolerance factor between 0.9 and 1.0 typically possess an ideal cubic structure. Tilted octahedra constitute a distorted perovskite structure when the tolerance factor is between 0.71 and 0.9. The formation of non-perovskite structures occurs at the tolerance factor is higher (>1) or lower (<0.71).[48]

Although the rule was initially formulated for oxide perovskites, it continues to hold true for OIHP. A schematic representation of the correlation between the structure of the perovskite and the tolerance factor can be observed in Figure 1.8.[49-50] Formamidinium (FA), Cesium (Cs), and Methylammonium (MA) are the only cations in the category of perovskite materials that are regarded as "established." Additional cations such as Sodium (Na), Potassium (K), and guanidinium (GA), are seen as unsuitable for inclusion in the perovskite structure due to their dimensions being either excessively small or large as illustrated in Figure 1.8. The variation in the octahedral position and crystal structure of perovskites as a function of the Goldschmidt tolerance factor is illustrated in Figure 1.9.

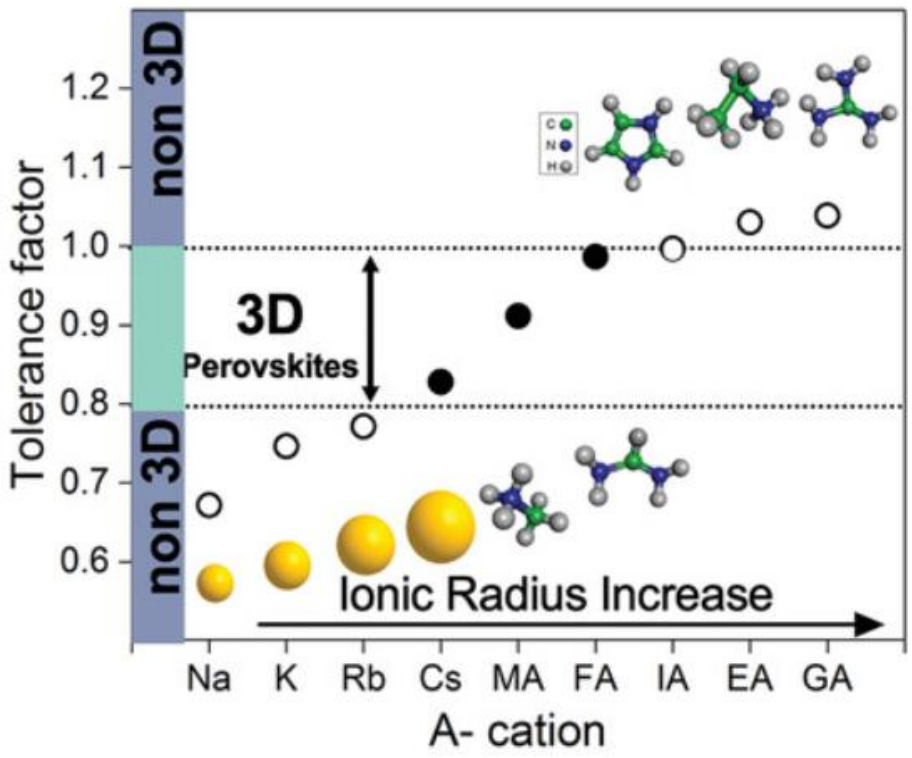

Figure 1.8 The effect of the ionic radius size of the A-site cation on the tolerance factor.[51]

PSCs are commonly organized in either a n-i-p or p-i-n configuration. The perovskite absorber, which is inherently intrinsic, is situated between a p-type hole transport layer (HTL) and an n-type electron transport layer (ETL), conductive substrate (Indium doped thin oxide (ITO) or fluorine doped tin oxide (FTO)) metal contact such as gold (Au) in this arrangement, as depicted in Figure 1.10a, b. Additionally, this arrangement may consist of a mesoporous framework, which can be of either semiconducting or insulating nature, as illustrated in Figure 1.10c.

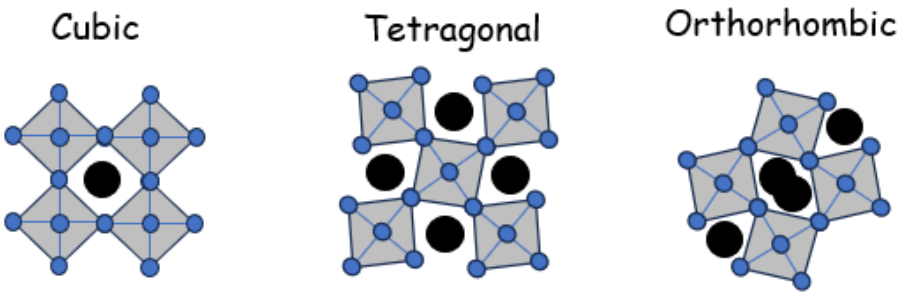

Figure 1.9 Schematic illustration of the impact of the Goldschmidt tolerance factor on the unit cell and the position of octahedra in perovskite framework.

Figure 1.11a, b illustrates a schematic energy level diagram of normal and inverted PSCs, wherein the active layer consists of methylammonium lead iodide (MAPI). An exciton is generated when solar irradiation causes an electron to jump from the VB to the CB in perovskite material, thereby leaving a positively charged electron vacancy.

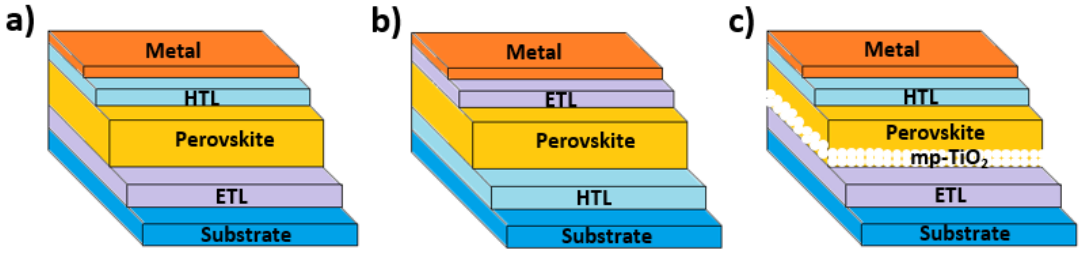

Figure 1.10 A schematic illustration of various solar cell configurations. a) a n-i-p junction, b) a p-i-n junction, c) a mesoporous structure.

The dissociation time of the exciton into a free charge carrier is relied on the electron-hole binding energy (exciton binding energy). This process can occur in picoseconds. To prevent a direct recombination of these two free charge carriers, they must be made to flow at their respective electrodes (electrons towards FTO while electron hole towards Au),as illustrated in Figure 1.11a. An analogous phenomenon is identified within the p-i-n PSCs, as illustrated in Figure 1.11b.[18]

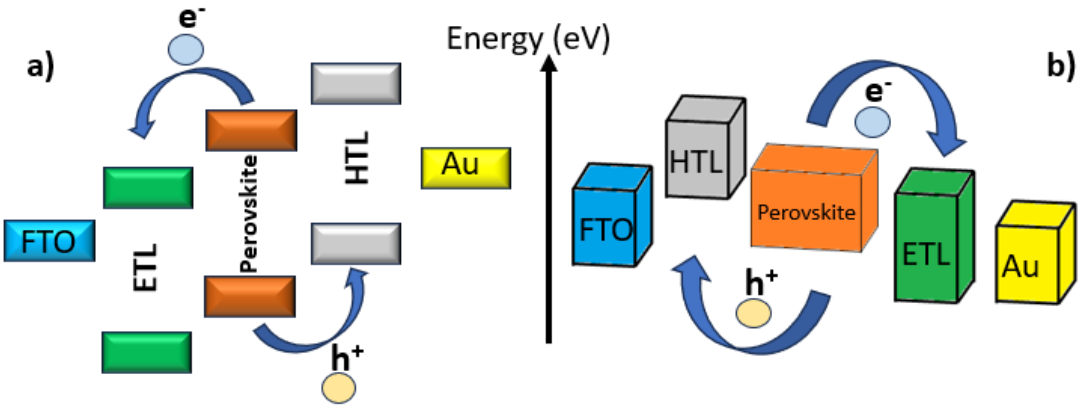

Figure 1.11 An illustrative sketch of the energy level diagram encompassing a) the n-i-p, b) p-i-n configurations within a solar cell.

To optimize charge seperation, the system utilizes charge carrier transporters to generate an energy cascade that compels the charge carriers to flow to the specified contacts. By utilizing

an ETL with a CBM situated between the CBM of the FTO contact and the perovskite, the electron is effectively routed towards the corresponding electrode. Efficient hole extraction is achieved by selecting an HTL whose energy corresponds to the VBM energy that aligns between the VBM of the perovskite and the energy of the corresponding electrode.[52]

1.5 Low-Dimensional Perovskites (LDP)

A significant impediment is the restricted composition that can be obtained from the ABX_3 perovskite structure. The Goldsmith tolerance factor imposes limitations on the selection of the organic constituent, as only three A-site cations are capable of forming reasonable stable 3D MAPI framework.[53] As a consequence, the quantity of potential configurations is considerably diminished, posing a substantial barrier to subsequent advancements.[54]

When the A cation in the 3D MAPI is replaced with large organic cations that do not fit into the interstitial space between the metal halide BX_6 octahedra, the structure is forced to form low-dimensional structure. The obtained low-dimensional phase has superior properties than its 3D MAPI counterpart.[55] Two-dimensional (2D) perovskites are the most well-known low-dimensional perovskite (LDP) structures.[56]

2D perovskite can be considered as a dimensionally reduced version of the 3D perovskite framework .The formation of 2D perovskite and its derivatives takes place by cutting along different crystallographic directions (<100>, <110>, and <111>) from 3D MAPI perovskite structure.[57-58] This process produces three distinct types of 2D perovskite families depending on the crystallographic direction of layer slicing, (100)-, (110)-, and (111)-oriented 2D perovskites. The (100)-oriented 2D perovskites are considered to be the most commonly utilized light absorbers in PSCs due to its well-aligned structure.[59] 2D perovskites are divided into an additional category called Ruddlesden-Popper (RP)-type and the Dion-Jacobson (DJ)-type perovskites, which are commonly used for materials in this group.[60-62] The classification of these two primary categories of 2D perovskites is based on the sort of organic spacer employed in their structure.

The RP and the DJ perovskites are represented by the general formulas as given $A'_2A_{n-1}B_nX_{3n+1}$ and $A''A_{n-1}B_nX_{3n+1}$ respectively. In this context, A' and A'' refer to aliphatic or aromatic alkylammonium monovalent ($R\text{-}NH_3$) and divalent ($H_3N\text{-}R\text{-}NH_3$) organic cations respectively, and act as insulating layers. They intercalate between the inorganic $A_{n-1}B_nX_{3n+1}$ 2D LDPs. A is a monovalent cation (MA^+, FA^+, etc.), B is a divalent metal cation and (Pb^{2+}, $Sn^{2+,}$ etc.), and X is a halide from the halogen group. Furthermore, the variable n denotes the thickness of the 2D

perovskite, which is determined by the quantity of corner-sharing $[BX_6]^{4-}$ octahedral inorganic layers that are sandwiched between two organic spacers.[63-70] The schematic diagram in figure 1.12 illustrates the RP and DJ types of 2D perovskite structures with a value of n equal to 2.

Furthermore, the 2D perovskite structure undergoes variation based on the value of n. When n equals 1, the structure is pure 2D. When n is between 2 and 5, the structure is quasi-2D. The value of n significantly influences the optoelectronic characteristics of 2D materials, such as exciton binding energy, charge carrier mobility, and bandgap. Hence, it is imperative to regulate the thickness of the inorganic layers. As the value of n increases, the thickness of the layer also increases. Consequently, the exciton binding energy and bandgap energy values are prone to falling. When n approaches infinity, the structure becomes a conventional 3D perovskite structure.[71-72]

The ability to tune optoelectronic properties in accordance with the thickness of the 2D RP perovskite makes this class of material favorable for PV applications. Thus, The RP phase is the most frequently examined in research. The organic cation's terminal amine forms hydrogen bonds, interacting with the halide of the inorganic layer, as well as the nearby carbon chains of the organic cations are held together by van der Waals force, thus resulting in the formation of organic layers. A Van der Waals gap is observed between neighboring inorganic octahedral layers, which is caused by the interdigitated organic spacers in the perovskite structure expansion in the interlayer gap.

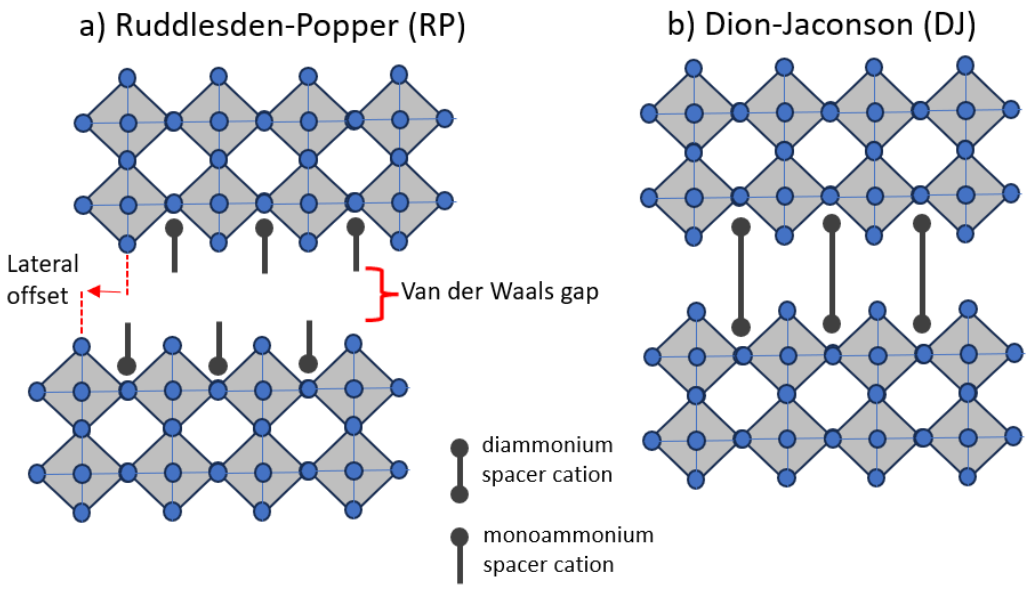

Figure 1.12 Schematic representation of RP and DJ perovskite structure.

Thus, inorganic octahedral layers are typically horizontally displaced by half an octahedral

unit, as depicted in Figure 1.12a.[73-82]

The DJ phase is less researched since there is a limited supply of easily accessible diamines.[83] The two terminal amines in DJ-type perovskite structures are connected to the inorganic layer via hydrogen bonds. The organic spacers often do not induce any lateral displacement of the inorganic octahedral layer since they form hydrogen bonds with adjacent inorganic octahedral layers as shown in figure 1.12b.[84-86]

2D perovskites often have a structure in which the perovskite layers are connected to each other via corner sharing as shown in Figure 1.13a. Nevertheless, there are rare occasions in which 2D perovskites display edge-sharing and face-sharing arrangements, as illustrated in Figure 1.13b, c.[87]The variability in connection modes can be regulated by manipulating the length of the organic amines employed in the substance which relies on the size of organic cations, enabling a level of structural flexibility and adjustability.[47]

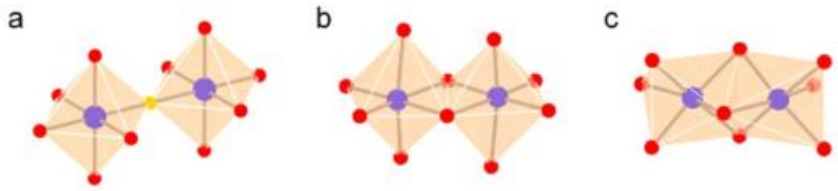

Figure 1.13 The connectivity modes in 2D perovskite are categorized into three types: (a) corner-sharing, (b) edge-sharing, and (c) face-sharing.[47]

2D perovskite structures, whether pure or quasi-2D, possess unique characteristics, such as enhanced ambient and operational device stabilities, as compared to 3D MAPI counterparts. There are some factors behind this trend such as stronger coulomb interaction between charge carriers and hydrogen bonds as well as the hydrophobic nature of large organic cations.[88] These interactions serve to shield the perovskite's surface and internal structure from degradation caused by moisture and humidity. Furthermore, the devices demonstrate enhanced thermal stability as a result of the reduced volatility of the organic cations.[89-91]

On the other hand, 2D perovskite has a higher quantum and dielectric confinement due to the incorporation of large organic cations into the structure, resulting in higher Eg and exciton binding energy.[92] The quantum confinement of carriers occurs within the perovskite crystal due to the inorganic layer acting as a "well" and the organic cation acting as a barrier.[93] This hinders the separation of charge carriers to the contacts, leading to a decline in the performance of the 2D-based PSCs.[94-95]

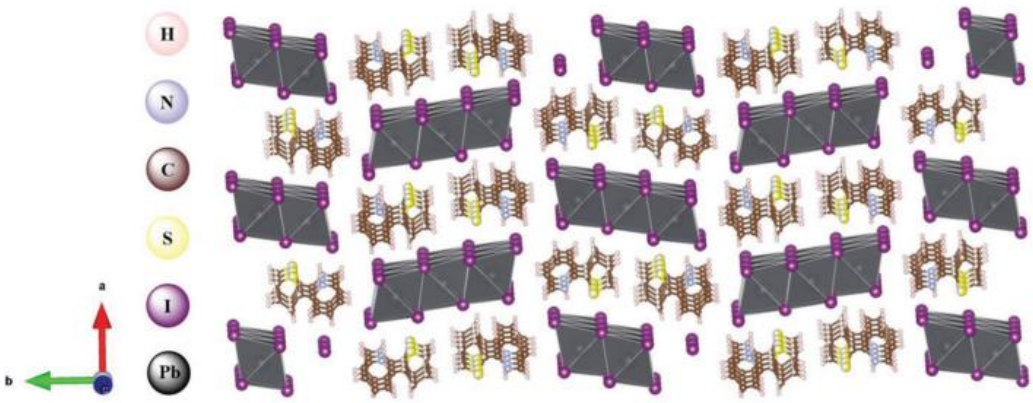

Figure 1.14 a 1D perovskitoid crystal structure serves as an illustration.[96]

Furthermore, apart from 3D and its 2D equivalents, a distinct category of organic-inorganic metal halides was discovered. These materials cannot be classified as perovskites since they do not exclusively demonstrate corner-sharing BX_6 octahedral connectivity. The compounds discussed exhibit BX_6 octahedra with either edge- and face-sharing connection patterns or a combination of corner-, edge-, and face-sharing connections patterns. These structures, as depicted in Figure 1.13b, c, do not meet the criteria to be classified as perovskites. The group of materials known as "perovskitoids" are characterized by their enhanced environmental stability, which is attributed to the stabilizing effect of the edge- and face-sharing structures on the orbital energies of $5s^2$ (Sn^{2+}) or $6s^2$ (Pb^{2+}), which are normally dominant in the VB of conventional perovskites. The 1D perovskitoid structures, such as $CsPbI_3$, exhibit greater stability compared to their analogous 3D perovskites.[97-99]

1.6 Passivation Strategy for 3D MAPI Perovskite Solar Cells

3D MAPI PSCs have garnered significant interest within the photovoltaic sector. They are a promising option for the future of the PV market due to their low cost, high efficiency, ease of processing, and versatility in various applications. This makes them a preferable choice over conventional semiconductors such as Si. Moreover, the perovskite thin-film technique has a tangible capability to come close to the theoretical efficiency limit (known as the Shockley-Queisser thermodynamic limit) for single-junction solar cells by effectively managing the optoelectronic properties.[100]

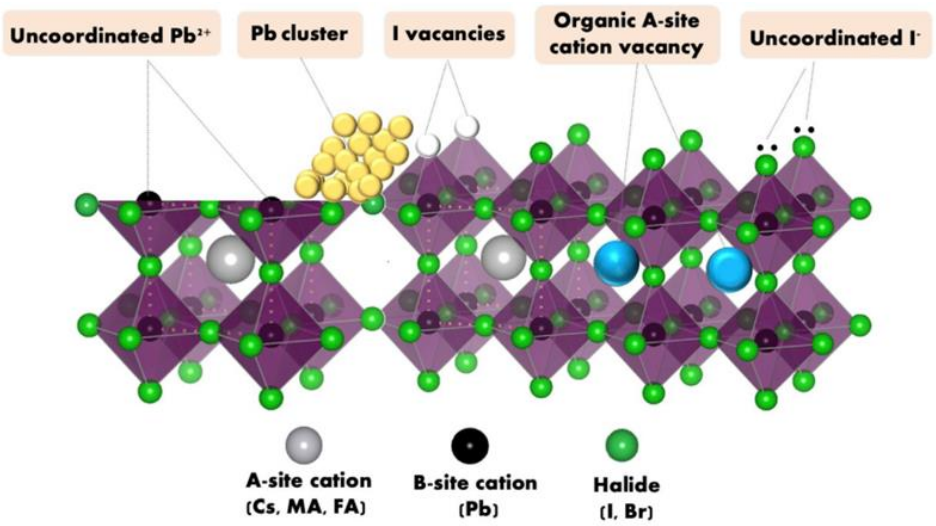

Figure 1.15 Illustration of possible defect categories in 3D MAPI.[101]

Although 3D perovskite materials have several advantages, their chemical and structural properties can lead to the development of undesirable defects on the surface and grain boundaries (GBs), and bulk structure of the 3D perovskite framework during the fabrication of solution-based low-temperature processes. These defects primarily arise from the disorder in the structure of the polycrystalline perovskite crystals, as depicted in figure 1.15. The reason for this is that they possess an ionic nature and often exhibit low activation energies for the creation of defects.[102-104] Defects in semiconductors are typically seen as harmful because they negatively affect important features of semiconductors, such as charge carrier mobility, conductivity.[105] Furthermore, the existence of chemical element vacancies or physical boundaries accelerates the deterioration of the 3D perovskite structure upon exposure to air containing humidity and oxygen. Consequently, they can degrade the PCE and long-term durability of PSCs.

The extensively researched perovskite compound, 3D MAPI exhibits a diverse range of defects. The presence of defects within the band gap of 3D MAPI perovskite leads to the creation of trap levels, which function as non-radiative recombination centers known as Shockley-Read-Hall (SRH) centers.[106] They have a detrimental impact on the mobility of charge carriers, resulting in a low open-circuit voltage (V_{oc}).[105] The defects in 3D MAPI can be categorized into two groups, shallow and deep based on their formation energies.[103] Their precise placements are dictated by the energy levels relative to the VBM or CBM.[102, 107] In the 3D MAPI concepts, point defects with low formation energies such as in the form of MA vacancy (V_{MA}) and I vacancy (V_I), MA molecules on Pb site (MA_{Pb}), I interstitials (I_i) are

depicted in Figure 1.16.[107]

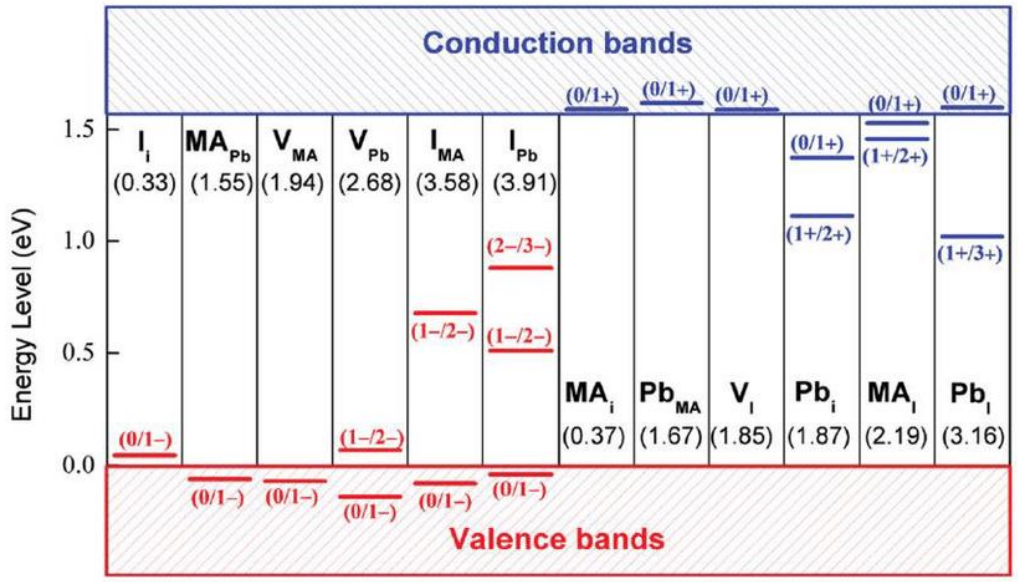

Figure 1.16 Computed the energy levels of several defects in the 3D MAPI perovskite. The formation energies of each defect type are indicated within parentheses.[107]

Given the mentioned limitations in the performance and stability of the 3D perovskite structure, passivation is identified as a highly effective approach to mitigate defects, inhibit ion migration, enhance interfacial contact, and optimize energy level alignment. This leads to improved stability and performance due to its significant impact. Through the process of passivation, the material's surface or interfaces can be treated to enhance its resistance to several variables, including moisture, oxygen, and ion migration. Passivation can be applied to bulk materials, surfaces, and GBs, depending on the specific locations and procedures used for passivation.

Passivation is the process of applying chemical compounds to defect locations on the surface or within the bulk of perovskite materials in order to repair charged defects. This interaction generates the creation of chemical bonds, which might be covalent or ionic.[108] Among these chemical compounds, the incorporation of low-dimensional perovskites (LDP) into 3D PSCs is another strategy for the passivation method. Since, introducing an insulating spacer layer to 3D perovskites provides intrinsic long-term stability due to the hydrophobic nature of organic spacers.[109]

The utilization of LDP perovskite increases the activation energy barrier for ion migration. Thus, ion migration is inhibited in the 3D perovskite structure.[110] This improves the longevity of PSCs and prevents the build-up of defects on the surface and GBs of the 3D perovskite

structure, resulting in an increased V_{oc} of the devices.[111] In addition, the application of organic cations on the surface of 3D MAPI can create a mixed-dimensional perovskite structure which consisting of LDP and 3D perovskite components. This structure acts as a barrier layer, preventing the recombination of charge carriers across the 3D/LDP perovskite.[112] The use of a LDP layer either within the bulk or on the surface of the 3D perovskite layer leads to longer lifetimes of charge carriers compared to the 3D MAPI counterparts as the defects in the 3D MAPI structure are effectively neutralized.

1.7 Outline of the Thesis

The primary objective of this thesis was to conduct extensive investigation into the defects that manifest at the GBs, surface, and bulk structure of lead- based 3D MAPI perovskite frameworks. The above-mentioned defects significantly impair the PCE, and stability of PV devices constructed from such materials. To mitigate the impact of these defects, we investigated a range of materials and concepts. Among these concepts, detailed research has been conducted on the incorporation of low-dimensional perovskite (LDP) structure into the 3D MAPI framework. The advantages of two different perovskite types are combined in the 3D/LDP PSCs and they are fabricated to reduce defects in the perovskite-based PV device. Thus, the performance and stability of 3D/LDP PSCs are enhanced.

Chapter 3 of the thesis, the utilization of a new organic cation called 2-(thiophene-2yl-) pyridine-1-ium iodide (ThPyI) is demonstrated. This cation is applied to the surface of 3D MAPI perovskite films as well as within its bulk structure. ThPyI is employed for two purposes: firstly, as a passivator to generate surface passivated films on top of 3D MAPI, resulting in the formation of stable 1D perovskite phase; secondly, as a byproduct of the unreacted surface PbI_2 and organic cation, or added separately into the 3D MAPI precursor to achieve bulk passivation.

Chapter 4 of the thesis, the utilization of 3,5-difluorobenzene-1-carboximidamidium iodide (2F), 4-(trifluoromethyl)benzene-1-carboximidamidium iodide (3F), and 2,3,4,5,6-pentafluorobenzene-1-carboximidamidium iodide (5F) organic cations. They fulfilled a dual function in the perovskite structure. These corresponding organic spacers are employed as passivation agents and interact with PbI_2 to fabricate mixed dimensional 3D/LDP MAPI PSCs.

1.8 References

[1] KRISHNAN, Suresh Kumar; KANDASAMY, Senthilkumar; SUBBIAH, Kavitha. Fabrication of microbial fuel cells with nanoelectrodes for enhanced bioenergy production. In: *Nanomaterials*. Academic Press, 2021. p. 677-687.

[2] HÖÖK, Mikael; TANG, Xu. Depletion of fossil fuels and anthropogenic climate change—A review. *Energy policy*, 2013, 52: 797-809.

[3] https://www.freeingenergy.com/the-earth-gets-more-solar-energy-in-one-hour-than-the-entire-world-uses-in-a-year/ (Rev: 01.01.2024)

[4] https://www.pv-tech.org/global-installed-pv-capacity-passes-1-18tw-iea/(Rev: 01.01.2024)

[5] https://www.solarpowereurope.org/insights/outlooks/global-market-outlook-for-solar-power-2023-2027/detail (Rev: 01.01.2024)

[6] GREEN, Martin A. Commercial progress and challenges for photovoltaics. *Nature Energy*, 2016, 1.1: 1-4.

[7] SADHANALA, Aditya, et al. Preparation of single-phase films of CH3NH3Pb (I1–x Br x) 3 with sharp optical band edges. *The Journal of Physical Chemistry Letters*, 2014, 5.15: 2501-2505.

[8] JACKSON, Philip, et al. Effects of heavy alkali elements in Cu (In, Ga) Se2 solar cells with efficiencies up to 22.6%. *physica status solidi (RRL)–Rapid Research Letters*, 2016, 10.8: 583-586.

[9] HUMMEL, Rolf E.; HUMMEL, Rolf E. Electrical properties of materials. *Understanding Materials Science: History· Properties· Applications*, 1998, 180-216.

[10] https://www.britannica.com/science/semiconductor (Rev: 01.01.2024)

[11] RIORDAN, Michael; HODDESON, Lillian; HERRING, Conyers. The invention of the transistor. *Reviews of Modern Physics*, 1999, 71.2: S336.

[12] AL-OQLA, Faris M., et al. Natural fiber reinforced conductive polymer composites as functional materials: A review. *Synthetic Metals*, 2015, 206: 42-54.

[13] BLAKEMORE, John Sydney. *Semiconductor statistics*. Courier Corporation, 2002.

[14] M FIORE, James. *Semiconductor Devices: Theory and Application*. dissidents, 2017.

[15] PANTELIDES, Sokrates T. The electronic structure of impurities and other point defects in semiconductors. *Reviews of Modern Physics*, 1978, 50.4: 797.

[16] ORTON, John W. *The story of semiconductors*. OUP Oxford, 2008.

[17] WÜRFEL, Peter; WÜRFEL, Uli. *Physics of solar cells: from basic principles to advanced*

concepts. John Wiley & Sons, 2016.

[18] TRESS, Wolfgang; TRESS, Wolfgang. Photovoltaic Energy Conversion. *Organic Solar Cells: Theory, Experiment, and Device Simulation*, 2014, 15-65.

[19] YADAV, A.; KUMAR, P.; RPSGOI, M. Enhancement in efficiency of PV cell through P&O algorithm. *International Journal for Technological Research in Engineering*, 2015, 2.11: 2642-2646.

[20] GINLEY, David S.; CAHEN, David (ed.). *Fundamentals of materials for energy and environmental sustainability*. Cambridge university press, 2011.

[21] SHAH, Arvind, et al. Photovoltaic technology: the case for thin-film solar cells. *science*, 1999, 285.5428: 692-698.

[22] SRINIVAS, B., et al. Review on present and advance materials for solar cells. *International Journal of Engineering Research-Online*, 2015, 3.2015: 178-182.

[23] GRÄTZEL, Michael. Photoelectrochemical cells. *nature*, 2001, 414.6861: 338-344.

[24] SNAITH, Henry J., et al. Anomalous hysteresis in perovskite solar cells. *The journal of physical chemistry letters*, 2014, 5.9: 1511-1515.

[25] SHAO, Ming, et al. Over 21% efficiency stable 2D perovskite solar cells. *Advanced Materials*, 2022, 34.1: 2107211.

[26] DE WOLF, Stefaan, et al. Organometallic halide perovskites: sharp optical absorption edge and its relation to photovoltaic performance. *The journal of physical chemistry letters*, 2014, 5.6: 1035-1039.

[27] PARK, Nam-Gyu. Perovskite solar cells: an emerging photovoltaic technology. *Materials today*, 2015, 18.2: 65-72.

[28] ZHANG, W. E. I., et al. Enhancement of perovskite-based solar cells employing core–shell metal nanoparticles. *Nano letters*, 2013, 13.9: 4505-4510.

[29] PONSECA JR, Carlito S., et al. Organometal halide perovskite solar cell materials rationalized: ultrafast charge generation, high and microsecond-long balanced mobilities, and slow recombination. *Journal of the American Chemical Society*, 2014, 136.14: 5189-5192.

[30] STOUMPOS, Constantinos C.; MALLIAKAS, Christos D.; KANATZIDIS, Mercouri G. Semiconducting tin and lead iodide perovskites with organic cations: phase transitions, high mobilities, and near-infrared photoluminescent properties. *Inorganic chemistry*, 2013, 52.15: 9019-9038.

[31] XING, Guichuan, et al. Long-range balanced electron-and hole-transport lengths in organic-inorganic CH3NH3PbI3. *Science*, 2013, 342.6156: 344-347.

[32] STRANKS, Samuel D., et al. Electron-hole diffusion lengths exceeding 1 micrometer in

an organometal trihalide perovskite absorber. *Science*, 2013, 342.6156: 341-344.

[33] SALIBA, Michael, et al. Cesium-containing triple cation perovskite solar cells: improved stability, reproducibility and high efficiency. *Energy & environmental science*, 2016, 9.6: 1989-1997.

[34] YANG, Woon Seok, et al. Iodide management in formamidinium-lead-halide–based perovskite layers for efficient solar cells. *Science*, 2017, 356.6345: 1376-1379.

[35] SHIN, Seong Sik, et al. Colloidally prepared La-doped BaSnO3 electrodes for efficient, photostable perovskite solar cells. *Science*, 2017, 356.6334: 167-171.

[36] KOJIMA, Akihiro, et al. Organometal halide perovskites as visible-light sensitizers for photovoltaic cells. *Journal of the american chemical society*, 2009, 131.17: 6050-6051.

[37] PARK, Jaewang, et al. Controlled growth of perovskite layers with volatile alkylammonium chlorides. *Nature*, 2023, 616.7958: 724-730.

[38] TAN, Hairen, et al. Efficient and stable solution-processed planar perovskite solar cells via contact passivation. *Science*, 2017, 355.6326: 722-726.

[39] ZHOU, Huanping, et al. Interface engineering of highly efficient perovskite solar cells. *Science*, 2014, 345.6196: 542-546.

[40] LI, Xiong, et al. A vacuum flash–assisted solution process for high-efficiency large-area perovskite solar cells. *Science*, 2016, 353.6294: 58-62.

[41] KIM, Hui-Seon, et al. Lead iodide perovskite sensitized all-solid-state submicron thin film mesoscopic solar cell with efficiency exceeding 9%. *Scientific reports*, 2012, 2.1: 591.

[42] GHARIBZADEH, Saba. *2D/3D Heterostructure Wide-Bandgap Perovskite Solar Cells for Efficient Tandem Photovoltaics*. 2022. PhD Thesis. Dissertation, Karlsruhe, Karlsruher Institut für Technologie (KIT), 2022.

[43] BORRIELLO, Ivo; CANTELE, Giovanni; NINNO, Domenico. Ab initio investigation of hybrid organic-inorganic perovskites based on tin halides. *Physical Review B*, 2008, 77.23: 235214.

[44] LI, Hui; ZHANG, Wei. Perovskite tandem solar cells: from fundamentals to commercial deployment. *Chemical Reviews*, 2020, 120.18: 9835-9950.

[45] JENA, Ajay Kumar; KULKARNI, Ashish; MIYASAKA, Tsutomu. Halide perovskite photovoltaics: background, status, and future prospects. *Chemical reviews*, 2019, 119.5: 3036-3103.

[46] WU, Yuxiang, et al. Organic–inorganic hybrid CH3NH3 PbI3 perovskite materials as channels in thin-film field-effect transistors. *RSC advances*, 2016, 6.20: 16243-16249.

[47] MAO, Lingling; STOUMPOS, Constantinos C.; KANATZIDIS, Mercouri G. Two-

dimensional hybrid halide perovskites: principles and promises. *Journal of the American Chemical Society*, 2018, 141.3: 1171-1190.

[48] GOLDSCHMIDT, Victor Moritz. Die gesetze der krystallochemie. *Naturwissenschaften*, 1926, 14.21: 477-485.

[49] KIESLICH, Gregor; SUN, Shijing; CHEETHAM, Anthony K. Solid-state principles applied to organic–inorganic perovskites: new tricks for an old dog. *Chemical Science*, 2014, 5.12: 4712-4715.

[50] LI, Zhen, et al. Stabilizing perovskite structures by tuning tolerance factor: formation of formamidinium and cesium lead iodide solid-state alloys. *Chemistry of Materials*, 2016, 28.1: 284-292.

[51] HOYE, Robert LZ, et al. The role of dimensionality on the optoelectronic properties of oxide and halide perovskites, and their halide derivatives. *Advanced Energy Materials*, 2022, 12.4: 2100499.

[52] KUMAWAT, Naresh K.; GUPTA, Dhritiman; KABRA, Dinesh. Recent advances in metal halide-based perovskite light-emitting diodes. *Energy Technology*, 2017, 5.10: 1734-1749.

[53] STOUMPOS, Constantinos C.; KANATZIDIS, Mercouri G. The renaissance of halide perovskites and their evolution as emerging semiconductors. *Accounts of chemical research*, 2015, 48.10: 2791-2802.

[54] BLANCON, J.-C., et al. Scaling law for excitons in 2D perovskite quantum wells. *Nature communications*, 2018, 9.1: 2254.

[55] HU, Jun; YAN, Liang; YOU, Wei. Two-dimensional organic–inorganic hybrid perovskites: a new platform for optoelectronic applications. *Advanced Materials*, 2018, 30.48: 1802041.

[56] KIM, Eun-Bi, et al. A review on two-dimensional (2D) and 2D-3D multidimensional perovskite solar cells: Perovskites structures, stability, and photovoltaic performances. *Journal of Photochemistry and Photobiology C: Photochemistry Reviews*, 2021, 48: 100405.

[57] XIANG, Huimin, et al. Two-dimensional Dion-Jacobson halide perovskites as new-generation light absorbers for perovskite solar cells. *Renewable and Sustainable Energy Reviews*, 2022, 166: 112614.

[58] DOHNER, Emma R.; HOKE, Eric T.; KARUNADASA, Hemamala I. Self-assembly of broadband white-light emitters. *Journal of the American Chemical Society*, 2014, 136.5: 1718-1721.

[59] XIANG, Huimin, et al. Two-dimensional Dion-Jacobson halide perovskites as new-

generation light absorbers for perovskite solar cells. *Renewable and Sustainable Energy Reviews*, 2022, 166: 112614.

[60] MAO, Lingling, et al. Hybrid Dion–Jacobson 2D lead iodide perovskites. *Journal of the American Chemical Society*, 2018, 140.10: 3775-3783.

[61] LI, Xiaotong; HOFFMAN, Justin M.; KANATZIDIS, Mercouri G. The 2D halide perovskite rulebook: how the spacer influences everything from the structure to optoelectronic device efficiency. *Chemical reviews*, 2021, 121.4: 2230-2291.

[62] STOUMPOS, Constantinos C., et al. Ruddlesden–Popper hybrid lead iodide perovskite 2D homologous semiconductors. *Chemistry of Materials*, 2016, 28.8: 2852-2867

[63] ORTIZ-CERVANTES, Carmen; CARMONA-MONROY, Paulina; SOLIS-IBARRA, Diego. Two-dimensional halide perovskites in solar cells: 2D or not 2D?. *ChemSusChem*, 2019, 12.8: 1560-1575.

[64] YAN, Jielin, et al. Recent progress in 2D/quasi-2D layered metal halide perovskites for solar cells. *Journal of Materials Chemistry A*, 2018, 6.24: 11063-11077.

[65] CAO, Duyen H., et al. 2D homologous perovskites as light-absorbing materials for solar cell applications. *Journal of the American Chemical Society*, 2015, 137.24: 7843-7850.

[66] LU, Di, et al. Thiophene-based two-dimensional Dion–Jacobson perovskite solar cells with over 15% efficiency. *Journal of the American Chemical Society*, 2020, 142.25: 11114-11122.

[67] ZHAO, Jinbo, et al. Dimensional tuning in lead-free Tin Halide perovskite for solar cells. *Advanced Energy Materials*, 2023, 13.13: 2204233.

[68] ZHOU, Ning, et al. Exploration of crystallization kinetics in quasi two-dimensional perovskite and high performance solar cells. *Journal of the American Chemical Society*, 2018, 140.1: 459-465.

[69] YUAN, Mingjian, et al. Perovskite energy funnels for efficient light-emitting diodes. *Nature nanotechnology*, 2016, 11.10: 872-877.

[70] CHEN, Yani, et al. 2D Ruddlesden–Popper perovskites for optoelectronics. *Advanced Materials*, 2018, 30.2: 1703487.

[71] HU, Jun; YAN, Liang; YOU, Wei. Two-dimensional organic–inorganic hybrid perovskites: a new platform for optoelectronic applications. *Advanced Materials*, 2018, 30.48: 1802041.

[72] HU, Yinghong, et al. Identifying and controlling phase purity in 2D hybrid perovskite thin films. *Journal of materials chemistry A*, 2018, 6.44: 22215-22225.

[73] GAO, Xupeng, et al. Ruddlesden–popper perovskites: synthesis and optical properties for

optoelectronic applications. *Advanced Science*, 2019, 6.22: 1900941.

[74] SAPAROV, Bayrammurad; MITZI, David B. Organic–inorganic perovskites: structural versatility for functional materials design. *Chemical reviews*, 2016, 116.7: 4558-4596.

[75] TILLEY, Richard JD. *Perovskites: structure-property relationships*. John Wiley & Sons, 2016.

[76] GHOSH, Dibyajyoti, et al. Charge carrier dynamics in two-dimensional hybrid perovskites: Dion–Jacobson vs. Ruddlesden–Popper phases. *Journal of Materials Chemistry A*, 2020, 8.42: 22009-22022.

[77] LENG, Kai, et al. Electron tunneling at the molecularly thin 2D perovskite and graphene van der Waals interface. *Nature Communications*, 2020, 11.1: 5483.

[78] WANG, Yiping, et al. Two-dimensional van der Waals epitaxy kinetics in a three-dimensional perovskite halide. *Crystal Growth & Design*, 2015, 15.10: 4741-4749.

[79] WANG, Yiping, et al. Band gap engineering of a soft inorganic compound PbI2 by incommensurate van der Waals epitaxy. *Applied Physics Letters*, 2016, 108.1.013105

[80] BLANCON, Jean-Christophe, et al. Semiconductor physics of organic–inorganic 2D halide perovskites. *Nature nanotechnology*, 2020, 15.12: 969-985.

[81] ZHANG, Fei, et al. Advances in two-dimensional organic–inorganic hybrid perovskites. *Energy & Environmental Science*, 2020, 13.4: 1154-1186.

[82] LU, Di, et al. Thiophene-based two-dimensional Dion–Jacobson perovskite solar cells with over 15% efficiency. *Journal of the American Chemical Society*, 2020, 142.25: 11114-11122.

[83] SIRBU, Dumitru, et al. Layered perovskites in solar cells: structure, optoelectronic properties, and device design. *Advanced Energy Materials*, 2021, 11.24: 2003877.

[84] ZHU, Mingzhe, et al. Interaction engineering in organic–inorganic hybrid perovskite solar cells. *Materials Horizons*, 2020, 7.9: 2208-2236.

[85] ZHANG, Fei, et al. Advances in two-dimensional organic–inorganic hybrid perovskites. *Energy & Environmental Science*, 2020, 13.4: 1154-1186.

[86] AHMAD, Sajjad, et al. Dion-Jacobson phase 2D layered perovskites for solar cells with ultrahigh stability. *Joule*, 2019, 3.3: 794-806.

[87] KAMMINGA, Machteld E., et al. Confinement effects in low-dimensional lead iodide perovskite hybrids. *Chemistry of materials*, 2016, 28.13: 4554-4562.

[88] STOUMPOS, Constantinos C., et al. Ruddlesden–Popper hybrid lead iodide perovskite 2D homologous semiconductors. *Chemistry of Materials*, 2016, 28.8: 2852-2867.

[89] LIU, Guozhen, et al. Introduction of hydrophobic ammonium salts with halogen functional groups for high-efficiency and stable 2D/3D perovskite solar cells. *Advanced Functional Materials*, 2019, 29.47: 1807565.

[90] SMITH, Ian C., et al. A layered hybrid perovskite solar-cell absorber with enhanced moisture stability. *Angewandte Chemie International Edition*, 2014, 53.42: 11232-11235.

[91] QUAN, Li Na, et al. Ligand-stabilized reduced-dimensionality perovskites. *Journal of the American Chemical Society*, 2016, 138.8: 2649-2655.

[92] MAHMUD, Md Arafat, et al. Origin of efficiency and stability enhancement in high-performing mixed dimensional 2D-3D perovskite solar cells: a review. *Advanced Functional Materials*, 2022, 32.3: 2009164.

[93] HUANG, Yuqiong, et al. 2D or not 2D? Selectively formed low-dimensional perovskitoids based on chiral organic cation to passivate perovskite solar cells. *Applied Materials Today*, 2022, 28: 101550.

[94] ETGAR, Lioz. The merit of perovskite's dimensionality; can this replace the 3D halide perovskite?. *Energy & Environmental Science*, 2018, 11.2: 234-242.

[95] STRAUS, Daniel B.; KAGAN, Cherie R. Electrons, excitons, and phonons in two-dimensional hybrid perovskites: connecting structural, optical, and electronic properties. *The journal of physical chemistry letters*, 2018, 9.6: 1434-1447.

[96] SEMERCI, Ali, et al. A Novel Multi-Functional Thiophene-Based Organic Cation as Passivation, Crystalline Orientation, and Organic Spacer Agent for Low-Dimensional 3D/1D Perovskite Solar Cells. *Advanced Optical Materials*, 2023, 11.16: 2300267.

[97] STOUMPOS, Constantinos C., et al. Structure–band gap relationships in hexagonal polytypes and low-dimensional structures of hybrid tin iodide perovskites. *Inorganic chemistry*, 2017, 56.1: 56-73.

[98] CHUNG, In, et al. CsSnI3: semiconductor or metal? High electrical conductivity and strong near-infrared photoluminescence from a single material. High hole mobility and phase-transitions. *Journal of the american chemical society*, 2012, 134.20: 8579-8587.

[99] GAO, Lili, et al. Improved environmental stability and solar cell efficiency of (MA, FA) PbI3 perovskite using a wide-band-gap 1D thiazolium lead iodide capping layer strategy. *ACS Energy Letters*, 2019, 4.7: 1763-1769.

[100] YAN, Jin, et al. Progress and challenges on scaling up of perovskite solar cell technology. *Sustainable Energy & Fuels*, 2022, 6.2: 243-266.

[101] LU, Haizhou, et al. Compositional and interface engineering of organic-inorganic lead halide perovskite solar cells. *Iscience*, 2020, 23.8.

[102] SRIVASTAVA, Saurabh, et al. Advanced spectroscopic techniques for characterizing defects in perovskite solar cells. *Communications Materials*, 2023, 4.1: 52.

[103] SAIDAMINOV, Makhsud I., et al. Planar-integrated single-crystalline perovskite photodetectors. *Nature communications*, 2015, 6.1: 8724.

[104] ONO, Luis K.; LIU, Shengzhong; QI, Yabing. Reducing detrimental defects for high-performance metal halide perovskite solar cells. *Angewandte Chemie International Edition*, 2020, 59.17: 6676-6698.

[105] LIU, Congcong, et al. Deep and shallow level defect passivation via fluoromethyl phosphonate for high performance air-processed perovskite solar cells. *Nano Energy*, 2023, 118: 108990.

[106] DUAN, Hsin-Sheng, et al. The identification and characterization of defect states in hybrid organic–inorganic perovskite photovoltaics. *Physical chemistry chemical physics*, 2015, 17.1: 112-116.

[107] YIN, Wan-Jian; SHI, Tingting; YAN, Yanfa. Unique properties of halide perovskites as possible origins of the superior solar cell performance. *Advanced materials (Deerfield Beach, Fla.)*, 2014, 26.27: 4653-4658.

[108] AKIN, Seckin, et al. New strategies for defect passivation in high-efficiency perovskite solar cells. *Advanced Energy Materials*, 2020, 10.13: 1903090.

[109] LIU, Guozhen, et al. Efficient solar cells with enhanced humidity and heat stability based on benzylammonium–caesium–formamidinium mixed-dimensional perovskites. *Journal of Materials Chemistry A*, 2018, 6.37: 18067-18074.

[110] HUANG, Ziru, et al. Suppressed ion migration in reduced-dimensional perovskites improves operating stability. *ACS Energy Letters*, 2019, 4.7: 1521-1527.

[111] MEGGIOLARO, Daniele; MOSCONI, Edoardo; DE ANGELIS, Filippo. Formation of surface defects dominates ion migration in lead-halide perovskites. *ACS Energy Letters*, 2019, 4.3: 779-785. [112] CHO, Kyung Taek, et al. Selective growth of layered perovskites for stable and efficient photovoltaics. *Energy & Environmental Science*, 2018, 11.4: 952-959.

2. Characterization Techniques

2.1 X-Ray Diffraction (XRD)

The principal technique employed for the analysis of the atomic structure and composition of crystalline substances is X-ray diffraction (XRD). It provides substantial insights into phase identification and crystallite sizes. X-ray diffraction (XRD) measurements rely on the scattering of electromagnetic waves, specifically X-rays, on structures in Ångstrøm range (10^{-10} m).

X-rays are commonly produced by the collision of high-velocity electrons, which are accelerated by several kilovolts (kV) in a cathode ray tube, with a metallic anode. Subsequently, the target object (generally Cu, Mo, etc.) undergoes an electron bombardment. After that, electrons in the target material which are in the ground state are forced out, leading to the creation of holes. X-ray emission occurs when the holes created in the ground state are filled again.[1]

Due to the similar wavelength of X-ray radiation to the distances between atoms in the crystal lattice, monochromatic electromagnetic radiation can be elastically dispersed and experience constructive and destructive interference, which is explained by Bragg's law in the equation 2.1. The following variables are defined in the equation 2.1 : the order of interference (n), the (λ) wavelength of X-rays, the lattice spacing of the material (d), and the angle of incidence (θ).[2] CuK_{α} radiation with a wavelength of 1.5418 Å makes copper the most popular target material used in single crystal diffraction.

$$n\lambda = 2dsin(\theta) \quad (2.1)$$

According to Bragg's law When the sample is exposed to these X-rays, they interact with the crystalline phases in the specimen, resulting in diffraction. Bragg's law provides a clear explanation of the necessary conditions for constructive interference. To capture all potential lattice diffraction directions, the specimen is systematically scanned across a range of 2θ angles, because of the material's random orientation since each material has its own unique set of d-spacings. A material is figured out by converting the diffraction peaks into d-spacings. Thus, the diffraction peak of a material becomes visible on the detector at a certain angle. Furthermore, the relative intensities of the peaks being distinct for each atom are contingent upon the positions of the atoms within the lattice structure.

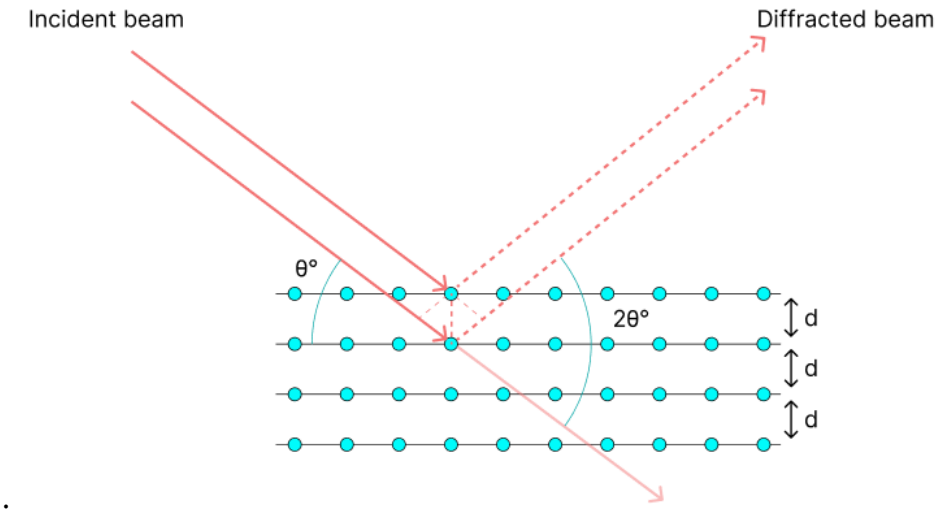

Figure 2.1 An X-ray diffraction diagram within the framework of a crystal lattice. Atoms serve as the scattering nuclei, denoted by blue circles. θ represents the incidence angle of X-rays. The distance between the reflecting planes is denoted by d.

2.2 Grazing Incidence Wide Angle X-Ray Scattering (GIWAXS)

GIWAXS is a reliable technique used to gather data on the crystal phase and orientation of a thin film in relation to the normal of the substrate surface.

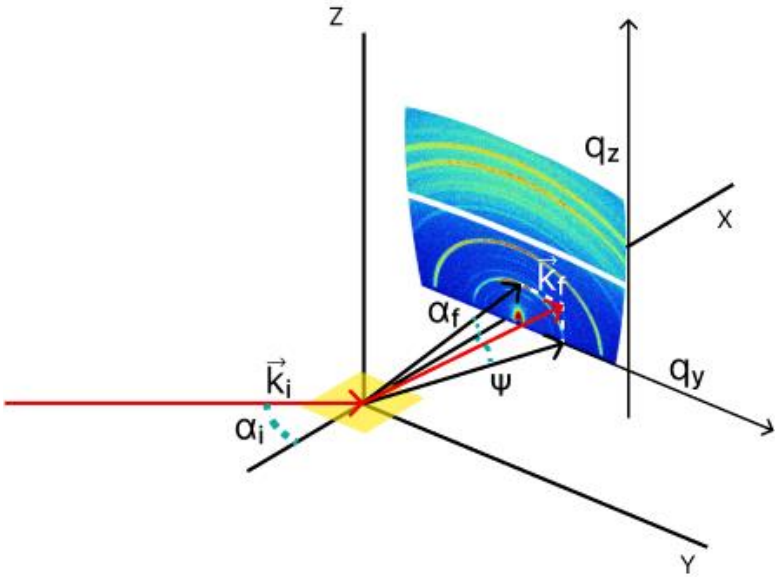

Figure 2.2 Visualization of wide-angle grazing-incidence scattering using vectors and important scattering angles.

In a standard XRD setup, which utilizes a point detector or a 1D-detector, scan configuration a significant amount of signal from the substrate is collected. However, using low incidence

angles in this advanced technique results in a substantially amplified signal, as the surface of the film is merely studied by integration of the measurement with a 2D detector. Furthermore, accurate data regarding the film's orientation is obtained.[3,4]

To examine a sample, an X-ray beam is used which is characterized by the wave vector $\vec{k}i$ at an angle of incidence αi that is normally in the range < 1º. This is usually selected around the critical angle, that is, the entire external reflection of the wave takes place. Following surface scattering, 2D detector is employed to find the intensity represented by the values of Ψ, and α_f which are quite small. They are expressed as lateral (q_y) or vertical (q_z) wavevectors respectively. By using the 2D imaging technique, specific patterns can be acquired depending on the orientation, showing partial rings or dots, as seen in single crystals or precisely oriented thin films. When the crystal structure exhibits a random orientation, it forms Debye-Scherrer rings with homogeneous density on the area detector.[5]

2.3 Electron Microscopies

Electron microscopes are experimental tools that engage high-energy electrons, similar to light, to visualize objects at a very small scale. This instrument offers comprehensive data on the topography, morphology, composition, and crystallographic characteristics. There exist two distinct categories of electron microscopes: transmission electron microscopy (TEM) and scanning electron microscopy (SEM).

2.3.1 Scanning Electron Microscopy (SEM)

SEM is an imaging technology that uses a focused electron beam to provide information about the topography and composition of the sample. As a result of the much smaller De Broglie wavelength of the electrons, this technology is able to produce images with a much higher resolution compared to light microscopes.[6]

During this process, an electron beam is propelled by an electron gun within a high vacuum environment, utilizing a voltage ranging from 1 kV to 30 kV. The beam is then concentrated to achieve a diameter of a few nanometers or smaller using multiple lenses. Then, the electron beam is moved across the sample, resulting in the generation electrons which are detected. The variation in electron detection counts at different scanning points allows for the generation of an image on the cathode-ray tube.[7]

In SEM measurement, the sample is generally visualized by recording the scattering of secondary electrons (SE) and backscattered electrons (BSE). SE have relatively low energy

levels, often ranging from 0 to 50 electron volts (eV). They can only remove if they occur very close to the surface of the sample, owing to the low energy levels. Thus, images recorded by SE have a high spatial resolution.

They are generated through an inelastic scattering mechanism involving atoms, which are excited during this process. The scattered secondary electrons provide valuable insights on the morphology of the material being studied. On the other hand, BSE possessing energy levels more than 50 eV yield valuable insights into the elemental composition of the sample. Furthermore, characteristic X-rays can be utilized in SEM for elemental microanalysis.

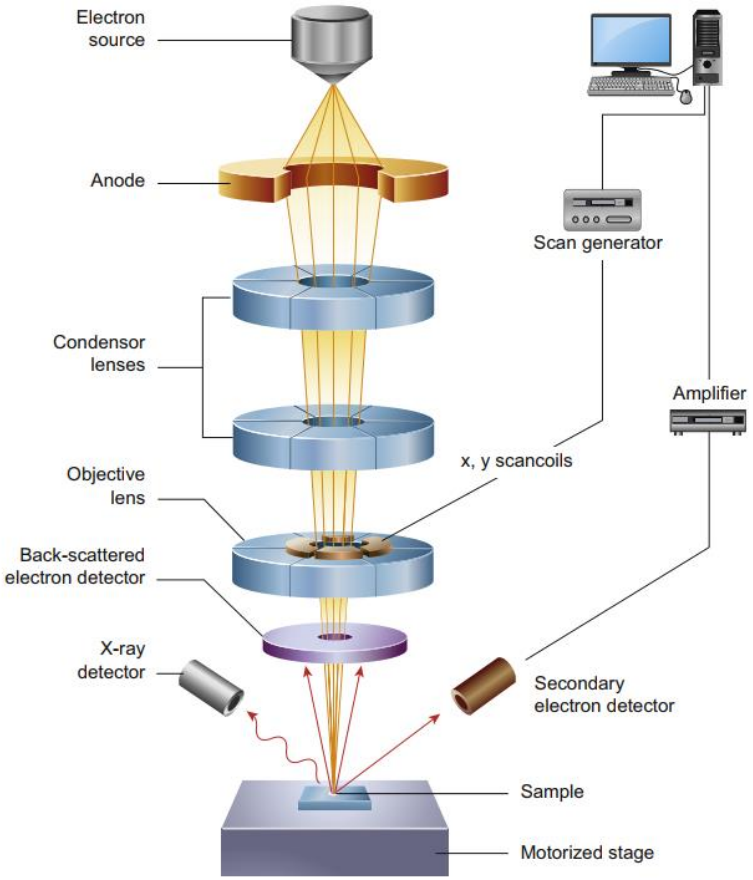

Figure 2.3 An illustration of the scanning electron microscope in schematic form.[8]

Cathodoluminescence (CL) is a technique utilized to identify and analyze nanoscale optical properties. The photons emitted in the ultraviolet and near-infrared regions of the electromagnetic spectrum are analyzed by CL techniques. Integration of functional optical information with the high spatial resolution of SEM defines the power of CL. The integration of functional optical data and the enhanced spatial resolution characteristic of electron microscopy is achieved in CL. As a result, the method is particularly well-suited for an

extensive range of applications within the domain of optics research.

2.3.2 Transmission Electron Microscopy (TEM)

Transmission electron microscopy (TEM) is a method in which an electron beam interacts with an object by passing through it. The operational mechanism of TEM closely resembles that of SEM. The resolution of this technique is significantly greater than that of SEM. Moreover, unlike standard SEM, TEM offers image and diffraction data of the specimen. The entire path of the electron (source to screen) occurs in a vacuum; thus, the sample must be extremely thin to permit it to go through.[9] Figure 2.4 displays the geometry of the TEM. The robustness of the samples is a major prerequisite for the analysis of samples using TEM. Using high voltages ranging from 60 kV to 400 kV during the measurement can cause less stable samples to deteriorate or decompose, resulting in reduced resolution and poor image quality.[10]

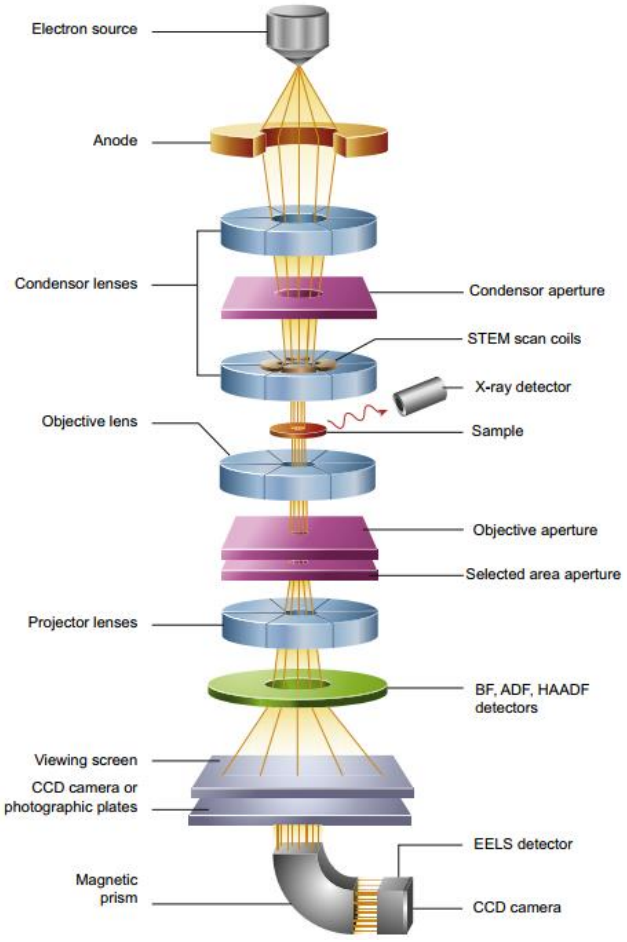

Figure 2.4 An illustration of the TEM imaging mode.[8]

When the electrons are generated by a source, they undergo concentration and magnification by magnetic lenses. The condenser lenses confine the electron beam, so that the electron beam

passes through the condenser aperture to strike the surface of the sample. The transmitted beams, resulting from the elastic scattering of the electrons, go through the objective lens. The image formation takes place within the objective lens. Thus, elastically scattered electrons forming the image of the microscope are then selectively gathered in the objective and selected area aperture. These electrons are chosen based on their trajectory within the objective and through the determined area aperture. Finally, the beam is directed towards a magnifying system, where the resulting image is displayed on the monitor.

2.4 Ultraviolet-Visible (UV-vis) Absorption Spectroscopy

By utilizing UV-vis spectroscopy method, the light absorption characteristics of molecules in solution or the bulk material can be determined. UV-vis absorption spectroscopy measures the absorption and reflection of a sample in a wavelength-dependent manner between the visible, UV, and near-infrared regions of the electromagnetic spectrum. The visible spectrum extends from 400 nm to 800 nm, whereas the UV spectrum spans 190 nm to 400 nm. A spectrometer consists of a light source, a monochromator, a sample holder, and a detector to achieve this aim. Light sources commonly employed to produce a continuous spectrum consist of a deuterium arc lamp for the ultraviolet region and a tungsten filament or xenon arc lamp for the visible region. Through light dispersion, the monochromator generates a wavelength-resolved spectrum. A signal is ultimately detected by a photomultiplier, photodiode array, or charge-coupled device.

Absorption behavior is typically characterized by the Lambert-Beer law, which is expressed in equation 2.2 and provides the definition of absorbance A:

$$A = -log_{10}\left(\frac{I}{I_0}\right) = \varepsilon * c * d \tag{2.2}$$

The equation demonstrates that the absorption of the sample at a specific wavelength is linked to the intensity of the incident (I) and measured (I_0) beam. This law establishes that the concentration of a substance in a solution correlates with A, the molar extinction coefficient (ϵ), the concentration of the solution (c), and the optical path length (L).[11] In addition, the Beer-Lambert Law cannot be used for samples with several layers as the light is scattered and diffracted at the interfaces between two different media. Precise calculation of the absorbance for this category of materials can be achieved through measurements utilizing an integrating sphere, which is then adjusted by selecting an appropriate reference.[12]

The interactions between light and the sample can be categorized into three possibilities:

absorption, transmission, or reflection of light. Hence, the intensity of the incident light can be expressed as the proportions of absorbed (%A), reflected (%R), and transmitted (%T) light.

The calculation of the absorbed light percentage, %A, can be determined using the following equation:

$$\%A = 1 - \%T - \%R \quad (2.3)$$

The calculation of absorbance can be determined using the following equation:

$$A = -log_{10}(1-\%A) \quad (2.4)$$

$$A_{film} = A_{sample} - A_{reference} \quad (2.5)$$

A tauc plot is utilized to approximate the optical E_g of semiconductors. Tauc plot equation is expressed given below in 2.6

$$(\alpha h\nu)^{1/r} = A(h\nu - E_g) \quad (2.6)$$

In this equation, α represents the absorption coefficient of the material, *ν is* frequency of light, h and A are Planck´s constant and proportionality constant respectively. In the illustration of a tauc plot, the energy of incident light (hυ) is on the x-axis, and the quantity $(\alpha h\upsilon)^{1/r}$ is on the y-axis. The exponent r represents the characteristic of the transition, with r = ½ indicating direct allowed transitions and r = 2 indicating indirect allowed transitions. Thus, the point where the linear regression of the squared absorption coefficient and photon energy intersects the energy axis corresponds to the band gap in semiconductors with a direct band gap. On the other hand, in semiconductors with an indirect band gap, the band gap is calculated by the intersection of the linear fit of the square root of the absorption coefficient and photon energy with the energy axis.[13]

2.5 Photoluminescence Spectroscopy (PL)

Photoluminescence spectroscopy is a technique used to analyze the electronic properties of materials, study the optoelectronic behavior of semiconductors, and detect defects in the interface region. When light is directed onto a sample, it is absorbed and transfers excess energy to the material through a process known as photo-excitation. Luminescence is the process by which excess energy is released by the emission of light. When a photo-excitation occurs, the resulting luminescence is referred to as photoluminescence (PL).

When the incident photon possesses an adequate amount of energy, it will stimulate an electron moving from the VB to the CB across the band gap. Recombination is the process by which

electrons return to equilibrium (Transitioning from an excited state down to the ground state), this phenomenon can encompass radiative and non-radiative mechanisms.

Radiative recombination refers to the process of band-to-band recombination, in which the excess energy is discharged through the emission of light. This means that when an electron moves from the CB to the VB state, a photon is emitted. In addition, electron-hole recombination can take place through non-radiative processes, wherein emission does not occur. These processes can be attributed to surface states, bulk defects, and traps, as depicted in Figure 2.5.[14]

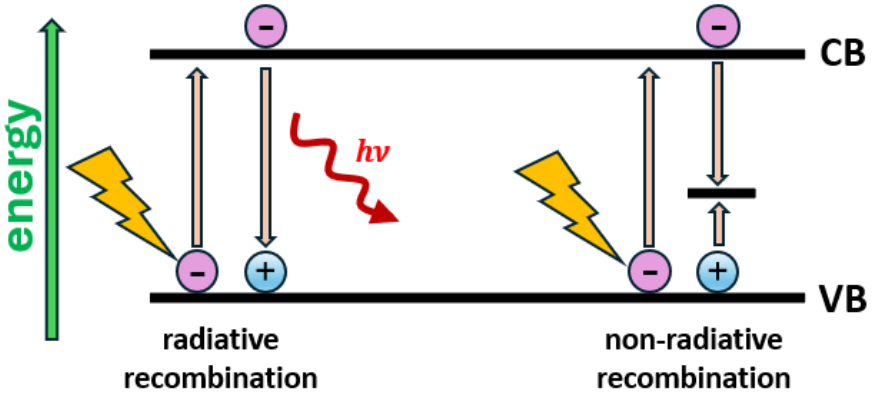

Figure 2.5 A diagram depicting the process of radiative and non-radiative recombination that occurs when a laser is used to excite a material.

2.6 Time-Correlated Single Photon Counting (TCSPC)

TCSPC is a technique used to analyze the fluorescence characteristics of materials and compounds. Unlike steady-state approaches that determine the photoluminescence (PL), this spectroscopy is time-resolved. This method uses a short pulse of light to stimulate the specimen and monitor its deterioration in a dark environment, while measuring the intensity of the signals depending on time.

The duration required for the light intensity of a fluorescent sample to diminish to the proportion 1/e is referred to as the lifetime of the sample. Essentially, lifetime describes the average time at which a molecule remains in an excited state.

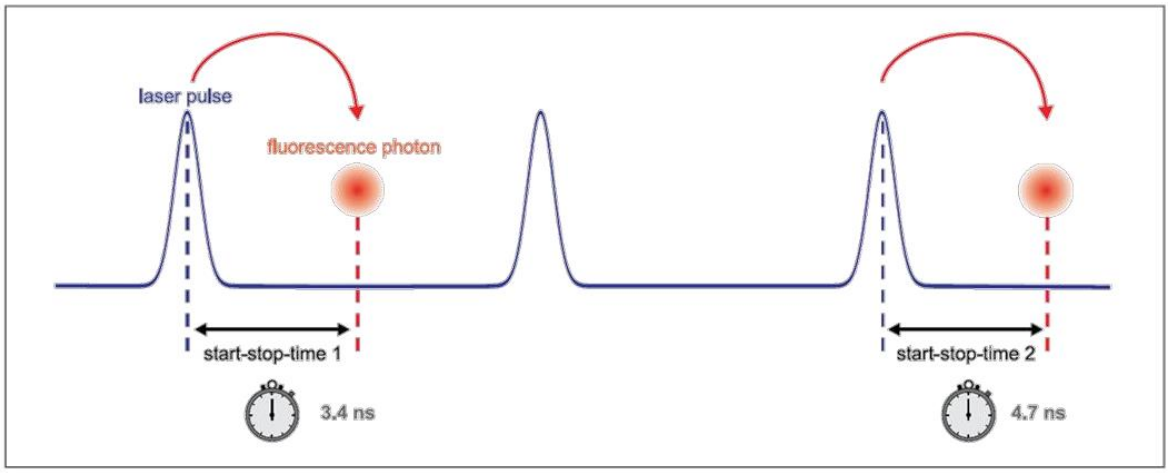

Figure 2.6 Measurement of start-stop times in TCSPC.[15]

The set-up measures the time between the generation of a pulse by the excitation source to the emission of a photon, as depicted in Figure 2.6. Data is transmitted, and the intensity of the released photons is graphed as a function of time. It is essential to measure only one photon at a time and graph each photon on a histogram, as depicted in Figure 2.7. A decay curve is produced subsequent to the accumulation of several photons. The photon count is utilized because the emission intensity is correlated with the likelihood of detecting a photon at a certain time.

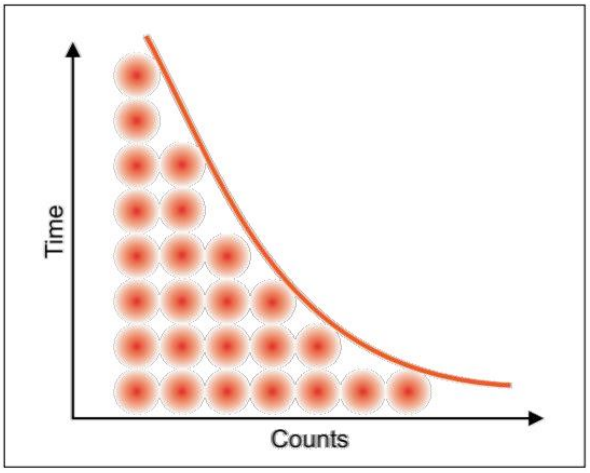

Figure 2.7 Histogram of start-stop times with TCSPC measurements.[15]

2.7 External Quantum Efficiency (EQE) Measurements

The quantum efficiency (QE) is the proportion of number of charge carriers collected by the solar cell to the number of photons that hit the solar cell at each wavelength. It can be

mathematically represented as a function of either the wavelength or the energy of the photon. Quantum efficiency can be classified into two categories: internal quantum efficiency (IQE) and external quantum efficiency (EQE). The EQE is commonly known as the IPCE, which stands for internal photon-to-charge carrier conversion efficiency. The IQE can be calculated from this value, representing the ratio of absorbed photons to produced charge carriers.[16] This section will exclusively focus on explaining EQE, as the calculation of IQE is dependent on EQE. The fundamental principle for determining the EQE (External Quantum Efficiency) of a solar cell sample is to establish the ratio between the quantity of incident photons (n_{ph}) and the photogenerated carriers (n_e) in relation to the wavelength:

$$EQE(\lambda) = \frac{ne(\lambda)}{nph(\lambda)} \tag{2.7}$$

The integrated photocurrent is another significant metric that can be calculated based on this data. The value is determined by integrating the EQE curve and the photon flux at one sun. This helps to validate and comprehend the J_{SC} values obtained from the *J/V* measurements of the examined solar cell. In this context, J_{int} represents the integrated photocurrent, q denotes the elemental charge, and $\Phi(\lambda)$ represents the photon flux of one sun.

$$J_{int} = q\int_0^{\infty} \Phi(\lambda) * EQE_{dioede}(\lambda) d\lambda \tag{2.8}$$

J_{int} of a solar cell value must fall around 90% of the J_{SC} to validate the J_{SC}.

2.8 Contact Angle Measurement

The contact angle is the angle that is defined between the interface of the liquid-vapor and the solid-liquid at the point of contact of the three phases, as shown in Figure 2.8. This angle is known as the wetting phenomenon. Typically, the contact is measured at the point where the liquid and air come into touch with one another. To characterize the contact angle, the Young equation is implemented:

$$Cos\theta_{YD} = \frac{\gamma_S - \gamma_{SL}}{\gamma_L} \tag{2.9}$$

The variables denoted as θ_{YD}, γ_S, γ_{SL}, and γ_L represent contact angle, solid-liquid interface energy, and liquid-gas interface energy, respectively.[17]

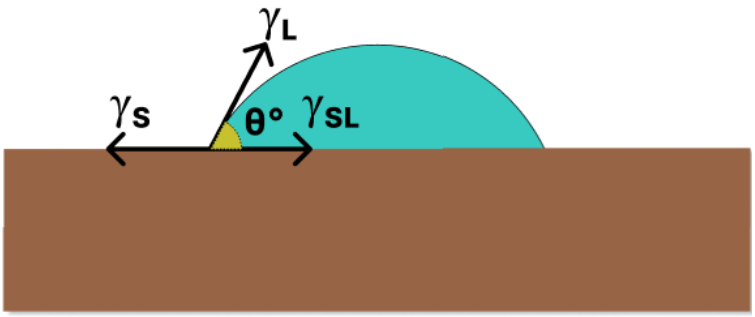

Figure 2.8 Illustration of contact angle (θ) and associated parameters.

The Young equation implies that the surface is an ideal, devoid of reactivity, and chemically uniform. The Young equation predicts that surfaces with high surface energy have low contact angles, whereas surfaces with low surface energy have high contact angles. Hydrophilic surfaces are characterized by a water contact angle that is below 90°, while hydrophobic surfaces exhibit contact angles that exceed 90°.[18]

The measurement of contact angles is conducted utilizing a goniometer apparatus. A syringe is used to drop a small amount of liquid onto a sample stage that may be adjusted. A light source is used to illuminate the droplet from the back, while a camera is employed to capture photographs of the process of situating the droplet. The contact angle of the droplet curvature is extracted by applying various fitting processes to the photos using analytic software. The approach in question is commonly referred to as the sessile drop method. The wetting dynamics of the wetting process can be investigated using a high-speed camera.

2.9 Photoelectron spectroscopy (PES)

PES is an important surface-sensitive instrument that serves for investigating the electron energy distribution within a compound.[19] It provides insights into various aspects such as the elemental composition, chemical bond characteristics, electronic states, and VB energy levels. In general, the sample is exposed to X-rays or ultraviolet photons of high energy radiation. The ejected electrons have a dispersion of kinetic energies (KE) that depend on the binding energies.

They proceed from the sample to an energy analyzer, where the KEs are documented, and then to a detector that enumerates the quantity of photoelectrons at different KEs.

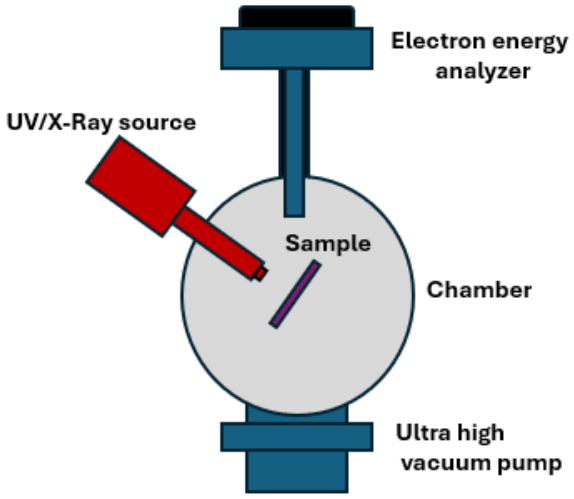

Figure 2.9 Schematic illustration of a photoelectron spectrometer.

By applying Einstein's equation (2.10) concerning the photoelectric effect, the ionization (binding) energy of the emitted electron can be computed. In this equation, E_{KE}, $h\nu$, E_{BE}, and ϕ represent the KE of the emitted electron, the energy of the incident photon, binding energy of the electron, and work function of the solid sample respectively.

$$E_{KE} = h\nu - E_{BE} - \phi \quad (2.10)$$

The information obtained through the measurement is contingent upon the radiation source, which is classified as ultraviolet photoelectron spectroscopy (UPS) or X-ray photoelectron spectroscopy (XPS).

2.9.1 X-Ray Photoelectron Spectroscopy (XPS)

XPS utilizes soft X-rays with an energy range of 0.2-2 keV to analyze the core levels of a sample's surface. The ionization and ejection of electrons from the core orbitals, resulting from their relatively high energy, yield valuable insights about the chemical composition of the surface of the material under investigation.[20] Furthermore, this methodology offers insights into the oxidation state and subsequent surface reactions and alterations in surface states, contingent upon the quantity of ejected electrons. This statement highlights the utilization of the fact that atoms exhibiting a higher positive oxidation state possess a greater electron binding energy which is due to the additional Coulomb interaction between the ejected electron and the ionized core.

2.9.2 Ultraviolet Photoelectron Spectroscopy (UPS)

Vacuum ultraviolet (UV) radiation with an energy range of 10–45 eV is employed for the purpose of conducting ultraviolet photoelectron spectroscopy. The utilization of UPS is employed for the purpose of defining the ionization energy of electrons within the valence levels. In this experiment, the ionization and detection of electrons in the valence orbitals of the sample under investigation provide significant knowledge into the binding energy and VB energy of the sample under study.[21]

2.10 Raman Spectroscopy

Raman spectroscopy relies on the phenomenon of inelastic scattering of light by a sample, resulting in a displacement of the scattered light's frequency. This shift allows for the acquisition of valuable insights into the vibrational modes exhibited by the sample.

It is necessary for the polarizability of bonds to undergo alterations for vibrations to exhibit Raman activity as a result of the scattering of monochromatic light.[22] Raman spectroscopy involves the utilization of a laser to expose the sample to radiation. The light absorbed by the sample stimulates an electron to transition from a vibrational state to a virtual energy state. Subsequently, the scattered light is gathered and subjected to analysis.

The phenomenon of Rayleigh scattering is characterized by the elastic scattering of the primary component at the same frequency as the incident light, accompanied by the inelastic scattering of a minor fraction. The following equation represents the phenomenon of Rayleigh scattering. The molecule or crystal lattice absorbs elastically scattered photons, causing a shift from the ground state to an excited virtual state. The emission of a photon of the same wavelength occurs as a result of subsequent relaxation to the ground state.

$$h\nu_{incident} = h\nu_{scattered} \quad (2.11)$$

The light scattered in an elastic manner can exhibit either a greater frequency, known as anti-Stokes scattering, or a lower frequency, known as Stokes scattering, in comparison to the incident laser light. The frequency of the scattered light relies on the vibrational modes of the sample. The energy of the scattered light in Stokes scattering is comparatively lower than that of the incident light. As a consequence, the frequency of the scattered light shifted towards lower values. Stokes scattering is the phenomenon in which the molecules of a scattering material absorb the energy of incident light and subsequently re-emit it as a photon with lower energy.

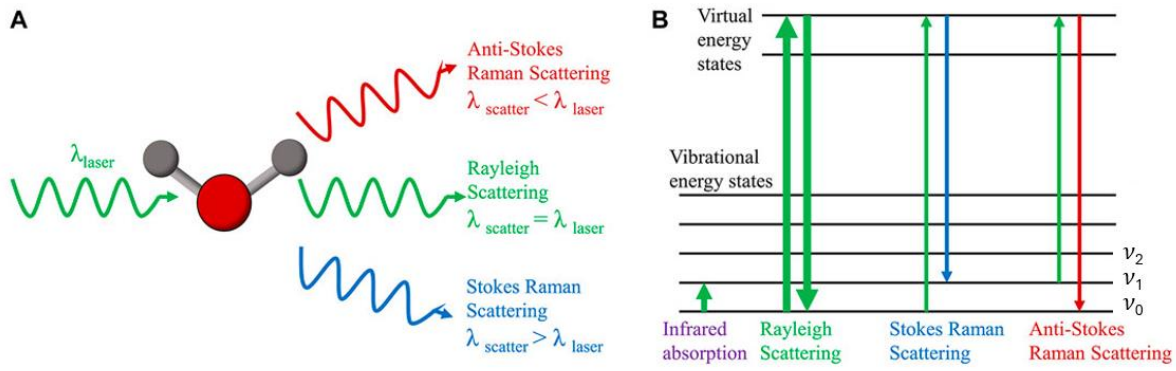

Figure 2.10. Theory of Raman scattering. A) Schematic illustration of Raman and Rayleigh scattering. B) Schematic representation of energy diagram of Raman, Rayleigh scattering and infrared absorption.[23]

Anti-Stokes scattering is characterized by the phenomenon where the energy of the scattered light exceeds that of the incident light.

As a consequence, the frequency of the scattered light shifted towards higher values. The phenomenon takes place when the energy of the incident light is utilized to stimulate the molecules of the scattering material, resulting in the re-emission of a photon with a higher energy. Anti-Stokes or Stokes shifts, which are noticed as shifts in frequency, are unique to each molecule and provide insights into its molecular structure. Peaks at various frequencies in the Raman spectrum of a sample indicate the vibrational modes of the chemical bonds present in the sample. A molecule's functional groups can be identified, and its chemical composition and structure can be determined using the Raman spectrum.[24]

2.11 Current-Voltage (*J/V*) Measurements

The measurement of the current-voltage (J/V) curve is considered the most effective method for evaluating the performance of a solar cell. The J/V curve serves as a valuable tool for obtaining important data, including power conversion efficiency (PCE), short circuit current density (Jsc), open circuit voltage (V_{oc}), and fill factor (FF). The J/V curve of a perovskite solar cell is depicted in Figure 2.11.

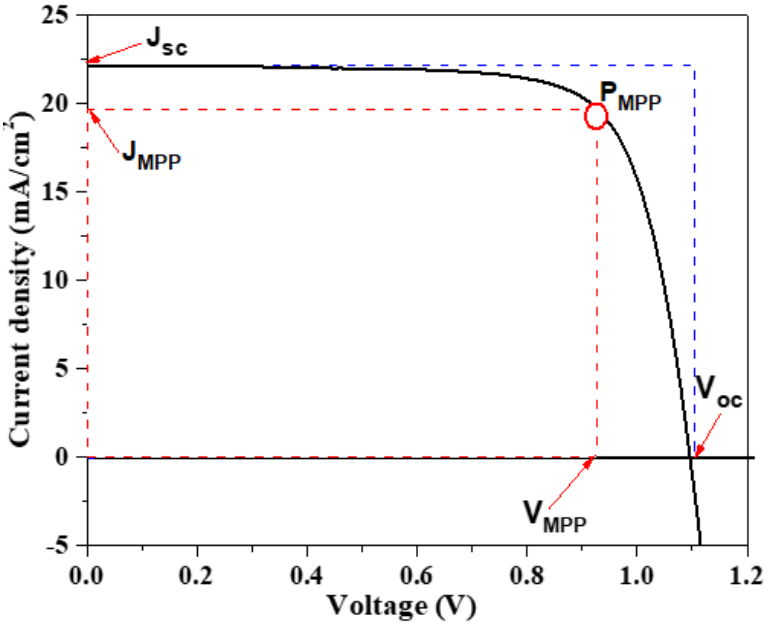

Figure 2.11 The J/V curve obtained from a solar cell and its distinctive photovoltaic properties.

An illuminated solar cell exhibits a J-V curve that closely simulates a diode model. The solar cell design consists of a diode and current source optimized to minimize series and maximize shunt resistances in the PV device designed to be useful for enhancing performance as shown in Figure 2.12.

A current source is generated by the absorbed light. The diode imitates the directional characteristic of the solar cell stack. Rs represents a series resistance in the open diode state, while R_{SH} is a shunt resistance in the short-circuited diode state. These components are within the equivalent circuit diagram. Hence, it is reasonable to obtain the total current flowing through the circuit using the subsequent equation (2.12):

$$I=I_L - I_D-I_{SH} \tag{2.12}$$

The output current of the solar cell is denoted as I, while the photogenerated current is represented by I_L. The diode current is denoted as I_D, and the shunt current is marked as I_{SH}.

The performance coefficient of the voltage supplied by a solar cell when the net current passing through the cell is zero is referred to as the open circuit voltage (V_{oc}), which is the maximum voltage value that can be obtained from a solar cell. Several factors, especially the bandgap of the material, have an effect on it. In general, an increase in the bandgap is associated with a higher $V_{oc.}$

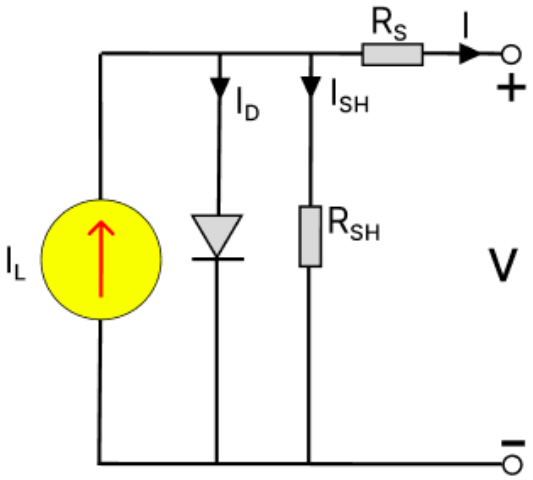

Figure 2.12 The illustration of the diode model for a solar cell.

However, it is important to note that this parameter is also affected by another factors such as the ratio of non-radiative to radiative recombination, interfacial recombination, and the lifetime of charge carriers. The maximum current flow in the cell at zero bias voltage is defined by the J_{sc}. The determination of this value is dependent on the efficiency of charge carrier collection and production rate, which in turn is influenced by optical parameters such as incident light and the band gap of the material. It is worth noting that a narrower bandgap corresponds to a higher number of absorbed photons, leading to the creation of charge carriers.[25] The values of V_{oc} and J_{sc} (blue dotted lines) are shown in Figure 2.11.

The concept of the maximum power point (MPP) refers to the highest power output (P_{MPP}) that a solar cell is capable of producing. It is situated at the point where the J/V curve intersects with the greatest rectangular region formed by the multiplication of the current (J_{MPP}) and voltage (V_{MPP}), as shown in Figure 2.11. (red dotted lines). The power at each point of the J/V curve can be calculated by multiplying the voltage and current to compute FF and determine the maximum power of the solar cell. The variable FF serves as a measure of internal losses, specifically indicating the peak value of the maximum power in relation to the product of V_{oc} and J_{sc}. The FF is a ratio between the maximum power and the total area covered by V_{oc} and J_{sc} can be calculated by the equation (2.13) given below:

$$FF = \frac{P_{MPP}}{V_{OC} * Jsc} = \frac{V_{MPP} * J_{MPP}}{V_{OC} * Jsc} \tag{2.13}$$

The assessment of the solar cell's overall quality heavily relies on this crucial metric, which might offer insights into potential malfunctions. This parameter is greatly affected by internal

charge carrier losses, including high series resistance and interfacial recombination. The power conversion efficiency (PCE) of solar cells is a measure of their overall efficiency. It precisely related to the rate of the electricity generated to the incoming light power (P_{in}).[26] The equation 2.14 given below describes PCE.

$$PCE = \frac{J_{SC} V_{oc} FF}{P_{in}} \tag{2.14}$$

2.12 References

[1] KITTEL, Charles; MCEUEN, Paul. *Introduction to solid state physics*. John Wiley & Sons, 2018.

[2] BRAGG, W. H.; BRAGG, W. L. Proceedings of the Royal Society of London: Series A, Containing Papers of a Mathematical and Physical Character. *Proc. R. Soc. London, Ser. A*, 1913, 88: 428-438.

[3] DOSCH, Helmut; BATTERMAN, B. W.; WACK, D. C. Depth-controlled grazing-incidence diffraction of synchrotron X radiation. *Physical review letters*, 1986, 56.11: 1144.

[4] DUBČEK, Pavo. Nanostructure as seen by the SAXS. *Vacuum*, 2005, 80.1-3: 92-97.

[5] SCHLIPF, Johannes; MÜLLER-BUSCHBAUM, Peter. Structure of organometal halide perovskite films as determined with grazing-incidence x-ray scattering methods. *Advanced energy materials*, 2017, 7.16: 1700131.

[6] WILLIAMS, Hollis. SEM for conductive and non-conductive specimens. *Physics Education*, 2021, 56.5: 055034.

[7] STEFANAKI, Eleni-Chrysanthi. Electron microscopy: the basics. *Physics of advanced materials winter school*, 2008, 4: 1-11.

[8] INKSON, Beverley J. Scanning electron microscopy (SEM) and transmission electron microscopy (TEM) for materials characterization. In: *Materials characterization using nondestructive evaluation (NDE) methods*. Woodhead publishing, 2016. p. 17-43.

[9] FULTZ, Brent; HOWE, James M. *Transmission electron microscopy and diffractometry of materials*. Springer Science & Business Media, 2012.

[10] BRANDON, David; KAPLAN, Wayne D. *Microstructural characterization of materials*. John Wiley & Sons, 2013.

[11] PERKAMPUS, Heinz-Helmut. *UV-VIS Spectroscopy and its Applications*. Springer Science & Business Media, 2013.

[12] SNAITH, Henry J.; DUCATI, Caterina. SnO2-based dye-sensitized hybrid solar cells exhibiting near unity absorbed photon-to-electron conversion efficiency. *Nano letters*, 2010, 10.4: 1259-1265.

[13] TAUC, J.; GRIGOROVICI, Radu; VANCU, Anina. Optical properties and electronic structure of amorphous germanium. *physica status solidi (b)*, 1966, 15.2: 627-637.

[14] RAJA, Pavan; BARRON, Andrew R. Physical methods in chemistry and nano science. 2019.

[15] WAHL, Michael. The Principle of Time-Correlated Single Photon Counting.*PicoQuant*

Technical Note, 2014, 1-14.

[16] HIERREZUELO-CARDET, Pedro, et al. External quantum efficiency measurements used to study the stability of differently deposited perovskite solar cells. *Journal of Applied Physics*, 2020, 127.23: 235501

[17] CADDEO, Claudia, et al. Hydrophilicity and water contact angle on methylammonium lead iodide. *Advanced Materials Interfaces*, 2019, 6.3: 1801173.

[18] DRELICH, Jaroslaw, et al. Hydrophilic and superhydrophilic surfaces and materials. *Soft Matter*, 2011, 7.21: 9804-9828.

[19] BENIGNA, James. Photoelectron spectroscopy in advanced placement chemistry. *Journal of Chemical Education*, 2014, 91.9: 1299-1305.

[20] ANDRADE, Joseph D. (ed.). *Surface and Interfacial Aspects of Biomedical Polymers: Volume 1 Surface Chemistry and Physics*. Springer Science & Business Media, 2012.

[21] ELAND, John HD. *Photoelectron spectroscopy: an introduction to ultraviolet photoelectron spectroscopy in the gas phase*. Elsevier, 2013.

[22] Larkin, P., Chapter 1 - Introduction: Infrared and Raman Spectroscopy. In Infrared and Raman Spectroscopy, Larkin, P., Ed. Elsevier: Oxford, 2011; pp 1-5.

[23] LIU, Kunxiang, et al. Raman spectroscopy: A novel technology for gastric cancer diagnosis. *Frontiers in Bioengineering and Biotechnology*, 2022, 10: 856591

[24] GRAVES, PRGDJ; GARDINER, D. Practical raman spectroscopy. *Springer*, 1989, 10: 978-3.

[25] WURFEL, Peter, et al. *Physics of solar cells*. Willy-Vch, Verlag, 2005.

[26] FIELD, Halden. Methods and Instruments for the Characterization of Solar Cells. *Photovoltaic Solar Energy: From Fundamentals to Applications*, 2016, 303-321.

3. A Novel Multi-Functional Thiophene-Based Organic Cation as Passivation, Crystalline Orientation, and Organic Spacer Agent for Low-Dimensional 3D/1D Perovskite Solar Cells

This chapter is based on the following publication:

Semerci, A†, Buyruk, A†, Emin, S., Hooijer, R., Kovacheva, D., Mayer, P., ... & Ameri, T. (2023). A Novel Multi-Functional Thiophene-Based Organic Cation as Passivation, Crystalline Orientation, and Organic Spacer Agent for Low-Dimensional 3D/1D Perovskite Solar Cells. *Advanced Optical Materials*, 2300267.

† Equal first-author contribution

†† The bulk treatment in this study is performed by Ali Semerci and surface treatment by Ali Buyruk.

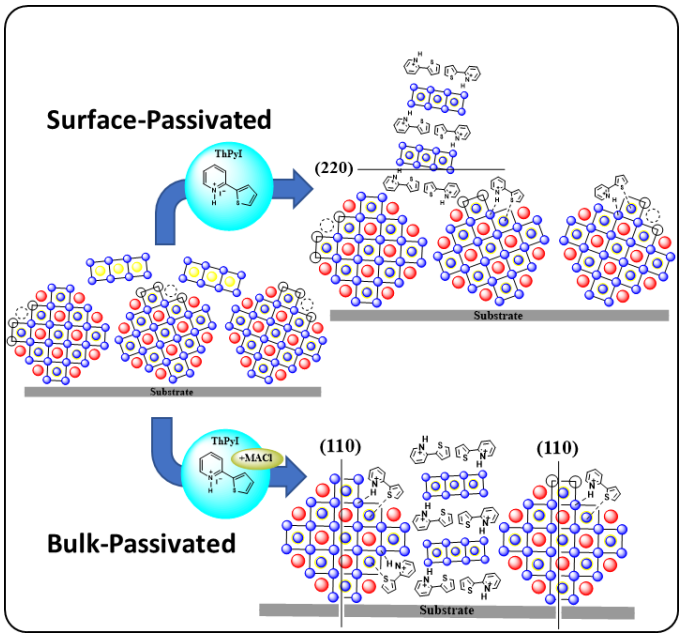

Keywords

1D perovskite, 3D/1D perovskite, solar cell, passivation, bulk-passivated 3D perovskite, crystalline orientation promoter

3.1 Introduction

During the last decade, three-dimensional (3D) organic-inorganic halide perovskites (OIHPs) have emerged as promising absorber materials for photovoltaic applications due to their superior properties such as high absorption coefficient, long diffusion length of the charge carriers, fast charge transport and tunable bandgap. The 3D OIHPs have demonstrated rapid increase in power conversion efficiency (PCE) from 3.8% to 25.2%.[1–9]

On the other hand, their moderate intrinsic stability against moisture and heat still has been a concern with a view on possible commercialization.[10–14] Instability of the 3D MAPI perovskite is assumed to be due to its crystalline structure. Ionic migration is now well recognized to affect the photovoltaic properties of perovskite solar cells. Especially, the ionic migration causes the generation and displacement of vacancies in perovskite materials. OIHPs are mixed ionic–electronic conductors with iodide ions as the majority ionic carriers. The diffusion coefficient of 10^{-12} cm^2 s^{-1} for I^- ions is several orders of magnitude higher than the value of 10^{-16} cm^2 s^{-1} for $CH_3NH_3^+$. The organic cations such as $CH_3NH_3^+$or $NH_2CH=NH_2^+$ show however moderate degrees of freedom for ion migration, which is one of the main reasons why 3D perovskite structures have poor stability.[15–17] Adsorption of water and oxygen molecules at vacancy sites is predominant than at pristine surfaces accelerating perovskite degradation via the vacancy-assisted mechanism. When MAPI is exposed to water, it degrades to lead(II)iodide (PbI_2), iodide anions, and methylammonium cations (MA^+).[16–17] In addition to the instability issues, surface and bulk defects in 3D polycrystalline perovskites can strongly affect the carrier recombination and hence performance of solar cells.

In the meantime, lower-dimensional relatives of the 3D halide perovskites have attracted growing attention. Here, layers of larger organic cations separate slabs of octahedral perovskite-like inorganic layers, with profound impact on band structure, charge carrier transport and often much improved stability.[14] However, the insulating nature of organic spacers in the low-dimensional perovskite can limit the conductivity and can contribute to low photovoltaic performance despite their enhanced environmental stability.[18]

To address the above-mentioned challenges, a strong research focus has been put on developing new strategies and approaches to suppress recombination processes and to overcome the stability issues of 3D halide perovskite structures.[19-20] Among the various passivating additives, it has been reported that ammonium salts can effectively diminish the impact of defects caused by dangling bonds or vacancies.[21-22] Another strategy for passivation is the

introduction of low-dimensional perovskites in the 3D perovskite system.[23] Following this approach, the passivation of defects can be achieved, and the intrinsic stability issues of the 3D MAPI structure can be addressed. Therefore, passivated and mixed-dimensional perovskite solar cells (PSCs) have been fabricated using small organic molecular spacers.[24] The low-dimensional (1D or 2D) perovskite structures found in the resulting mixed-dimensional perovskites serve both as passivating agents to reduce the impact of defects and as heterojunctions that enhance the fluorescence lifetimes in the perovskite structure.[21] Hence, mixed-dimensional perovskites recently evolved as suitable photovoltaic (PV) candidates due to their encouraging environmental stability and wide tunability of optical properties.[25-30] Here, the higher perovskite stability could be attributed to the hydrophobic nature of the organic spacers used. [31-32] For example, 1D perovskitoids can be used both on top of 3D perovskite films or in the bulk perovskite by adding the desired organic cations to the precursor solution to improve efficiency and stability of perovskite PV devices.[33-35]

It has been demonstrated that the metal halide bonds can break upon illumination, followed by rearrangement of the perovskite crystal structure.[30] The individual metal halide octahedra formed during this reorganization are more stable than the regularly bonded ones.[36] In 1D perovskitoid structures, the $[PbI_6]^{4-}$ octahedral framework structure based on edge, face, or corner-sharing connect to the organic spacers. In this case, the metal halide octahedra are surrounded by organic spacer molecules.[37] Among the reasons for the instability of tin and lead based perovskites are the high-energy orbitals ($5s^2$ (Sn^{2+}) /$6s^2$ (Pb^{2+})) near the top of the valance band, which are more reactive.[38] The edge or face-sharing binding motif of 1D structures stabilizes these high-energy orbitals, which leads to better environmental stability. [39] For example, Liu et.al employed 1D PbI_2-bipyridine (BPy) to incorporate into the 3D MAPI perovskite structure. Thereby, the obtained 1D perovskite layers reduced the ion migration by improving the stability of the 3D/1D perovskite structure.[40] Gao et al. used thiazole ammonium iodide (TAI) to form a 1D $TAPbI_3$ capping layer on 3D MAPI, improving the stability and performance of corresponding PSCs compared to the 3D MAPI control device.[39] Yang et al. used polymerizable propargylammonium to fabricate 1D structures at the surface and grain boundaries in a mixed-dimensional 3D/1D perovskite. By this means, they enhanced the charge transport and decreased the tensile strain of perovskite layers.[34]

The solar cells with grain boundary passivation have been reported to be superior in performance compared to those without passivation since grain boundaries can act as

recombination centers. The most studied defects in MAPI perovskites are the point defects. Twelve different types of defects are generally observed in MAPI, including vacancies, interstitials, and anti-site occupations.[41] Defects at grain boundaries in polycrystalline perovskites are a major source for recombination of photo-generated carriers. Typical examples for tailored passivation schemes of defects include the use of polymers, quaternary ammonium salts, and other organic compounds.[42-50] In order to reduce non-radiative recombination in the bulk and at grain boundaries, both inorganic additives (Cl^-, SCN^-, etc.) or organic molecules have been introduced into the perovskite materials.[51]

In this work, a novel organic spacer 2-(thiophene-2yl-) pyridine-1-ium iodide (ThPyI) was developed to fabricate mixed-dimensional bulk-passivated 3D and surface-passivated 3D/1D perovskite solar cells. The ThPyI organic spacer is proposed to generate 1D structures at the grain boundaries of surface-passivated 3D perovskite films. Further, the ThPyI organic spacer is also viewed as a promising passivating agent for reducing other defects in the 3D MAPI and as a suitable material to create 3D/1D heterostructure perovskites for efficient charge separation. Employing the two different passivation methods of bulk and surface treatment, the impact of this organic spacer on the photovoltaic performance, stability, structural as well as optoelectronic properties of the corresponding perovskite solar cells was investigated. The optimized PCE of bulk-passivated 3D and surface passivated 3D/1D mixed-dimensional PSCs reached 14.10% and 19.60%, respectively, with significantly improved stability compared to the reference 3D PSCs.

3.2. Results and Discussion

The molecular structure of the ThPyI organic spacer used in this work is illustrated in **Figure 1a**. The characterization of ThPyI was performed with nuclear magnetic resonance (^{1}H-,^{13}C-NMR) and mass spectroscopy (**Figure S1a-d**, Supporting Information). The so-called surface-passivated 3D/1D device was prepared by spin-coating of ThPyI on top of MAPI films.

As for the bulk-passivated 3D perovskite, the fabrication process is similar to the case of MAPI, with the addition of ThPyI into the precursor solution. The latter sample comprising both ThPyI and methylammonium chloride (MACl) agents is called “bulk-passivated 3D” from here on. For the purpose of comparison with the bulk-passivated 3D perovskite, MAPI-based control devices were fabricated with and without MACl additive. It is worthwhile mentioning that based on a known effect, MACl is added to the bulk-passivated 3D MAPI to achieve

preferential orientation of the crystal grains.[34] However, in the surface-passivated samples the use of MACl was avoided due to the use of excess PbI_2 (5% mol) in the precursor solution. Further processing details are provided in the experimental section. Interestingly, both methods of ThPyI-based surface and bulk passivation result in the formation of a new perovskite-related phase, which is identified as the 1D perovskitoid structure ($C_{18}H_{16}I_8N_2Pb_3S_2$), as explained in the following.

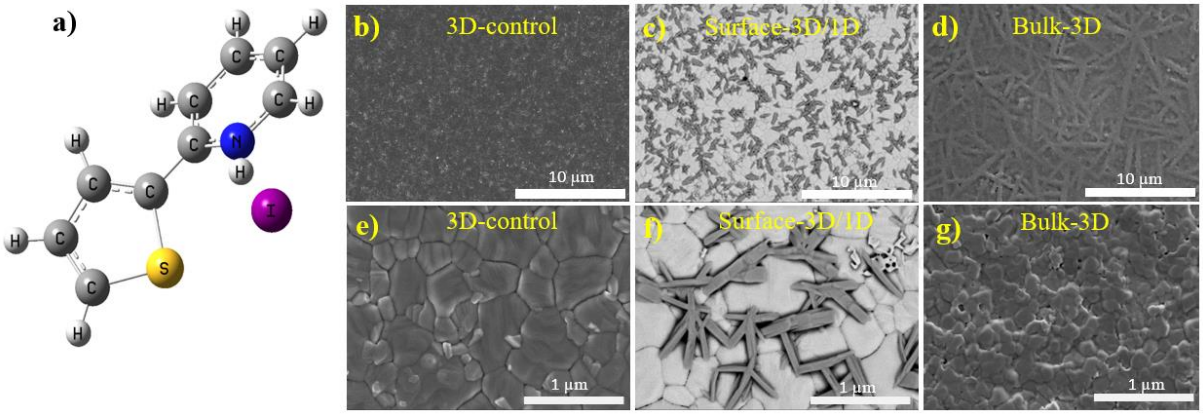

Figure 1. a) Molecular structure of ThPyI spacer. SEM images of b, e) 3D MAPI control film, c, f) surface-passivated 3D/1D, and d, g) bulk-passivated 3D MAPI perovskite film.

To evaluate the morphology of 3D control, bulk-passivated 3D, and surface-passivated 3D/1D MAPI perovskite films, scanning electron microscopy (SEM) measurements were performed. As shown in the top-view SEM images of the corresponding films in **Figure 1b-g,** the active MAPI layers completely cover the substrate surface. The grain-based morphology in the 3D control and the surface-passivated 3D/1D films looks very similar. However, on the surface-passivated 3D/1D perovskite film, needle-like new features form preferentially at the 3D perovskite grain boundaries as shown in **Figure 1c**. These needles assemble into an interconnected network which may affect the charge transport across the grains. In comparison to the 3D MAPI control, bulk-passivated 3D MAPI perovskite film shows a different surface morphology. In the 3D control with MACl, the interconnected needles were no longer observable (**Figure S2**, Supporting Information).

The grains of bulk-passivated 3D perovskite seem to be more closely connected (or fused) which appears to obscure their grain boundaries. At lower magnification (× 2000) the bulk

passivated 3D perovskite shows interconnected needle-shape formations as shown in **Figure 1d**. It is well-known that needle-like morphology can offer enhanced charge collection compared to pure planar films.[52-54] Here, the bulk-passivated 3D film shows homogenous composition without any formations assigned to an additional phase.

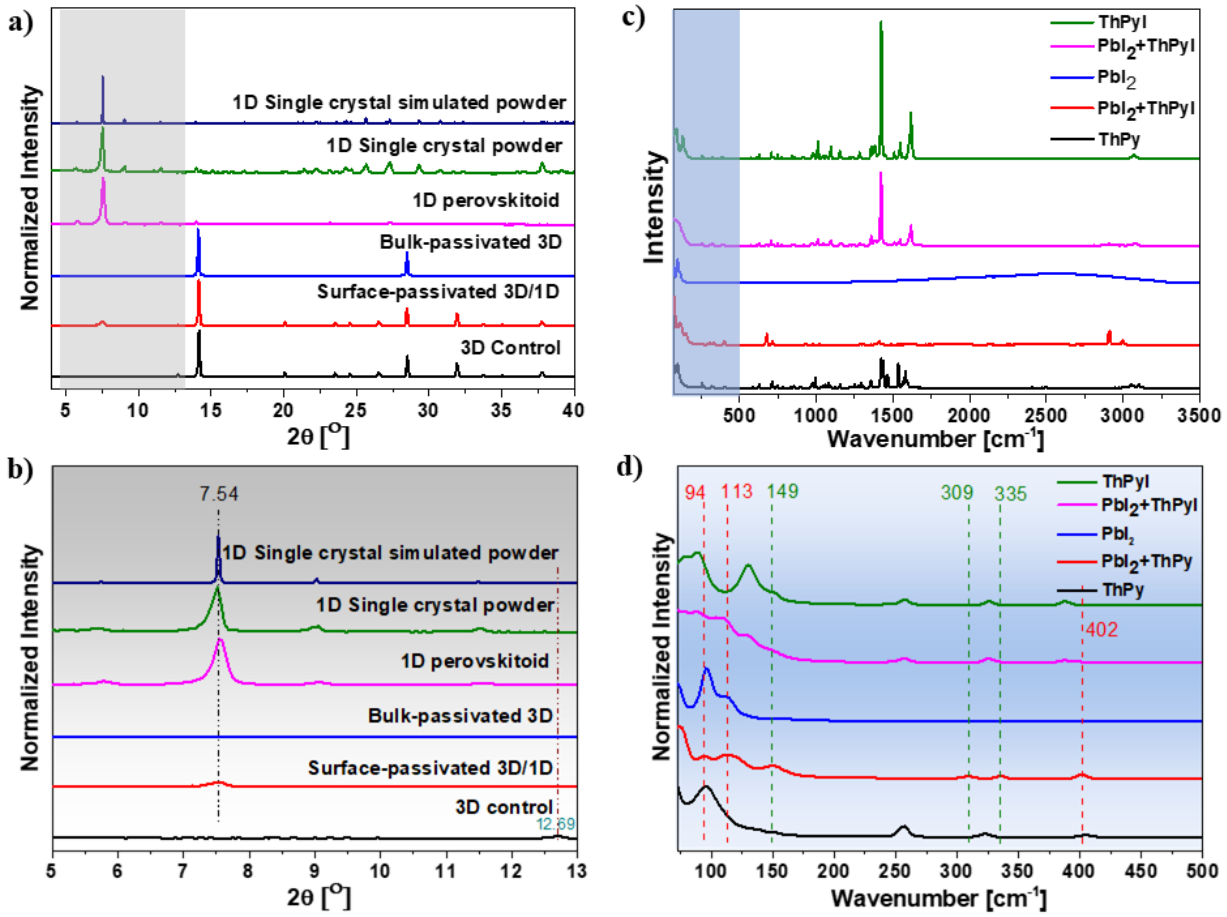

Figure 2. XRD patterns of pure 1D perovskitoid film and 1D single crystal powder, simulated 1D, 3D control, bulk-passivated 3D, and surface-passivated 3D/1D perovskite thin films showing a) wide scan and b) enlarged XRD pattern from 5 and 13˚*2θ*. C) Raman spectra of powder forms taken of the ThPy ligand, ThPyI, PbI_2, the mixture of PbI_2 + ThPy, and the mixture of PbI_2 + ThPyI. D) Narrow range Raman spectra taken from c).

X-ray diffraction (XRD) measurements were employed to investigate the crystallinity of a 1D single crystal, 3D control, surface-passivated 3D/1D, and bulk-passivated 3D perovskite films as shown in **Figure 2a**. The main XRD peaks of the 3D control appear at 14.19º and 28.50º *2θ*, which correspond to (110) and (220) planes, respectively. As illustrated in the XRD data, the bulk-passivated 3D perovskite film (3D Bulk with MACl) fabricated using MACl also exhibits these two dominant diffraction peaks. The lack of additional reflections or any peak shift indicates that the addition of the ThPyI organic spacer into the 3D perovskite film does not

change the MAPI lattice. The absence of other diffraction peaks from MAPI or a possible second phase (including below <12º 2θ) confirms both the phase purity and the preferential orientation of the MAPI grains. Here, the preferential orientation is achieved by the addition of MACl, which is widely used in the literature as an additive to boost the PCE.[55]

As observed in the XRD pattern of the surface-passivated perovskite, a new peak appears at low 2θ values (7.54º). This additional peak can be related to the needle-like formations at the 3D perovskite grain boundaries shown in **Figure 2c, f**. Moreover, this new phase did not result from PbI_2 or from the pure ThPyI organic spacer according to the XRD patterns. To elucidate the structure of the needle-like formations on the surface-passivated perovskite film, single crystals were grown by reacting stoichiometric ratios of PbI_2 and ThPyI (**Figure S3**, Supporting Information). The structural analysis of the needle-shaped single crystals was performed using both powder XRD data shown in **Figure 2** and single crystal diffraction (**Figure S4**, Supporting Information).

To further confirm the presence of both the 3D control MAPI and the 1D perovskitoid, powder XRD measurements and Rietveld refinements were carried out. The results of the Rietveld refinement of the structure and the Rietveld plot of the fit are presented in **Figures S5-6 and Table S2** in the Supporting Information. The whole powder pattern fitting procedure of the 1D-film (**Figure S6**) revealed a single phase 1D perovskitoid with unit cell parameters a = 25.494(4) Å, b = 61.82(1) Å and c = 4.5968(8) Å, which are close to those observed for the single crystal phase (**Table S1,** Supporting Information).

According to the single crystal diffraction results and the calculated powder diffraction pattern, the single crystal data perfectly matches the XRD pattern of the 1D perovskitoid structure {with reflections at 5.7º (040), 7.5º (220), 9.0º (240), 11.0º (260), and 11.4º (080)} The crystal structure of the 1D perovskitoid corresponds to the unit cell formula $C_{18}H_{16}I_8N_2Pb_3S_2$ given in **Figure 3**. In the crystal structure, three edge-shared octahedra are accompanied by two edge-to-edge aligned organic spacer (ThPyI) molecules, which engage in strong N^+-H···I-Pb hydrogen-bonding interactions (**Figure S4**, Supporting Information). According to the obtained crystallographic data, the 1D perovskitoid features an orthorhombic crystal system (*Fdd*2 space group) (**Table S1,** Supporting Information). In good agreement with the single crystal XRD data of the 1D perovskitoid, the new peak emerging at 7.54º for the surface-passivated sample can be assigned to the 1D perovskitoid phase as shown in **Figure 2b**. We note that under these conditions, reflections corresponding to the 1D phase are missing in the

diffractogram of bulk-passivated 3D MAPI. However, when the passivation is done without (wo) added MACl, the dominant peak at 7.54° is clearly seen, which indicates the formation of the 1D perovskitoid phase (**Figure S7**, Supporting Information).

To gain additional insight about the needles formed on the surface of the 3D/1D perovskite film, Raman spectroscopy was employed as shown in **Figure 2c, d**.

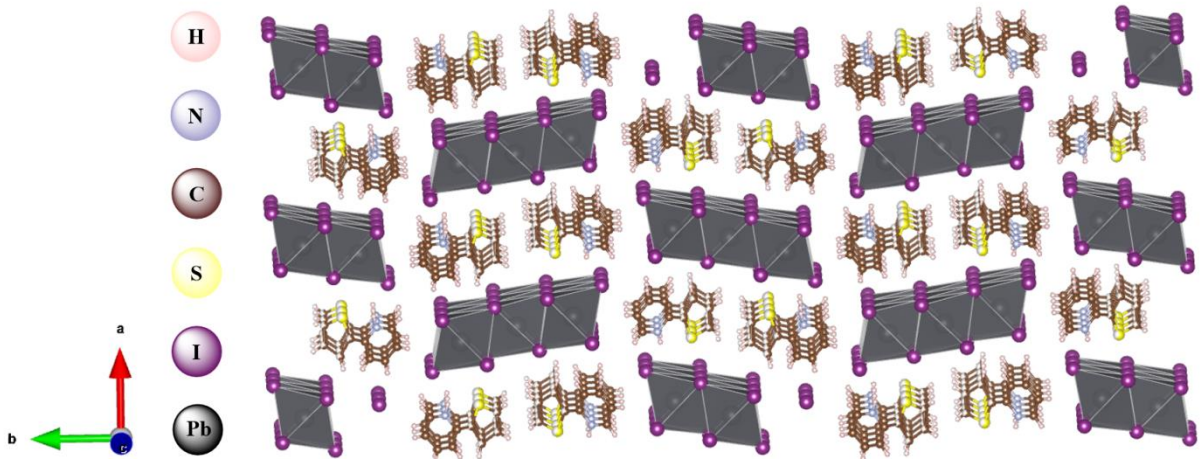

Figure 3. Schematic representation of the crystal structure of the 1D perovskitoid unit cell. The free iodine atoms which appear in the schematic are part of the octahedra of the adjacent unit cell which is not involved here.

The Raman spectra of the ThPyI organic spacer, its neutral form (ThPy, unprotonated), PbI_2, and mixtures of PbI_2 + ThPy, and PbI_2 + ThPyI were compared to eliminate the possibility that the needles derive from a basic complex form of PbI_2 with the organic spacer (**Figure S8,** Supporting Information).[56] The Raman vibrational frequencies of the mixture of PbI_2 + ThPy appear at 74, 94, 112, 149, 309, 335, and 402 cm^{-1} (red and green dashed lines in **Figure 2d**). Some of these signals (red dashed lines) are shifted compared to those of PbI_2 and ThPy. Moreover, two Raman vibrational frequencies of free ThPy at 258 and 323 cm^{-1} disappear, while two new vibrational frequencies appear at 309 and 335 cm^{-1} (green dashed lines). These new signals are in the region of the metal-nitrogen stretching vibrations (200-600 cm^{-1}). In sum, these observations suggest that a new phase has formed via a chemical reaction between PbI_2 and ThPy.[57]

Unlike the mixture of PbI_2 + ThPy, the Raman spectrum of the mixture of PbI_2 + ThPyI shows no shifts and/or new signals. This indicates that here the Raman signals are due to the unreacted mixture of PbI_2 and ThPyI since these overlap with the signals of pure PbI_2 and ThPyI. To support the Raman results for the unreacted PbI_2 + ThPyI mixture, its solution-state ^{1}H-NMR

was evaluated (**Figure S1d-e,** Supporting Information). In the PbI_2–ThPyI solution, no new ^{1}H-NMR signal associated with a chemical reaction was recorded. Interestingly, the signal of the proton (N^+-H) of the pyridine group shows an up-field shift (shielding effect), which is a specific hint as to the strong N^+-H···I-Pb-I hydrogen-bonding interactions. In addition to the up-field shifted proton (N^+-H), obvious up-field shifts for the neighboring protons of both rings (ThPy) are also observed. Together, these results confirm that complexation between ThPyI and PbI_2 is not the cause of the needle-like formations after surface treatment.

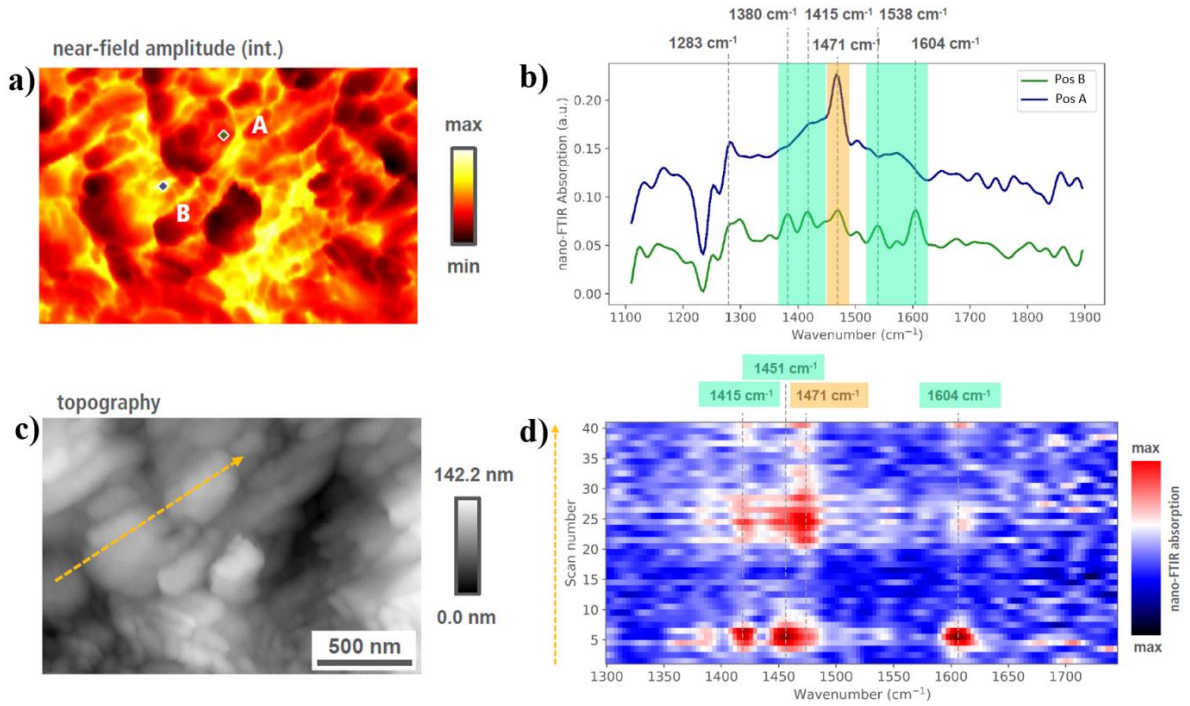

Figure 4. Nano-FTIR analysis of surface-passivated 3D/1D perovskite film. a) broadband, integrated near-field amplitude image, b) spectra recorded from the positions in A and B shown in a), c) topography of the surface, and d) spectral image recorded from the line scan in c).

To study the needle-like formations on the surface-passivated 3D/1D perovskite sample at the nanoscale (10-20 nm spatial resolution), nano-FTIR spectroscopy was used.[58] Two locations were identified from the broadband near-field amplitude image taken on the surface-passivated 3D/1D sample, presented in **Figure 4a**. While spot (A) was taken on the top of a 3D perovskite grain, spot (B) was recorded from the needle-like formations (1D phase) which is observed in SEM images (**Figure 1c-f**). The selected broadband infrared range for these two spots varied from 1100 to 1900 cm^{-1} as given in **Figure 4b**. In spot B the intense vibration at 1471 cm^{-1}

(orange highlight) was assigned to the well-known symmetric NH_3^+ bending of methylammonium in MAPI.[59] Additionally, four new signals (highlighted in green) were observed for position B corresponding to the needle-like formation, which are not seen in the MAPI grain (position A).[60] Furthermore, these new signals are similar but slightly shifted to lower wavenumbers compared to those seen in the ThPyI organic spacer (**Figure S9,** Supporting Information). The new vibrations can be assigned to the 1D perovskitoid phase. The observed shift to lower wavenumbers in the 1D perovskitoid is attributed to the local environment in the 1D perovskitoid crystal structure. To probe the distribution of the 1D formations in detail, position-dependent measurements (one spectrum at every 30 nm) along a 1.2 μm sample distance were carried out as indicated by the orange dashed arrow in **Figure 4c**. We note that the signals from the 1D phase formations are predominantly observed at the 3D perovskite grain boundaries as shown in **Figure 4c-d**.

Grazing incidence wide-angle X-ray scattering (GIWAXS) was conducted to evaluate the orientation of perovskite crystallites in the 3D control, bulk-passivated 3D MAPI and surface-passivated 3D/1D perovskite films with and without MACl respectively. The 3D reference crystallizes with random orientation, observable through the diffraction rings as shown in **Figure 5a**. This result is in accordance with previous studies.[61] The reflection along the azimuthal angle around 0°, below the first diffraction ring corresponding to MAPI, corresponds to the (001) plane of PbI_2. Excess PbI_2 is common for untreated 3D MAPI thin films and is caused by surface degradation of the perovskite film, as well as by the excess use of PbI_2 in the precursor solution.[62]

The 3D reference with MACl displays the same features, although the intensity of the PbI_2 reflection is increased and the MAPI diffraction rings show a slight (110) horizontal orientation (orientation always with regard to the substrate plane), as shown in **Figure 5d**. The surface-passivated 3D/1D samples display a new set of reflections in the lower *q* region, shown in **Figure 5b**. These reflections appear with a horizontal orientation and can be assigned to the (040), (220) and (240) reflections of the 1D perovskitoid phase. The surface-passivated 3D/1D samples with MACl do not show any preferential orientation, or any diffraction corresponding to the 1D perovskitoid phase, see **Figure 5e**. The bulk-passivated 3D MAPI without MACl samples display oriented reflections for the 3D MAPI phase, indexed and shown in **Figure 5c**, as well as the reflections of the 1D perovskitoid phase with a horizontal orientation.

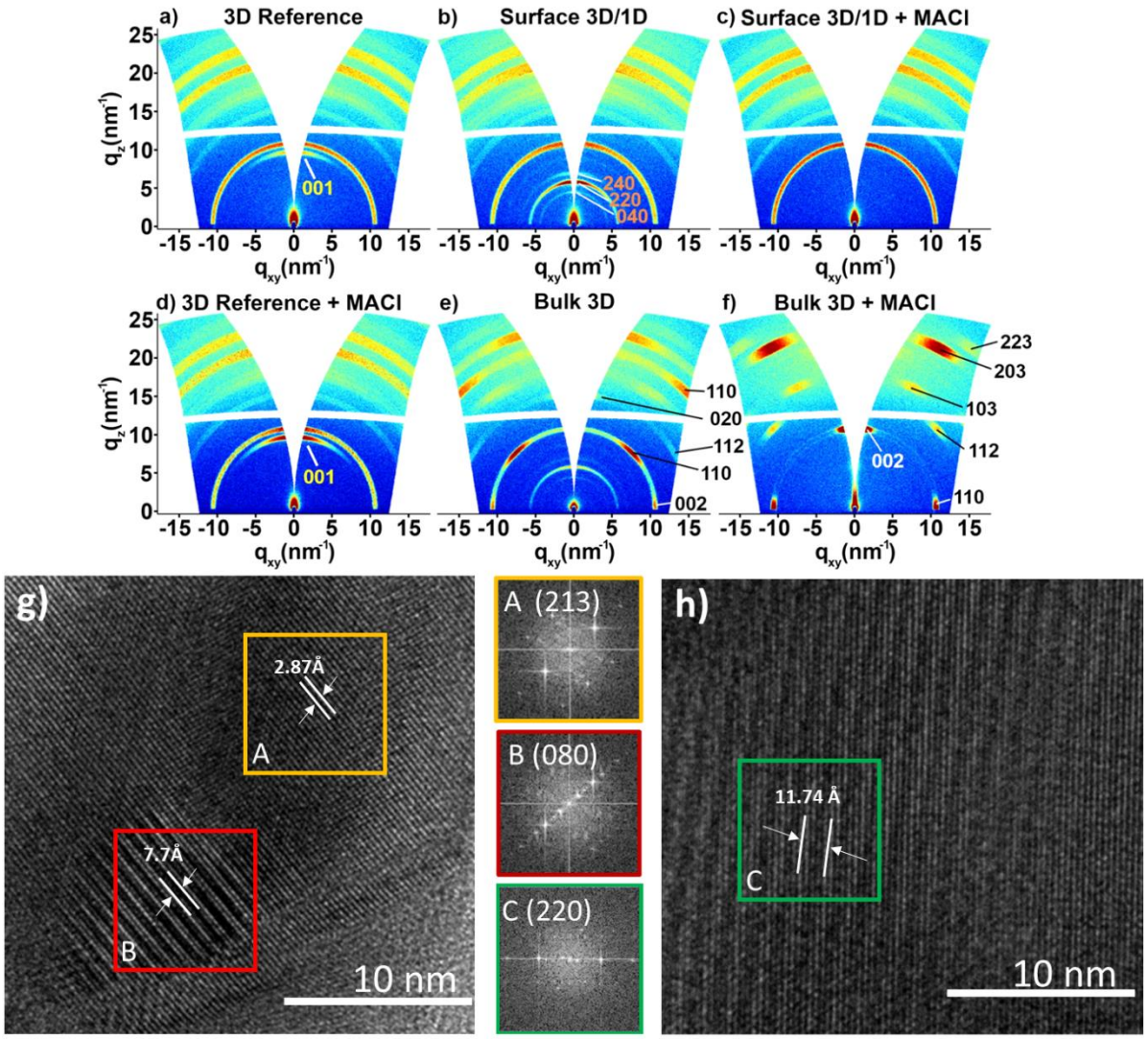

Figure 5. GIWAXS data of a) 3D control MAPI (with +5% excess PbI_2), b) surface-passivated 3D/1D without MACl, c) surface-passivated 3D/1D with MACl, d) 3D control MAPI of the bulk-passivated sample with MACl, e) bulk-passivated 3D MAPI without MACl, and f) bulk-passivated 3D MAPI with MACl. g, h) TEM images of bulk-passivated 3D MAPI (without MACl) perovskite film and corresponding fast Fourier transforms (FFT) taken from the marked areas in A, B and C.

These GIWAXS result are consistent with the XRD results where the 1D perovskitoid phase can be clearly seen in the bulk-passivated 3D film MAPI without MACl (**Figure S7a**, Supporting information). Lastly, the bulk passivated 3D MAPI with MACl displays a different orientation for the MAPI reflections and only a very weak reflection of the (220) plane corresponding to the 1D perovskitoid phase. For both bulk-passivated 3D MAPI samples, the ThPyI spacer has a strong influence on the orientation of the MAPI film, while the (110) planes

reorient from horizontal to vertical orientation with respect to the substrate if MACl is additionally employed to control the crystallization. The absence of any strong diffraction, corresponding to the 1D phase in the bulk-passivated 3D MAPI with MACl sample (**Figure 5f** and **Figure S7a**, Supporting information), points towards an interaction between MACl and ThPyI in the crystallization process. The additional MA^+ in the crystallization competes with the amount of Pb^{2+} ions, which is the same for both thin films, i.e., the same amount of PbI_2 in the precursor solution. This is also evident in the surface passivated 3D/1D samples, where if MACl is used in combination with the ThPyI spacer no 1D phase is observed, but rather a complete consumption of the excessive PbI_2 into MAPI (Fig. 5e).

In conclusion for the surface-passivated 3D/1D samples, the combination of the data from the SEM, Nano FTIR and GIWAXS confirm the formation of the 1D phase at the surface and grain boundaries of the perovskite thin film. The ThPyI bulk passivated sample shows evidence of the 1D phase formation in addition to a pronounced horizonal orientation of (110) planes of the 3D MAPI perovskite phase. However, when MACI is used as a co-additive in the bulk-passivated sample, the 3D MAPI perovskite orientation is changed toward vertical (110) orientation and the diffraction peaks of the 1D phase are missing or have a noticeable intensity attenuation. At this stage it is not clear if the ThPyI spacer in the presence of MACl forms an amorphous 1D phase or if it prefers to stay in amorphous molecular (pure ThPyI) form. The impact of the ThPyI and MACl agents on the morphology of surface-passivated and bulk-passivated perovskite films is schematically illustrated in **Figure 6a-f**.To further elucidate the structural properties of the bulk passivated 3D MAPI samples (without MACl), high-resolution transmission electron microscopy (HR-TEM) studies were carried out as shown in **Figure 5g, h**. The HR-TEM images from selected locations confirm the existence of different lattice spacings. The calculated *d*-spacings corresponding to these planes are summarized (**Table S3,** Supporting Information). The narrow interplanar lattice spacing of 2.87 Å corresponds to the (231) diffraction peak of the 3D MAPI phase in **Figure 5g**.

On the other hand, the lattice spacings of 7.7 and 11.74 Å match the (080) and (220) planes of the 1D perovskitoid, respectively, as shown in **Figure 5g, h.** Overall, the interplanar lattice distances agree with the corresponding XRD data (**Table S4,** Supporting Information). The HR-TEM results demonstrate that the 1D perovskitoid phase distributes in the 3D perovskite phase. TEM images were also recorded from bulk-passivated 3D MAPI prepared using MACl. In this case we observed nanoscopic objects like nanorods which after recrystallization under

the intensive electron beam yielded crystallites (of unknown structure) with lattice spacing equal to 7.7 Å (**Figure S10**, Supporting Information).

UV-vis absorption spectroscopy was employed to investigate the optoelectronic characteristics of the perovskite films (**Figure S11a,** Supporting Information). In comparison with the 3D MAPI control film, surface-passivated 3D/1D films (thickness of about 600 nm) show no significant changes, implying that the 1D perovskitoid on top of the 3D structure does not significantly change the absorption features of the photoactive film. However, the bulk-passivated 3D film exhibits a weaker absorption while retaining the spectral features of MAPI. This is attributed to the different thickness of the bulk-passivated 3D film (400 nm).

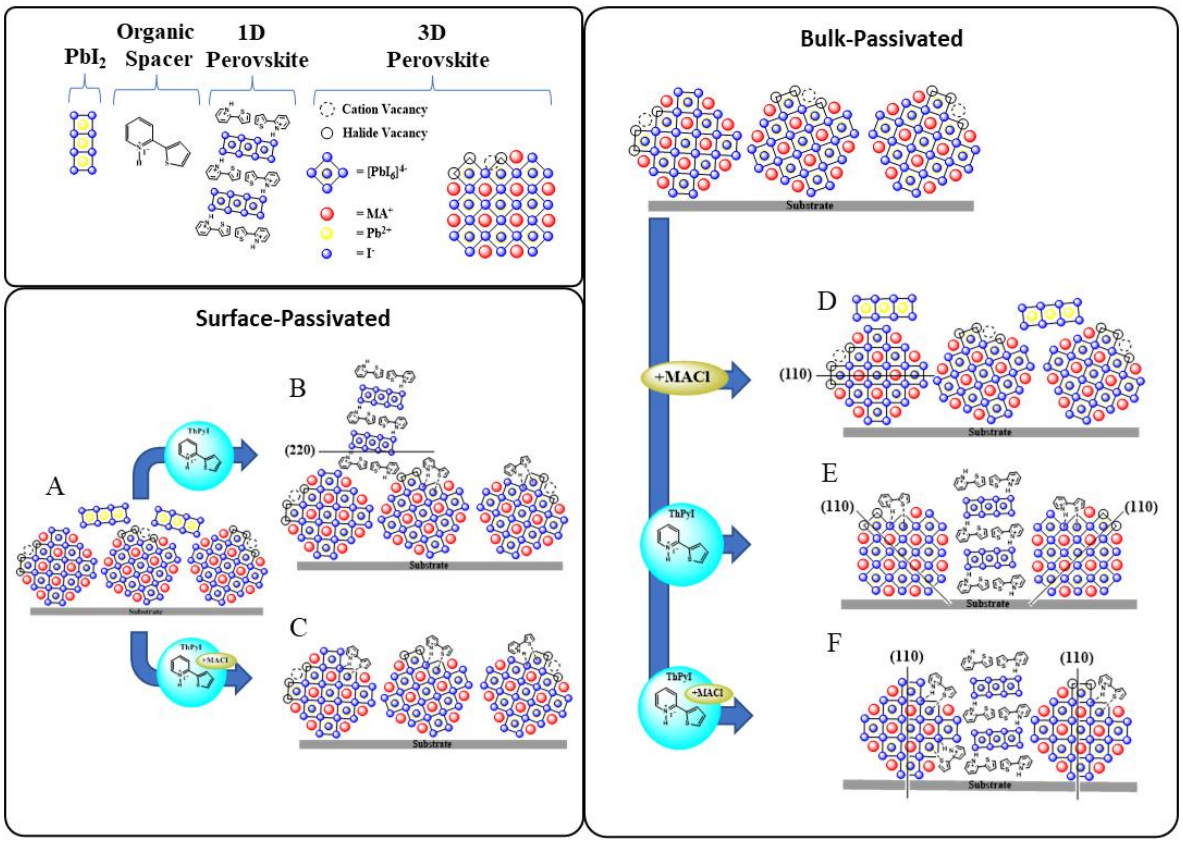

Figure 6. Schematic representation of crystal domain orientation in a) 3D MAPI control (with +5% excess PbI_2), b) ThPyI-surface-passivated 3D/1D c) ThPyI-surface-passivated 3D/1D with MACl d) 3D MAPI control with MACl e) ThPyI-bulk-passivated 3D without MACl, and f) ThPyI-bulk-passivated 3D with MACl.

In line with the similar optical absorption spectrum, the surface-passivated 3D/1D hybrid device shows an EQE response similar to the 3D MAPI control (**Figure S12a,** Supporting Information). In the case of the bulk-passivated 3D MAPI sample, the EQE is higher than that

of the corresponding 3D MAPI reference with MACl (**Figure S12b,** Supporting Information). To determine the energy levels of the bulk-passivated 3D MAPI phase, ultraviolet photoelectron spectroscopy (UPS) was employed (**Figure S11b,** Supporting Information). The valence band maximum (VB) and conduction band minimum (CB) of the bulk-passivated 3D perovskite are estimated at –5.81 and –4.21 eV, respectively, which are very close to the values of 3D MAPI. These energy levels are also compatible with the hole transport layer comprising poly(3,4-ethylenedioxythiophene) poly(styrenesulfonate) (PEDOT:PSS), (–5.1 eV; VB) and the electron transport layer comprising phenyl-C_{61}-butyric acid methyl ester, $PC_{61}BM$, (–3.8 eV; VB).

Steady-state photoluminescence (SSPL) and time-resolved photoluminescence decay (TRPL) measurements were carried out to unravel the charge recombination processes in the 3D MAPI control, bulk-passivated 3D, and surface-passivated 3D/1D films as shown in **Figure 7a–d.** In the case of the bulk-passivated 3D sample, a perovskite film with MACl is considered as the control sample to specify the influence of the ThPyI passivator additive. Notably, more intense PL emission peaks are observed in the surface-passivated 3D/1D and bulk-passivated 3D perovskite films compared to the 3D control, shown in **Figure 7a, b.**

The high PL intensity is an indicator for the elimination of sub-bandgap states in perovskite films that are linked to defect states.[64] The emission peak of the surface-passivated 3D/1D perovskite is slightly blue shifted compared with the 3D control film in **Figure 7a**, which can be attributed to the 1D phase formed on top (**Figure S13**, Supporting Information). The emission peak of the bulk-passivated 3D perovskite appears at similar wavelength comparable with the 3D control with MACl as shown in **Figure 7b**. [65]

The TRPL decay spectra of the corresponding films prepared on glass substrates are shown in **Figure 7c, d.** The TRPL curve was fitted using the following biexponential equation (1):

$$y = A_1 exp\ (\frac{-t}{\tau_1}) + A_2\ exp(\frac{-t}{\tau_2}) + y_0 \qquad (1)$$

where A_1 and A_2 are the amplitudes. The symbols τ_1 and τ_2 express short and long charge carrier recombination times, respectively.[66] Here, we propose that τ_1 is related to the trap-assisted nonradiative recombination arising at the grain boundaries. On the other hand, τ_2 is associated with bulk carrier recombination.[67] The resulting charge carrier lifetimes of the perovskite films are listed (**Table S5**, Supporting Information).

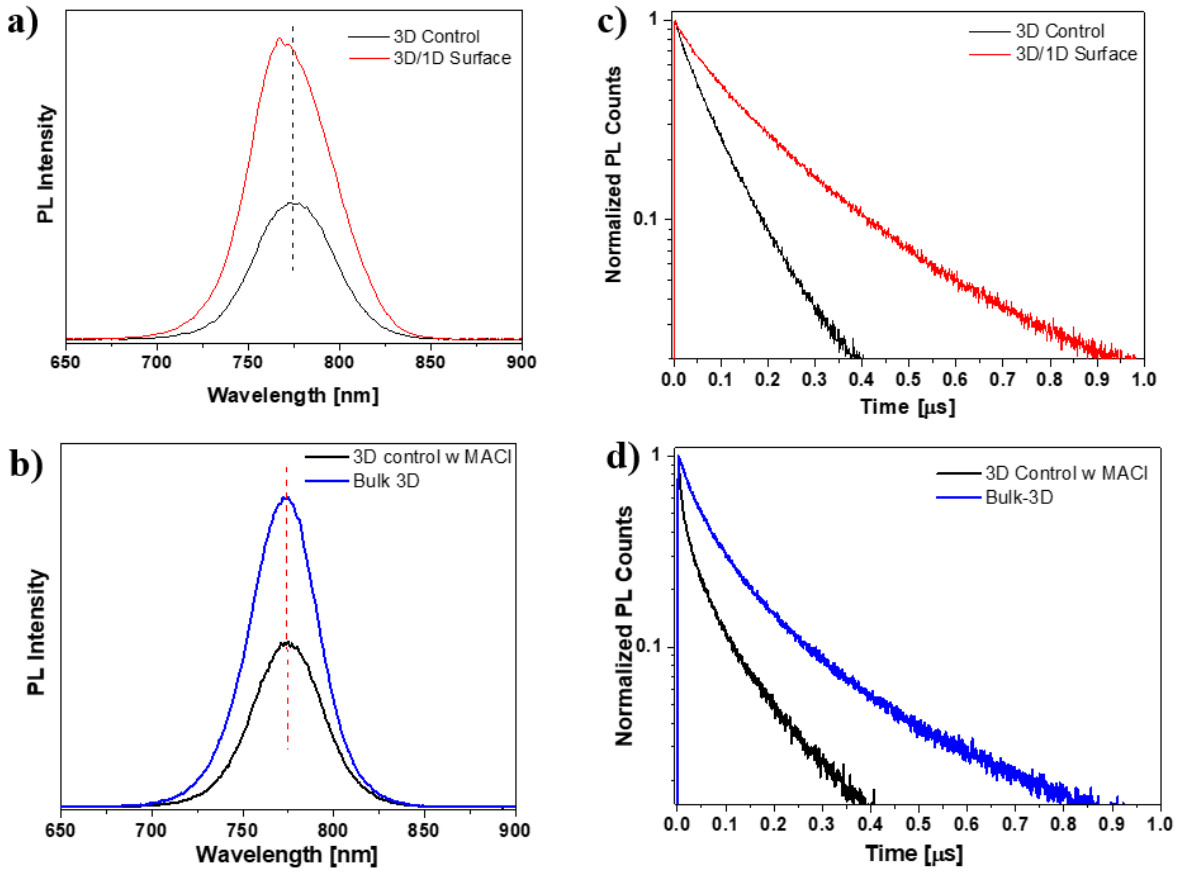

Figure 7. a, b) SSPL and TRPL spectra of 3D MAPI control and surface-passivated 3D/1D film, c, d) SSPL and TRPL spectra of 3D control with MACl and bulk-passivated 3D film.

In the 3D control film, the τ_1 and τ_2 values are equal to 50 and 114 ns, respectively. The values τ_1 and τ_2 of both bulk-passivated 3D and surface-passivated 3D/1D films are significantly extended compared to the control sample. The low τ_1 value indicates that the trap-assisted nonradiative recombination is reduced and radiative recombination of carriers dominates the PL decay in the bulk-passivated 3D and 3D/1D phases.[68]

The trap-state density of the corresponding films was quantified by the space-charge-limited current (SCLC) method for electron/hole-only devices, using the following equation (2):

$$N_t = 2\varepsilon\varepsilon_0 V_{TFL}/qL^2 \quad (2)$$

where N_t is the trap-state density of electron or hole, ε is the relative dielectric constant of MAPI perovskite (ε = 25), ε_0 is vacuum permittivity (8.85×10^{-12} F m^{-1}), V_{TFL} is the trap-filled limit voltage, q is elementary charge (1.602×10^{-19} C) and L is the thickness of the perovskite film.[69] Electron-only devices were fabricated for this measurement and dark *J-V* curves were recorded (**Figure S14,** Supporting Information). The linear region seen in the dark *J-V* curve at low bias

voltage is the ohmic region. The intermediate bias region where the traps are filled with the charge carriers is known as the trap-filled region. The trap-free region is defined at the high-bias voltage. The V_{TLF} is determined as the bias voltage at the inflection point between the ohmic region and the trap-filled region. The calculated trap state density of the 3D MAPI control device is 7.58×10^{15} cm $^{-3}$. For the surface-passivated 3D/1D device, the trap-state density is calculated to be 6.18×10^{15} cm $^{-3}$. The lower trap-state density in the surface-passivated 3D/1D perovskite device confirms that the low-dimensional 1D phase has a passivation effect and reduces the traps in the corresponding devices. In the case of bulk-passivated 3D perovskite the trap-state density was found to be 1.20×10^{16} cm $^{-3}$, and for the 3D MAPI control with the same device architecture it was found to be equal to 1.31×10^{16} cm $^{-3}$. These results suggest that in the bulk-passivated 3D film the ThPyI also acts as a passivator for the trap states, albeit with more moderate effect.

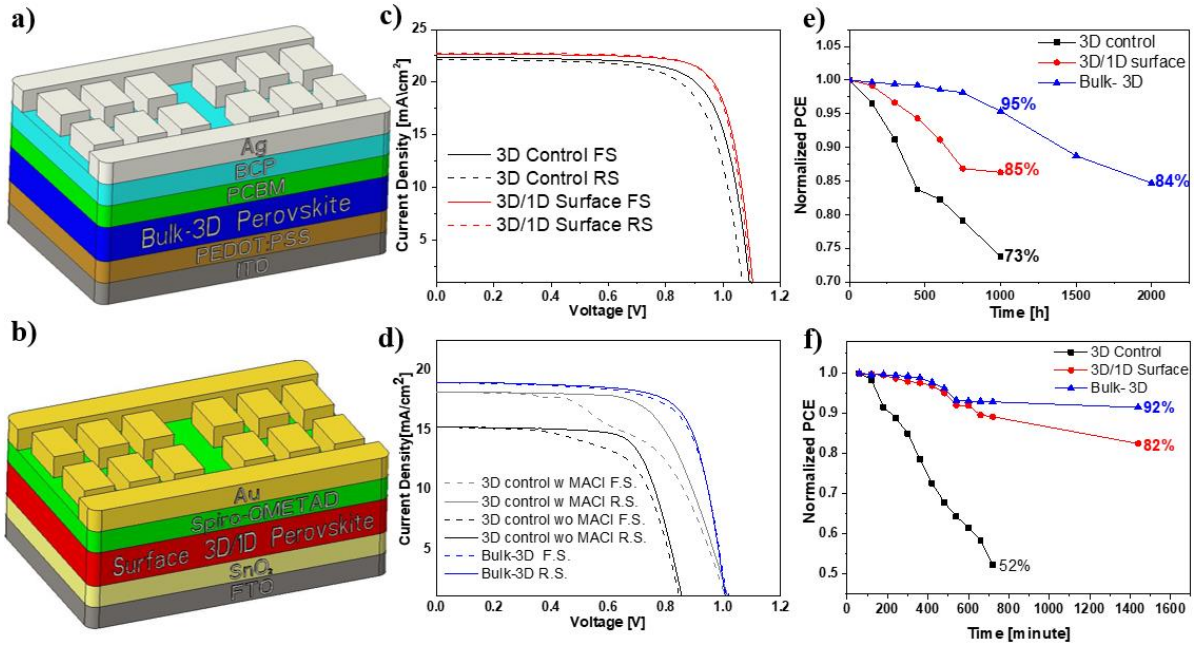

Figure 8. Device structure of a) bulk-passivated 3D and b) surface-passivated 3D/1D perovskite devices. c, d) *J-V* curves of surface-passivated 3D/1D and bulk-passivated 3D perovskite devices e) long-term stability, and f) light-thermal stability of 3D control, surface-passivated 3D/1D, and bulk-passivated 3D devices.

To evaluate further the effect of the 1D phase on the photovoltaic performance, the normal (*n-i-p*) planar perovskite solar cells for the 3D MAPI control and the surface-passivated 3D/1D phases were fabricated as shown in **Figure 8a**. The device architecture of bulk-passivated 3D MAPI was kept inverted (*p-i-n*) because of the need for better energy alignment between the

different layers given in **Figure 8b.** As noted above, to increase the preferential orientation of perovskite slabs, MACl was used as an additive which plays an important role in improving the PCE of bulk-passivated 3D MAPI. Bulk-passivated 3D devices with and without MACl were fabricated for the purpose of comparison. Devices with the MACl/MAI 0.5 weight ratio show the highest performance (**Figure S15,** Supporting Information**)**. The results of photovoltaic *J-V* characterization of the optimized devices, performed under AM 1.5G (1000 W/m^2), are presented in **Figure 8c, d** and **Table S6 (**Supporting Information). Moreover, statistical distributions of the photovoltaic parameters are given (**Figure S16,** Supporting Information).

The 3D MAPI control perovskite film yielded a short-circuit current density (J_{sc}) of 22.35 mA/cm^2, an open-circuit voltage (V_{oc}) of 1.09 V, and a fill factor (*FF*) of 74%, which gives an overall PCE equal to 18.08% (for the best performing device). As seen in the forward and backward scans, the 3D control device suffers from hysteresis. On the other hand, the surface-passivated 3D/1D device exhibits a higher PCE (19.60%) with improved V_{oc} of 1.11 V, J_{sc} of 22.69 mA/cm^2, and a FF of 78%. The improved V_{oc} suggests that the low-dimensional 1D phase grown at the grain boundaries of the 3D perovskite suppresses the trap-assisted recombination that is associated with surface defects. As for the optimized bulk-passivated 3D MAPI perovskite, the overall PCE was 14.10% with a J_{sc} of 18.98 mA/cm^2, V_{oc} of 1.02, and FF of 74% (For the best performing device). Hence, the efficiency of bulk-passivated 3D MAPI devices is lower than that of the surface-passivated 3D/1D perovskite device, presumably since it contains a high fraction of organic passivation agent (ThPyI: PbI_2; 2:3 mole ratio). We note that this is one of the first studies where 3D MAPI perovskite is prepared with a high volume fraction of organic agents in bulk-passivated perovskite solar cells.

The stability of the unencapsulated devices was studied under ambient conditions in air (room temperature, relative humidity 40-45%) as shown in **Figure 8c.** The surface-passivated 3D/1D perovskite device retained 86% of its PCE after a 1000 h stability test (under dark) whereas the PCE of the 3D control device dropped to 74% of its original PCE. On the other hand, the bulk-passivated 3D perovskite device showed the best environmental stability among these devices, keeping 95.3% of its initial PCE after 1000 h, and 84% after 2000 h under N_2 atmosphere (dark). Furthermore, a combined light-thermal stability test of the corresponding devices was conducted under one sun at 60 °C for 24 h under N_2 atmosphere. The bulk-passivated 3D device also showed the highest light-thermal stability by retaining 92% of its initial efficiency under

continuous light soaking after 24 h as shown in **Figure 8d**. In comparison, the initial PCE of surface-passivated 3D/1D and 3D MAPI control devices decreased to 82% and 52%, respectively. The improved stability of the surface-passivated 3D/1D device is attributed to the presence of the low-dimensional 1D phase, which is proposed to inhibit ion migration, moisture penetration, to improve film quality, and to reduce defects in the perovskite film. On the other hand, the high-volume fraction of hydrophobic ThPyI spacer used in the bulk-passivated 3D MAPI film should efficiently prevent moisture penetration, which apparently explains the higher stability. Remarkably, and in line with this assessment, the bulk-passivated 3D MAPI film retained its structure in air for four months after which time only a very weak diffraction peak of PbI_2 emerged (**Figure S17,** Supporting Information).

To find out the impact of the ThPyI-based low-dimensional new phase treatment on the hydrophobicity, the water contact angles of 3D $MAPbI_3$ control, 1D perovskitoid, surface-passivated 3D/1D, and bulk-passivated 3D perovskite films were measured. (**Figure S18,** Supporting Information). The pure 1D perovskitoid shows the highest water contact angle of around 73° compared to the others. As compared to the 3D $MAPbI_3$ control with an angle of 60°, the surface- and bulk-treated forms of the 3D perovskite films exhibit increased water contact angles of around 67° and 69°, respectively. The greater water contact angles of the 1D and treated 3D perovskite films compared to the 3D $MAPbI_3$ control reveal the enhanced hydrophobicity of the treated forms of the 3D perovskite.

The same films that were evaluated in the water contact angle measurements were immersed in water to further solidify their behavior in water. As expected, 3D control $MAPbI_3$ and its surface- and bulk-treated 3D films were decomposed into PbI_2 in a few seconds, which shows it with the characteristic yellow color of PbI_2. Interestingly, in the 1D film, no changes related to the color was observed. After removing the samples from the water and drying the corresponding films, XRD measurements were carried out to understand their behavior in water (**Figure S19,** Supporting Information). In comparison with the 3D control film and its treated forms, which show complete decomposition into PbI_2, the ThPyI-based low-dimensional pure new phase shows no decomposition. These water contact angle measurements and XRD diffractions of the water-immersed films show the water stability of the 1D phase compared with its 3D counterparts.

3.3. Conclusions

In summary, a novel thiophene based ThPyI organic spacer with heterocyclic structure was developed and used both as a defect passivator and as an organic spacer in surface- and bulk-passivated 3D MAPI-based perovskite devices. Our results demonstrate that the ThPyI organic spacer is a suitable candidate for creating 1D perovskitoids in perovskite-based photovoltaic devices. TRPL results showed that the fluorescence lifetimes in both passivated devices become longer and contribute to the better performance. Moreover, the ThPyI based perovskite devices offered high efficiency and environmental stability compared to their 3D counterparts. The bulk-passivated 3D PV devices showed significantly higher environmental as well as light-thermal stability even compared to the surface-passivated devices. Importantly, this novel organic agent promoted the preferential orientation of the 3D perovskite slabs crystalline orientation (vertical orientation of the (110) planes with respect to the substrate) in the films much more efficiently than the MACl additive. This study enriches the literature on thiophane-based organic spacers and presents a different perspective on organic spacer design. We envision that the above results can help to bring on a rational strategy for the design of organic agents that play a multiple role as defect passivator, crystalline orientation promoter and organic spacer for various perovskite-based solar cells.

3.4 Experimental Section

Materials and reagents

The SnO_2 colloid precursor was purchased from Alfa Aesar (tin (IV) oxide, 15% in H_2O colloidal dispersion). Before spin-coating as an ETL, the SnO_2 nanoparticles were diluted with DI water to 2.67 wt.%. The organic spacer precursor 2-(2-thienyl) pyridine (unprotonated form), as well as PbI_2 and MAI were purchased from TCI. MACI, BCP, solvents (DMSO, DMF, etc.) and freshly delivered hydroiodic acid (HI ~57 wt.%) were purchased from Sigma-Aldrich. The Spiro-OMeTAD used as an HTL material was purchased from Borun Chem. The PEDOT:PSS aqueous solution and $PC_{61}BM$ were purchased from Ossila.

Solar cell fabrication:

Fabrication of bulk-passivated 3D MAPI solar cell

ITO substrates (3 cm x 3 cm) were first etched using 3 M HCl and Zn powder and later rinsed with deionized water. This was followed by sonication of the substrates in 2% *detergent (*Hellmanex™ III) aqueous *solution*, DI water, ethanol, and isopropanol for 15 min each, respectively. Afterwards the substrates were dried in nitrogen flow and treated with nitrogen plasma for 15 min. PEDOT: PSS was spin-coated onto pre-cleaned ITO substrates at 2500 rpm for 40 s and annealed at 140 ℃ for 20 min in air. After this process, the substrates were transferred into a glovebox for device fabrication.

Bulk-passivated 3D perovskite precursor solution was prepared from the stoichiometric ratio of PbI_2, MAI and ThPyI at molar ratio 3:2:2, respectively, in a 1 ml DMF: DMSO (8:1 volume ratio) mixture. For the devices where MACI was used as an additive for preferential crystal orientation, the amount of MACl was adjusted to MACl/MAI 0.5 wt.%. The prepared solution was stirred for 12 h at 70 ℃ . The prepared bulk-passivated 3D perovskite solution was spin coated onto ITO/PEDOT:PSS substrate at 6000 rpm for 40 s. Toluene (350 µl) was dropped onto the perovskite film during the last 15 s of the spin-coating process, followed by heat treatment at 100 ℃ for 15 min. $PC_{61}BM$ (20 mg/mL in CB) and BCP (0.6 mg/mL in IPA) were spin-coated subsequently onto the perovskite active layer at 1000 rpm for 30 s, respectively. In the last step, a 100 nm thick silver electrode was thermally evaporated under vacuum ($1x10^{-6}$ Pa). The active area was fixed to 0.0831 cm^2 using a metal mask. 3D MAPI control devices with and without MACI were fabricated using similar steps as given above but without using ThPyI in the precursor solutions.

Solar cell fabrication with surface-passivated 3D/1D perovskite

FTO substrates (3 cm x 3 cm) were first etched using 3 M HCl and Zn powder and later rinsed with deionized water. This was followed by sonication of the substrates in 2% *detergent (*Hellmanex™ III) solution, DI water, ethanol, and isopropanol for 15 min each, respectively. Afterwards the substrates were dried in nitrogen flow and treated with nitrogen plasma for 15 min. A diluted SnO_2 nanoparticle solution (2.67 wt% in water) was spin-coated onto the FTO substrate in air at 4000 r.p.m. for 35 s, and then annealed in air at 150 ^oC for 30 min. Before the perovskite coating, the SnO_2 coated substrates were cleaned once again using the UV-O_3 environment for 10 min. Using the one-step "anti-solvent" method, the precursors of the perovskite – PbI_2 (1.68 M, 5% excess), MAI (1.60 M), and DMSO (1.60 M) in 1 mL DMF were deposited on top of the SnO_2 layer at 1000 rpm for 10 s, followed by fast spinning at 3500 rpm for 20 s. Ethyl acetate as an anti-solvent was dropped onto the perovskite film during the last 10 s while spinning. The sample was then annealed at 130 ^oC for 10 min. For the surface treatment, the 2-(thiophen-2-yl) pyridin-1-ium iodide salt in isopropanol solution (3.9 mg/ml) was spin-coated onto the perovskite films at 1000 r.p.m for 30 s followed by 5000 r.p.m for 5 s. This was followed by heat treatment of the latter substrate at 100 ^oC for 10 min. The hole transport material (HTM) was deposited by spin-coating (3000 rpm for 30 s) a solution containing 72.3 mg spiro-OMeTAD, 35 μl bis(trifluoromethane) sulfonimide lithium salt (LiTFSI) stock solution (270 mg LiTFSI in 1 ml acetonitrile), 30 μl 4-*tert*-butylpyridine and 1 ml chlorobenzene. Finally, a 70 nm thin film of Au was thermally evaporated under high vacuum on top of the HTM layer.

General characterization techniques:

UV–vis absorption (UV-vis)*:* were recorded using a Perkin Elmer Lambda 1050 spectrometer with an integrating sphere. Time-resolved photoluminescence

Photoluminescence (PL): spectroscopy was performed with a Picoquant Fluotime 300 spectrofluorometer using an excitation wavelength of 375 nm. Current-voltage (*J-V*) characteristics were measured under ambient conditions using a Newport OrielSol 2A solar simulator (AM 1.5G - 100 mW cm^{-2}) and a Keithley 2400 source meter.

The solar simulator: was calibrated with a Fraunhofer ISE certified silicon cell (KG5-filtered). The active area of the solar cells was defined by a square metal aperture mask with an area equal to 0.0831 cm^2. *J-V* curves were recorded by scanning the input bias from -0.1 V to 1.2

V(forward scan) at a scan rate of 0.1 V/s after the devices had been at 1.2 V for 5 s under illumination. For the light intensity-dependent *J-V*-measurements, a white light LED was used as a light source. The LED intensity was adjusted with a Keithley 2200-20-5 Power Supply. A highly linear photodiode was used to control the light intensity over a range of 0.1 – 1.2 suns. *J-V*-curves were measured with a Keithley 2401 source meter.

External Quantum Efficiency (EQE): To obtain the EQE spectra, the PV cells were illuminated with a chopped light (tungsten lamp) and the beam was passed through a monochromator. Further, the light beam was split to illuminate the sample as well as a reference silicon photodetector (Hamamatsu S2281-01) at the same time. The resulting wavelength-dependent current response of both devices was recorded simultaneously by two lock-in amplifiers (Signal Recovery 7265, Stanford Research Systems 830) at a chopping frequency of 14 Hz. The incident illumination power, determined via the reference photodetector, was used to calculate the EQE response of the perovskite solar cell.

X-Ray Diffraction (XRD): (XRD) measurements were performed with a Bruker D8 Discover X-ray diffractometer operating at 40 kV and 30 mA. The diffracted X-ray beam was passed through a Ni filter. The Cu Kα1 radiation (λ = 1.5406 Å) and a position-sensitive LynxEye detector were used.

Powder X-Ray Diffraction (P-XRD): P-XRD measurements were carried out on a STOE STADI P diffractometer in Debye–Scherrer geometry, operating at 40 kV and 40 mA, using monochromated (Ge(111) single crystal monochromator) Cu-$K_{\alpha1}$ radiation (λ = 1.5406 Å) and a DECTRIS MYTHEN 1K detector.

Grazing-incidence wide-angle X-ray scattering (GIWAXS): GIWAXS data measurements were performed on an Anton-Paar Saxspoint 2.0 with a Primux 100 microfocus source with Cu-$K_{\alpha1}$ radiation (λ = 1.5406 Å) and a Dectris Eiger R 1M 2D Detector.

Scanning Electron Microscopy (SEM): For SEM, an FEI Helios Nanolab G3 UC DualBeam scanning electron microscope (SEM) equipped with an Oxford Aztec Advanced X-Max 80 EDX detector was used. SEM images were recorded at an acceleration voltage of 2 kV. Top view images were recorded using both a backscattered electron detector and a secondary electron through-the-lens detector.

***HR-TEM studies*:** Transmission electron microscopy (TEM) studies were carried out with a JEOL 2100F instrument operating at 200 kV. MAPI perovskite thin films (without MACI)

were used as source material. Sample preparations were achieved by removing perovskite from the substrate and transferring it on the surface of a lacey coated copper TEM grid.

***Single-Crystal X-Ray Diffraction (SC-XRD)*:** The frames were integrated with the Bruker SAINT software package.[70] Data were corrected for absorption effects using the Multi-Scan method (SADABS).[71]. The structure was solved and refined using the Bruker SHELXTL Software Package.[72] All hydrogen atoms have been calculated in ideal geometry riding on their parent atoms. The structure has been refined as a 2-component inversion twin. The domain volume ratio refined to 0.87/0.13. The disorder of the organic cation has been described by a split model. The ratio of site occupation factors of the two disordered parts refined to 0.58/0.42. All atoms of the organic cation have been refined isotropically. Atoms of the main part have been used as geometrical model for the minor part (SAME instruction in SHELX). The SIMU restraint has been applied for disordered atoms with a distance of 0.8 A or closer. The figures have been drawn at the 25% ellipsoid probability level.[73] In the case of disorder the less-occupied parts have been neglected for the figures.

Crystallographic data have been deposited with the Cambridge Crystallographic Data Centre, CCDC, 12 Union Road, Cambridge CB21EZ, UK. Copies of the data can be obtained free of charge on quoting the depository numbers CCDC-2237540 (https://www.ccdc.cam.ac.uk/structures/).

Nano-FTIR: For nano-FTIR measurements, a commercially available near-field microscope (neaSNOM, Neaspec) was used. For this technique, based on scattering-type scanning optical near-field microscopy (s-SNOM), a sharp, metal-coated AFM tip was illuminated by a broadband IR source. The light backscattered from the oscillating metallic tip was analyzed with an asymmetric Fourier transform spectrometer, which was based on a Michelson interferometer.[4] This allowed for the simultaneous recording of optical amplitude and phase of the backscattered light. To suppress the background light the tip was oscillated harmonically with a small tapping amplitude A and frequency Ω (here A = 65 nm, Ω = 247 kHz) and the detector signal was demodulated at higher harmonics $n\Omega$ of this frequency. For $n \geq 2$ the background is completely suppressed, delivering local near-field amplitude and phase spectra. To eliminate the microscope response function, the spectra were normalized to the spectra obtained from a spectrally flat reference (Si substrate). This resulted in local reflectivity and absorption spectra of the investigated materials. The latter was used for chemical identification according to standard FTIR databases.[5]

To record the nano-FTIR data, silicon wafer (2.5 cm X 2.5 cm) substrates were used. The substrates were sonicated in 2% *detergent* solution, DI water, ethanol, and isopropanol for 15 min each, respectively. Subsequently, dried substrates were further cleaned via ultraviolet ozone treatment for 15 min before the perovskite coating. The architecture of the thin film follows the order: silicon wafer/$MAPbI_3$/ w/-, w/o the 2-(thiophen-2-yl)pyridin-1-ium iodide salt. Neat perovskite and surface treated perovskite films were fabricated using the same method employed for solar cell fabrication.

Space-Charge Limited Current (SCLC): To evaluate the surface passivation effects on trap-density via the space-charge limited current (SCLC) method, electron-only devices were prepared with the device configuration of ITO/SnO_2/$MAPbI_3$ w or wo ThPyI /PCBM/Au. For bulk-passivated 3D MAPI, the electron-only device configuration is ITO/SnO_2/ Perovskite with MACl w or wo ThPyI /PCBM/BCP/Ag.

Ultraviolet Photoelectron Spectroscopy (UPS). Photoelectron spectroscopy was performed with a PHI 5000 VersaProbe at the Clustertool at InnovationLab GmbH in Heidelberg. The samples were introduced from the glovebox with exposures to air <1 min. UPS was carried out with a He-discharge lamp using the He-I emission with an energy of 21.22 eV. Pass energies of 2.95, and 0.59 eV were used for UPS valence band and UPS secondary electron cut-offs, respectively. For the measurements of the secondary electron cut-off, a bias of −5 V was applied. The take-off angle for all measurements was 90°. The Fermi level of clean silver (Ar sputtered) was used to calibrate the UPS data.

Syntheses:

Synthesis of 2-(thiophen-2-yl)pyridin-1-ium iodide salt

The organic spacer precursor (2g, 12.16 mmol) – 2-(2-thienyl)pyridine (unprotonated form) – was dissolved in 20 ml IPA. After cooling down to 0 °C in an ice bath, subsequently hydriodic acid ~57 wt.% (1.93 ml, 14.59 mmol) was dropped into the solution. After stirring at 0 °C for 2 h, a yellowish precipitate was observed and then collected by filtration. Collected solids were washed with diethyl ether for three times, dried under vacuum at 50 °C for 24 h to afford the yellowish solid product (3.24 g 92 % yield). ^{1}H NMR (400 MHz, DMSO-d_6) δ 8.62 (ddd, J = 5.3, 1.7, 1.0 Hz, 1H), 8.14 – 8.03 (m, 2H), 7.92 (dd, J = 3.7, 1.2 Hz, 1H), 7.80 (dd, J = 5.0, 1.2 Hz, 1H), 7.50 (ddd, J = 6.9, 5.2, 1.7 Hz, 1H), 7.24 (dd, J = 5.0, 3.7 Hz, 1H), 7.13 (s, 1H). ^{13}C NMR (101 MHz, DMSO) δ 149.47, 146.65, 140.68, 140.29, 130.38, 128.85, 127.59, 123.21, 120.79. HRMS (ESI, m/z): calculated for $C_9H_8NS^+$ 162.04; found 162.03733 $[M+H]^+$.

Synthesis of single crystals

PbI_2 (0.3 M) and 2-(2-thienyl)pyridine, unprotonated form) (0.3 M) were mixed in a round bottom flask in fresh hydriodic acid ~57 wt.% (20 mL) and stirred at room temperature for 10 minutes. Subsequently, the resulting mixture was heated up to 140 °C and stirred at this temperature for 1 h. After stirring for 1 h, the transparent yellow solution was slowly cooled down to room temperature. During the cooling, at about 110 °C, yellow needle-shape crystals were observed in the solution. The needle-shaped crystals were collected by filtration to remove unreacted PbI_2, which is soluble in the reaction mixture, and subsequently washed several times with diethyl ether. Finally, they were dried at 60 °C in air for 24 h.

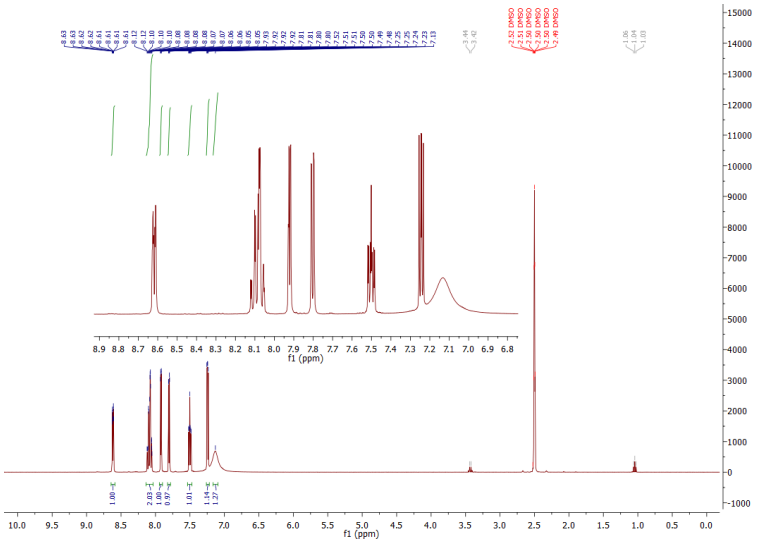

Figure S1a. ^{1}H-NMR spectra of ThPyI organic spacer

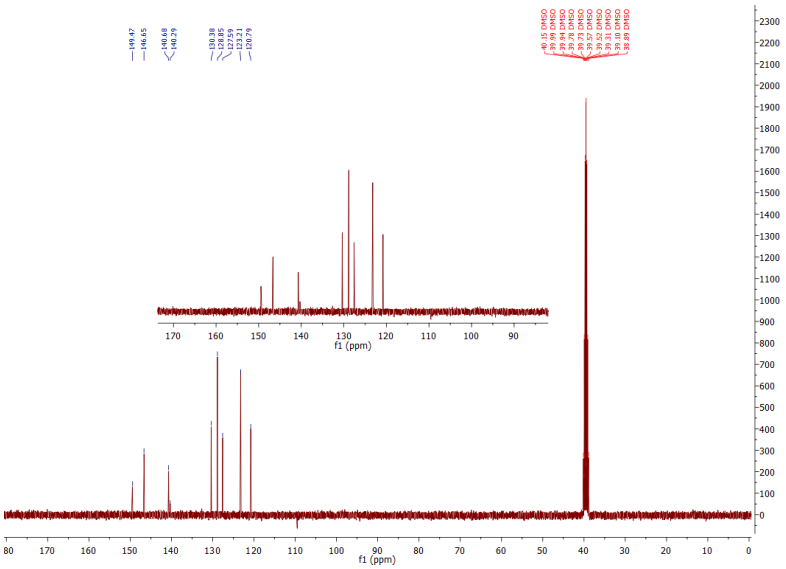

Figure S1b. ^{13}C-NMR spectra of ThPyI organic spacer

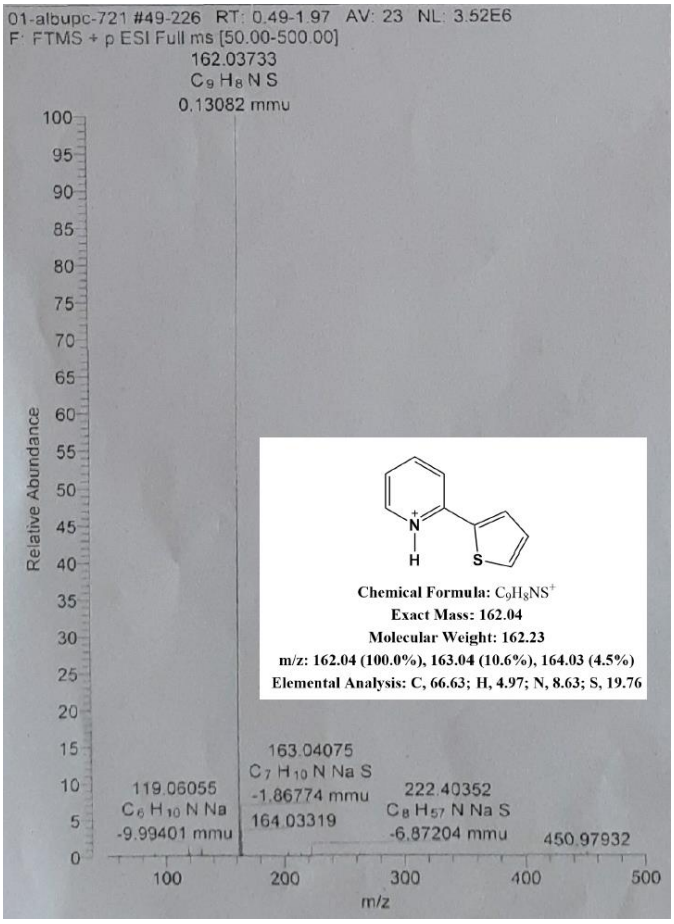

Figure S1c. Mass spectrum of ThPyI organic spacer with a distinctive *m/z* peak at 162.037.

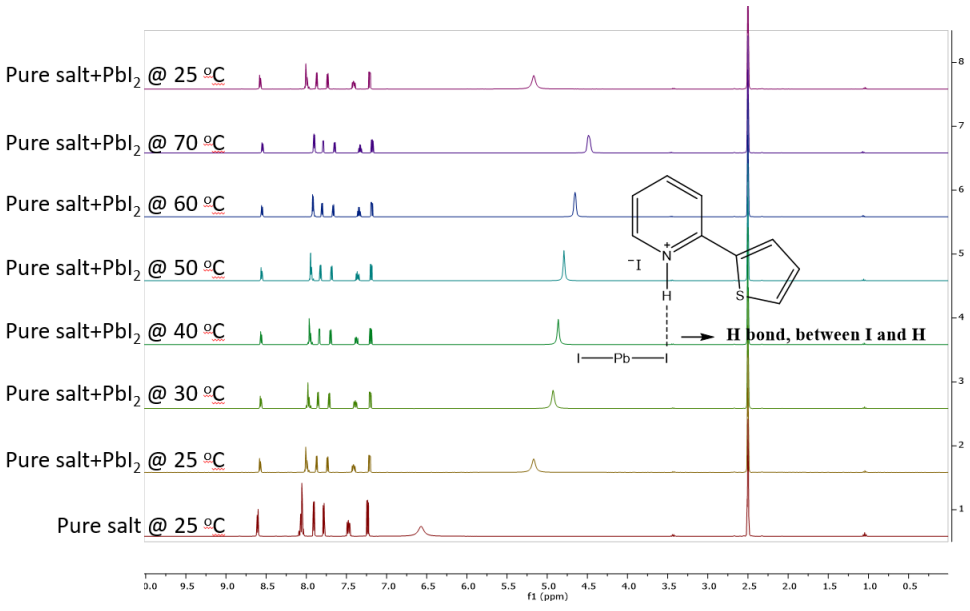

Figure S1d. ^{1}H-NMR spectra of PbI_2 + ThPyI mixture at different temperatures

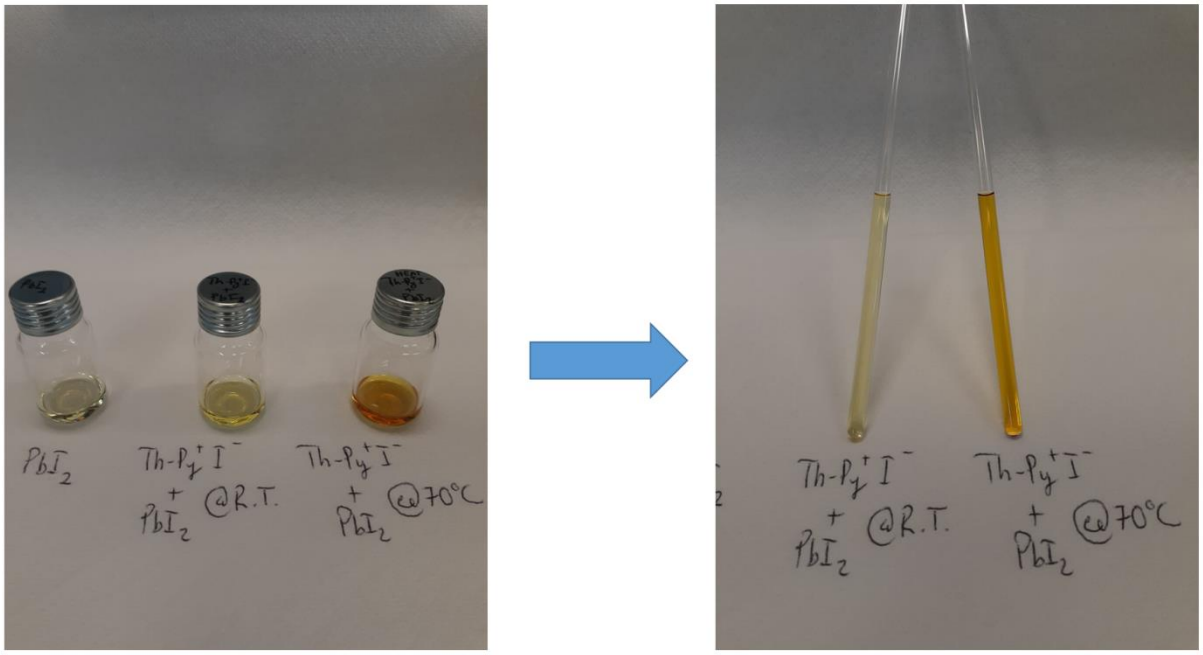

Figure S1e. Photos of the PbI_2 + ThPyI mixture after heating at different temperatures.

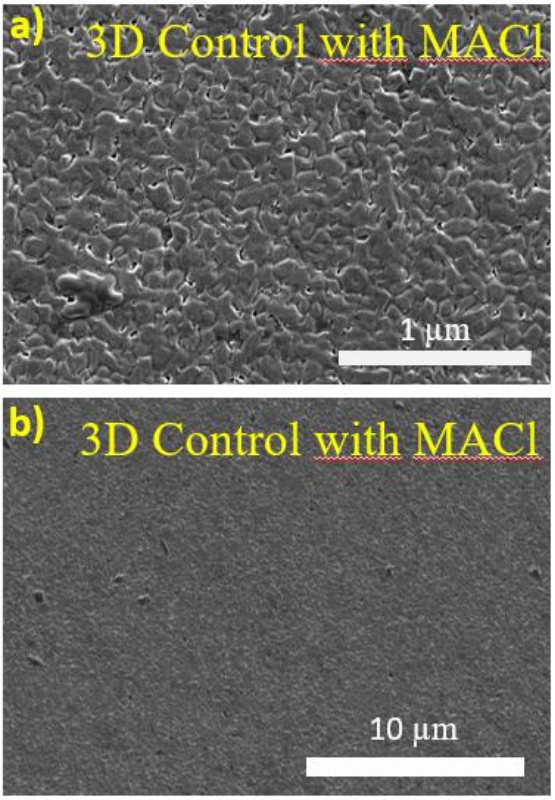

Figure S2. SEM images of a, b) 3D control with MACl.

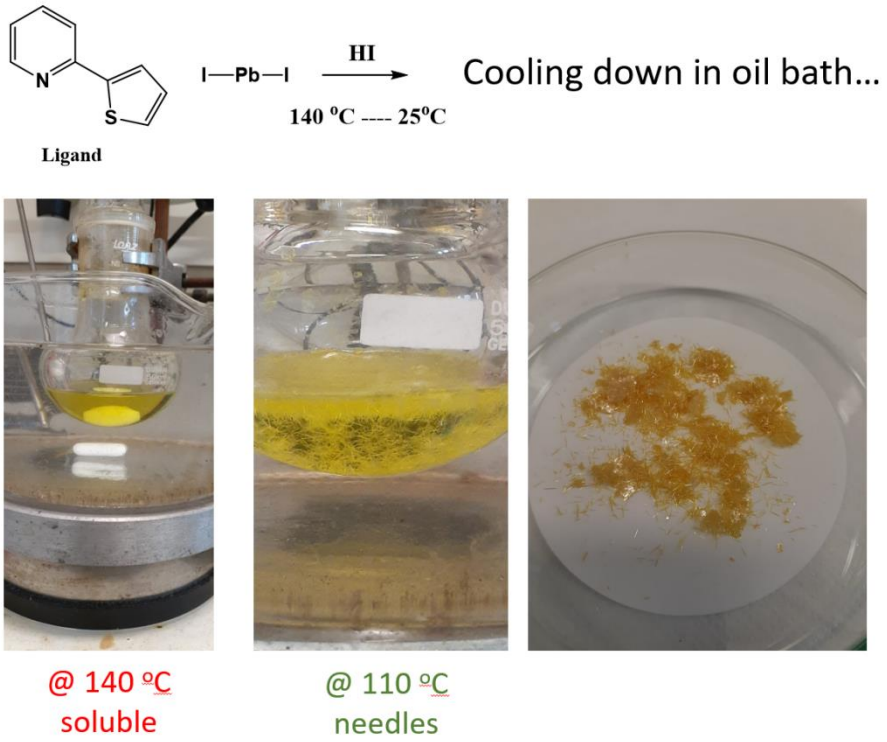

Figure S3. Photos of the 1D single crystals forming during the synthesis.

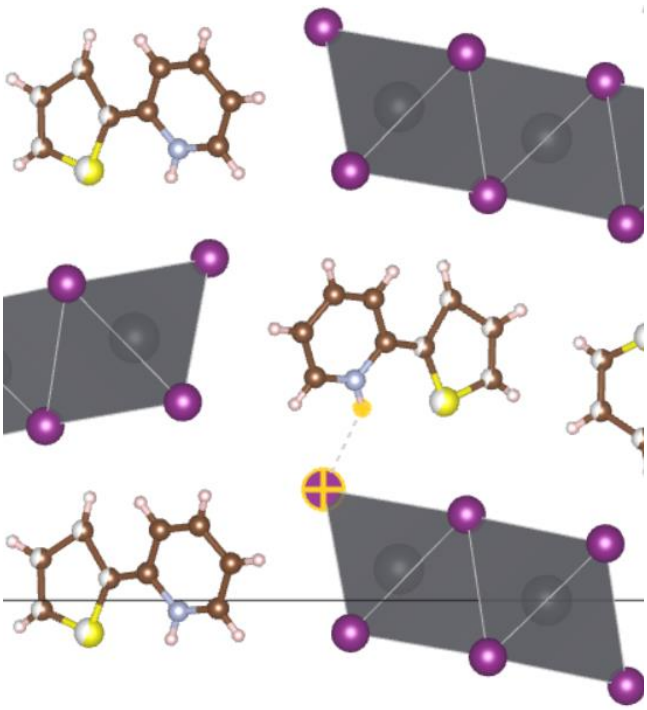

Figure S4. N^{+}-H···I-PbI_5 hydrogen-bonding interaction (l(H1-I4) = **2.8118(2) Å**

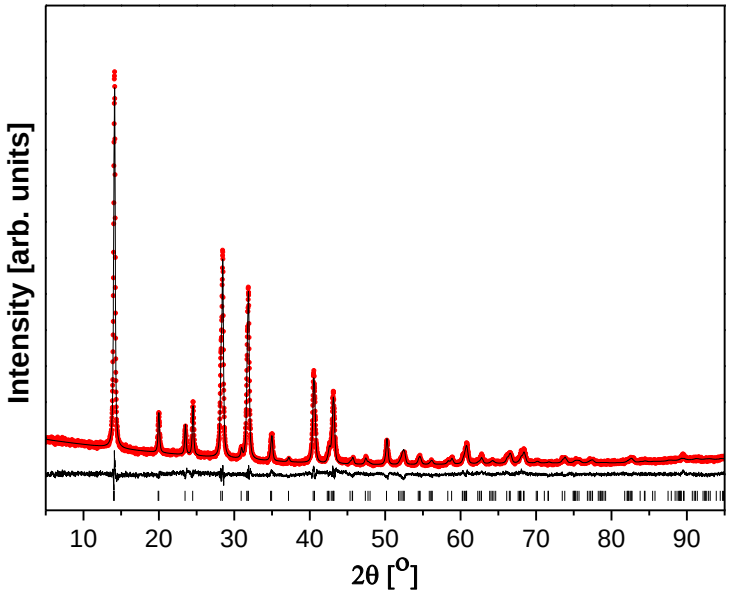

Figure S5. Rietveld plot for the 3D-control sample. Red dots – Y_{obs}, black line – Y_{calc}, line below – Difference, Vertical bars – Bragg positions.

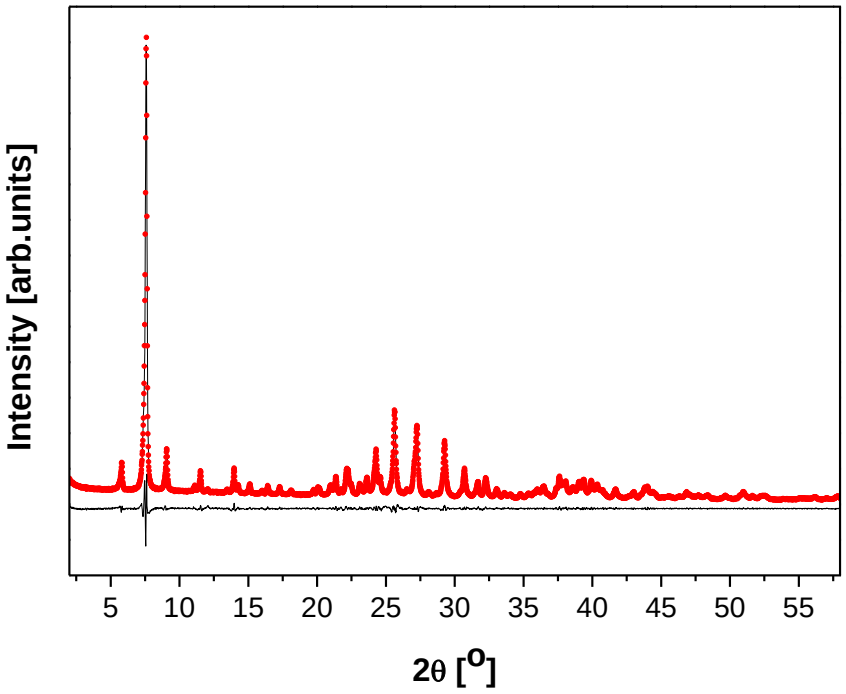

Figure S6. Le Bail Profile fitting of powder diffraction pattern of the1D film.

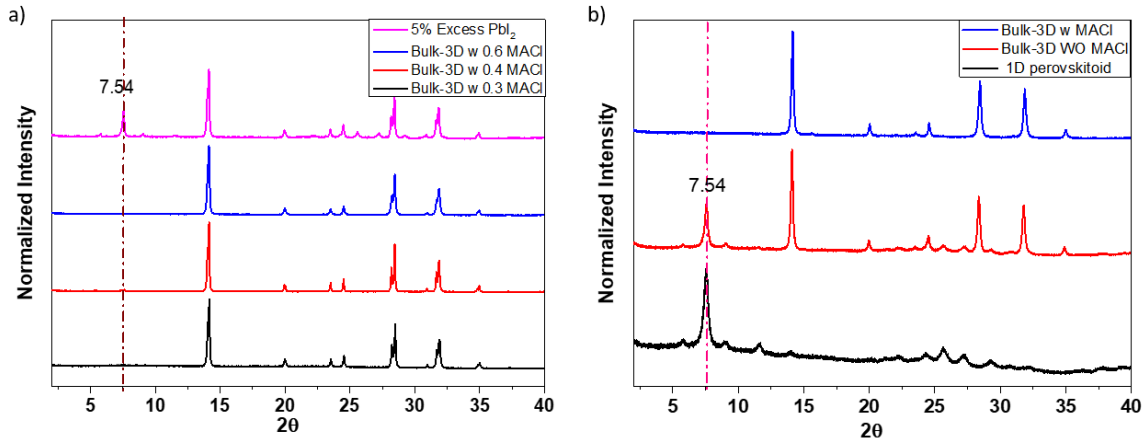

Figure S7. a) Powder XRD patterns of bulk-passivated 3D MAPI with different amount of MACl added (MACl/MAI wt. ratio) b) XRD patterns of 1D and bulk-passivated 3D perovskite with MACI (MACl/MAI (0.5 wt. ratio) and without MACI.

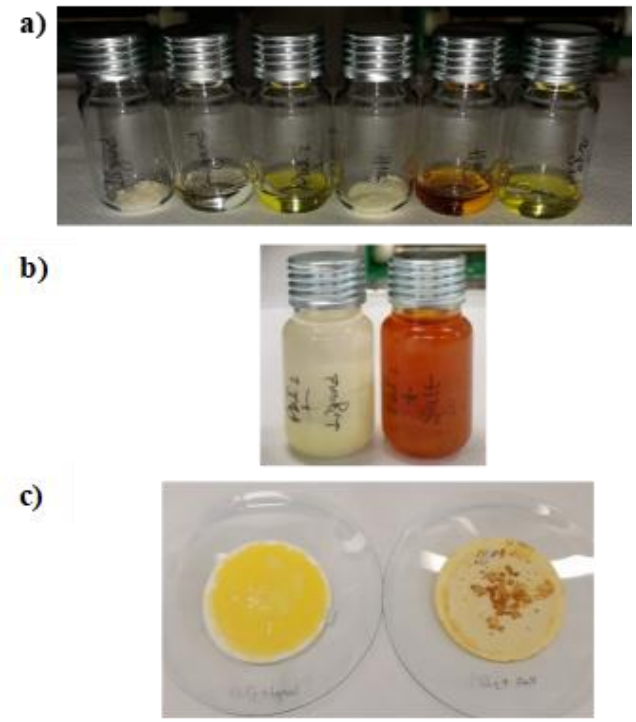

Figure S8. Left to right: a) Photos of the ThPy ligand (unprotonated form of the organic salt) in its pure (solid) form, its solution form in DMF, and its mixture with PbI_2 in DMF; photos of the ThPyI (organic salt) in its pure (solid) form, its solution form in DMF, and its mixture with PbI_2 in DMF. b) Photos of the mixtures of PbI_2 + ThPy, and PbI_2 + ThPyI in DMF with a large amount of toluene, which was stirred at room temperature for 1 hour. c) Photos of the PbI_2 + ThPy, and PbI_2 + ThPyI precipitates in powder forms which were many times washed with toluene and isopropanol to remove unreacted ligand and its salt form, respectively, dried under vacuum at room temperature for 24 hours.

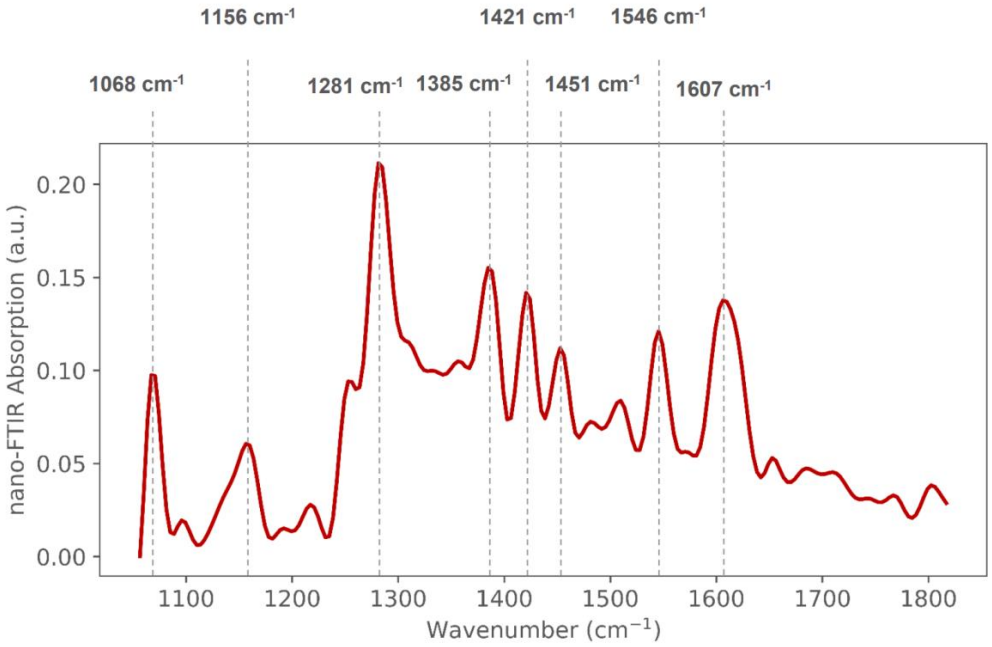

Figure S9. Nano-FTIR Spectra of pure ThPyI.

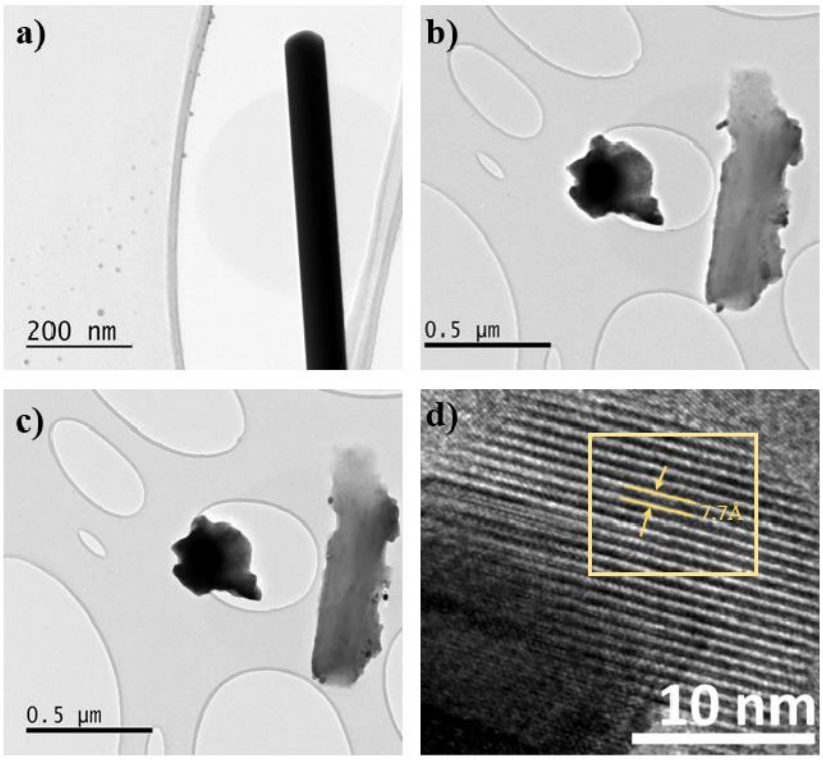

Figure S10. TEM images of bulk-passivated 3D (with MACI) perovskite film.

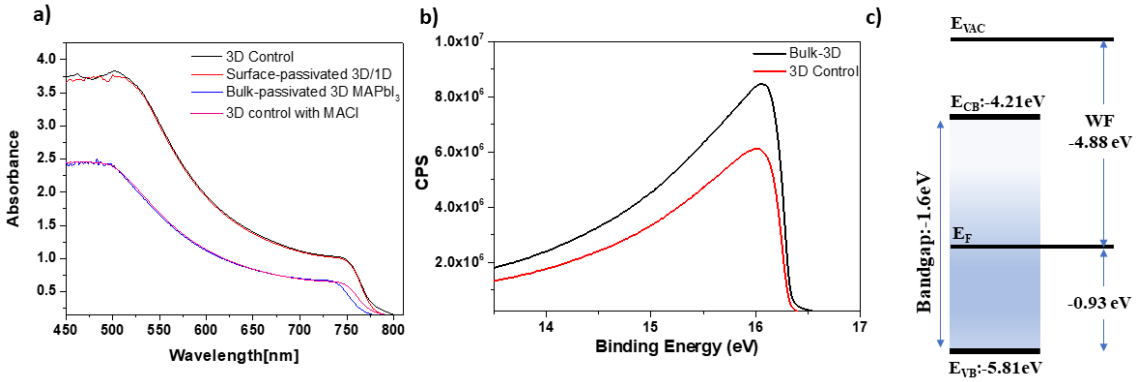

Figure S11. Absorption spectra of 3D MAPI control, surface-passivated 3D/1D and bulk-passivated 3D MAPI. b) Helium Iα ($h\nu$ = 21.22 eV) spectra of SE (secondary electron) cutoff of bulk-passivated 3D perovskite films. c) Schematic energy level diagrams of bulk-passivated 3D perovskite film.

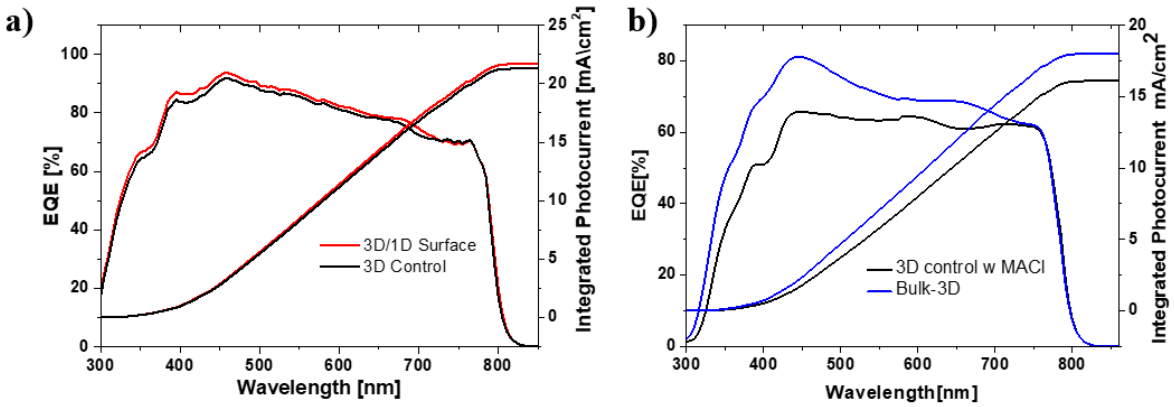

Figure S12. a) EQE of 3D MAPI Control and 3D/1D surface passivated device, b) EQE of 3D MAPI control with MACl and bulk-passivated 3D perovskite.

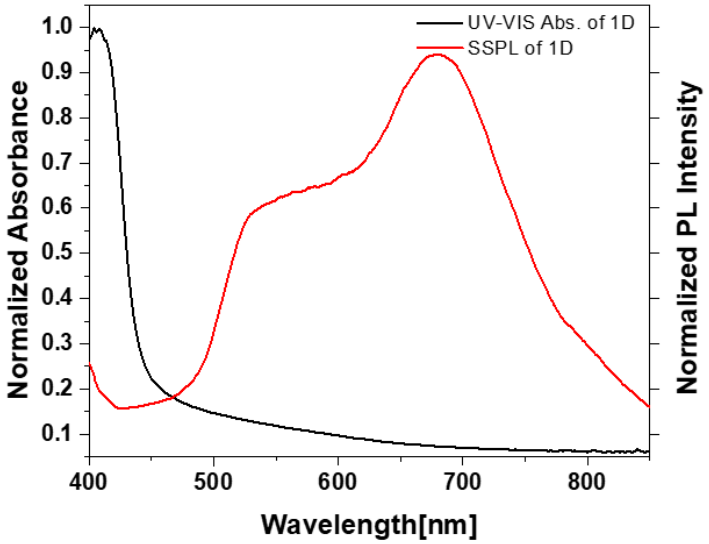

Figure S13. Absorption spectra and SSPL spectra of the1D perovskitoid.

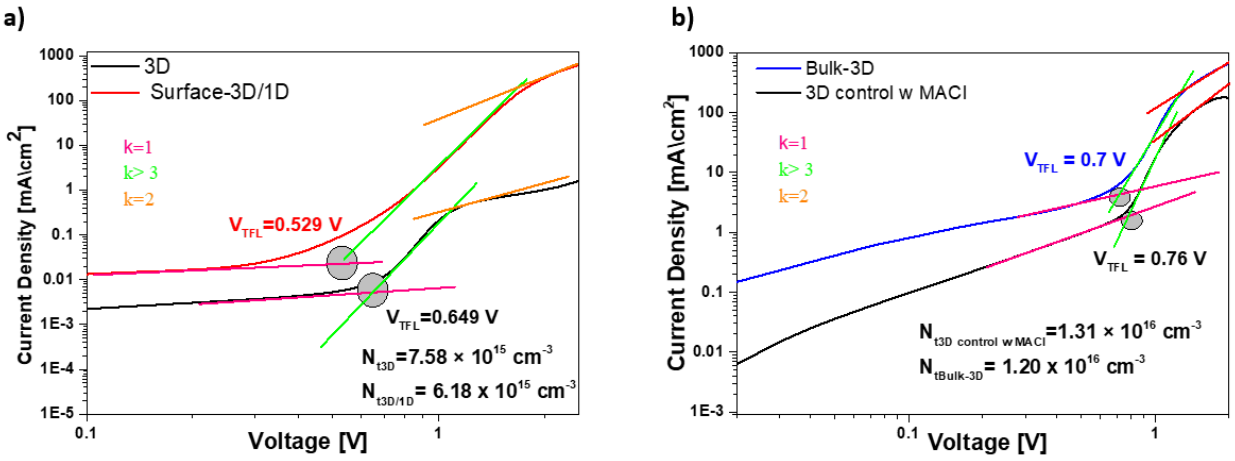

Figure S14. a-b) Electron only devices of the 3D MAPI control, surface-passivated 3D/1D, 3D MAPI control with MACl, and bulk-passivated 3D.

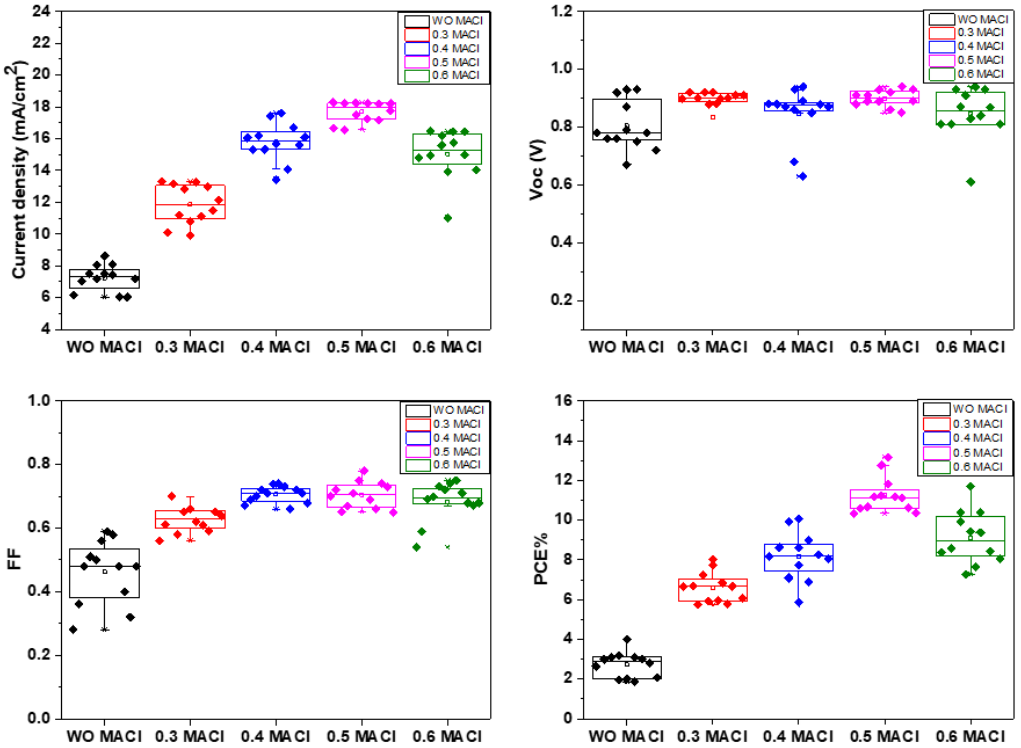

Figure S15. The statistical distribution of photovoltaic parameters of the bulk-3D MAPI with different ratios of MACl in the presence of ThPyI (for example 0.3 MACl means MACl/MAI: 0.3 wt. ratio).

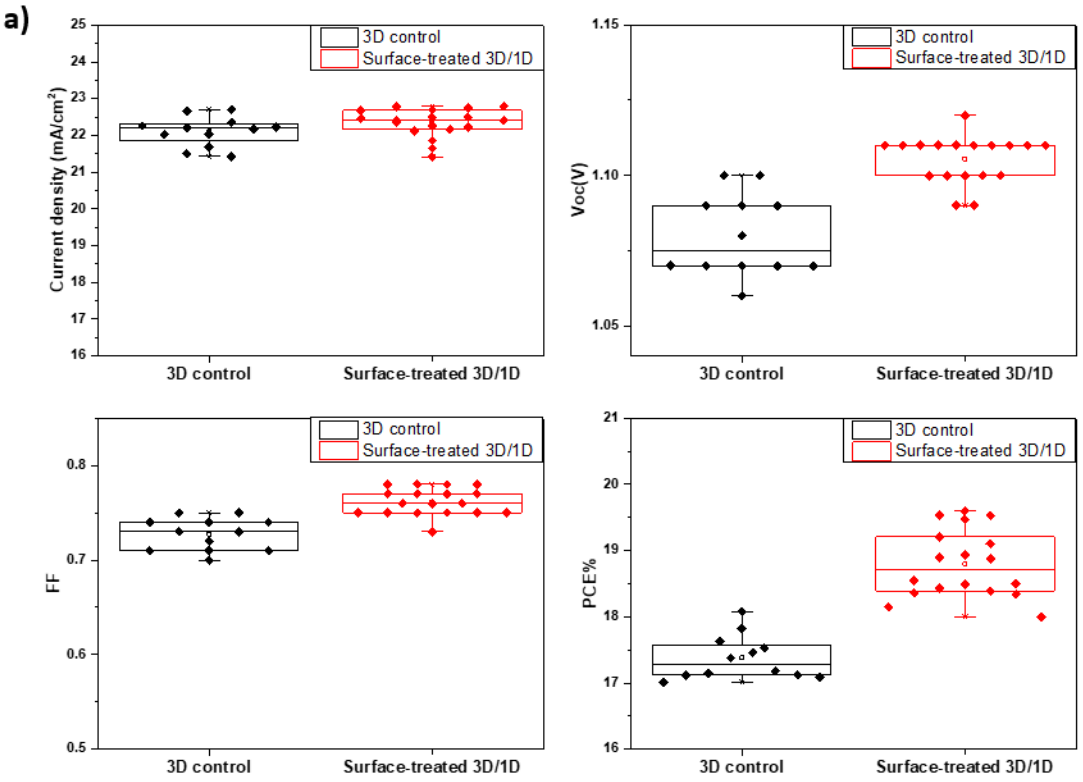

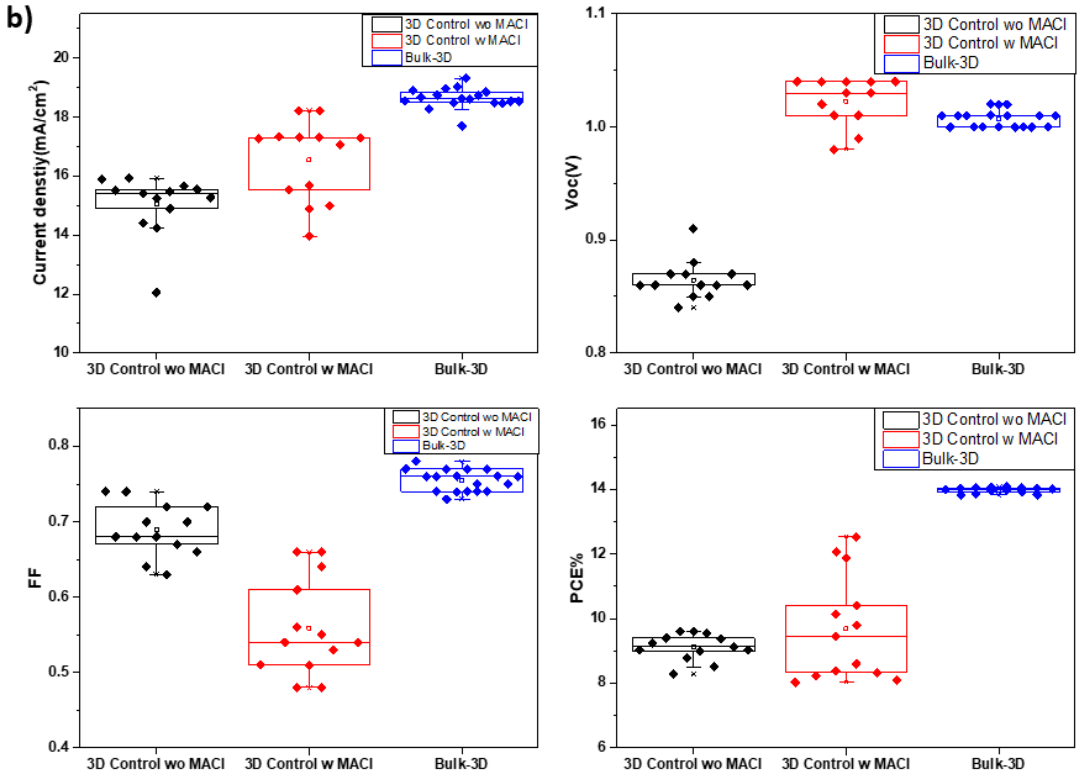

Figure S16. The statistical distribution of photovoltaic parameters of a) Surface-passivated and b) Bulk passivated devices.

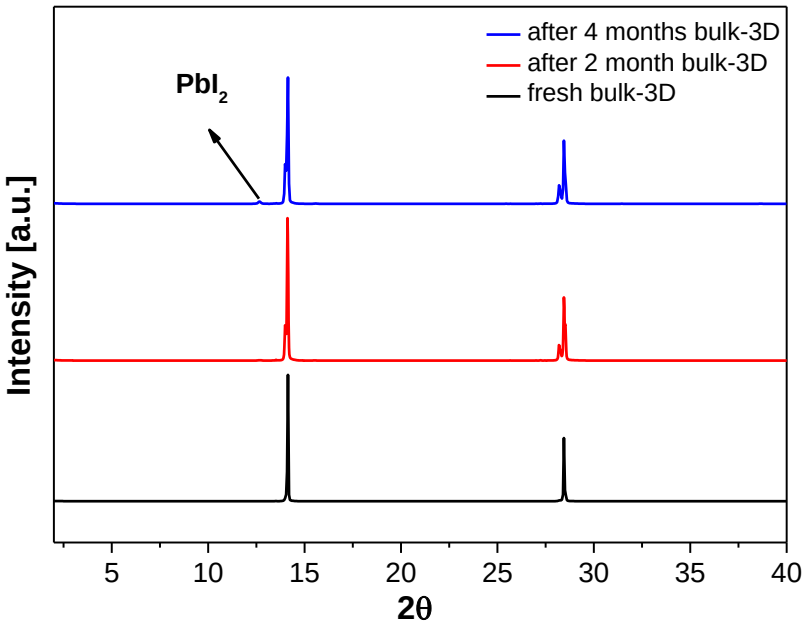

Figure S17. XRD patterns of bulk-passivated 3D perovskite thin films in air after 2 and 4 months.

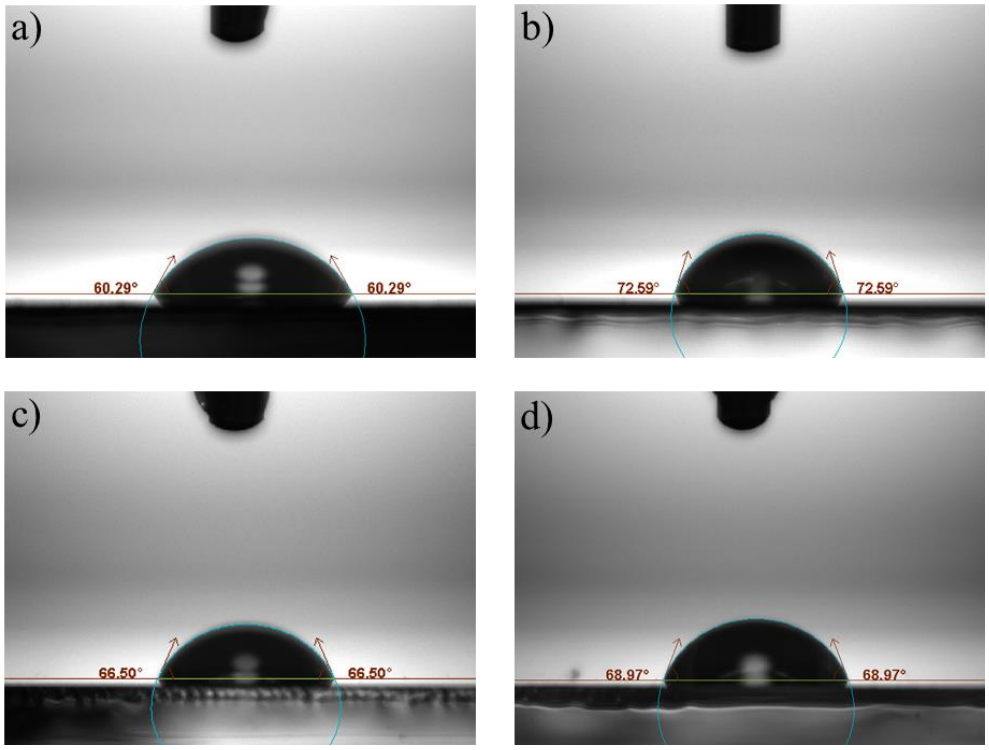

Figure S18. Contact angle measurements of a) 3D $MAPbI_3$ control, b) 1D perovskitoid, c) surface-passivated 3D/1D, and d) bulk-passivated 3D perovskite film.

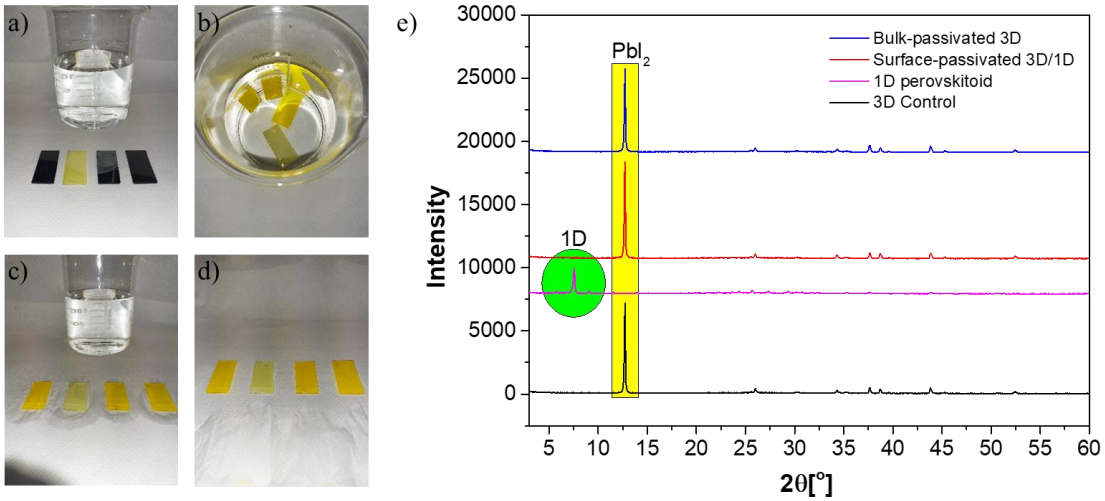

Figure S19. Photos of films, from left to right: a) 3D control, 1D, surface-passivated 3D/1D and bulk-passivated 3D, before water immersion, b) in water, c) after immersion (c), d) after drying, and e) XRD measurements.

Table S1. Crystallographic data of the 1D single crystal

net formula	$C_{18}H_{16}I_8N_2Pb_3S_2$
*M*r/g mol-1	1961.22
crystal size/mm	0.140 × 0.020 × 0.020
T/K	297.(2)
radiation	MoKα
diffractometer	'Bruker D8 Venture TXS'
crystal system	orthorhombic
space group	'F d d 2'
a/Å	25.389(3)
b/Å	61.606(6)
c/Å	4.5767(5)
α/°	90
β/°	90
γ/°	90
V/Å3	7158.5(13)
Z	8
calc. density/g cm-3	3.639
μ/mm-1	21.106
absorption correction	Multi-Scan
transmission factor range	0.33–0.68
refls. measured	24469
*R*int	0.0577
mean σ(*I*)/*I*	0.0488
θ range	3.094–28.281
observed refls.	3993
x, *y* (weighting scheme)	0.0099, 1443.4072
hydrogen refinement	constr
Flack parameter	0.126(18)
refls in refinement	4361
parameters	117
restraints	16

R(*F*obs)	0.0620
*R*w(*F*2)	0.1383
S	1.144
shift/errormax	0.001
max electron density/e Å-3	2.351
min electron density/e Å-3	-3.356

Table S2. Refined structural parameters of the 3D-Control sample.

Refinement was performed using Topas V4.2 SG- I4cm.[74]

Unit cell parameters

a (Å) 8.8706(15)

c (Å) 12.6404(23)

Site	Np	x	y	z	Atom	Occ	Beq
C1	4	0.50000	0.00000	0.61000	C	1	9.475
H1c1	16	0.41950	0.06230	0.58460	H	0.25	11.08
H1n1	16	0.46420	0.91500	0.75200	H	0.25	11.08
H2c1	16	0.59420	0.03860	0.58460	H	0.25	11.08
H2n1	16	0.59150	0.01150	0.75200	H	0.25	11.08
H3c1	16	0.48630	0.89910	0.58460	H	0.25	11.08
H3n1	16	0.44420	0.07350	0.75200	H	0.25	11.08
I1	4	0.00000	0.00000	0.1214(58)	I	1	9.8(3)
I2	8	0.72360(27)	0.22360(27)	0.3590(53)	I	1	6.57(1)
N1	4	0.50000	0.00000	0.72900	N	1	9.475
Pb1	4	0.00000	0.00000	0.3727(51)	Pb	1	3.41(8)

Table S3. a) Part of the Calculated Powder Diffraction Pattern for CuKa1 radiation of the ThPyI based 1D crystal structure data obtained from single crystal.

h	k	l	d (Å)	F(real)	F(imag)	|F|	2θ	I	M	ID(λ)	Phase
0	4	0	15.4015	331.564	59.7401	336.903	5.73363	2.23302	2	1	1
2	2	0	11.737	2072.66	303.527	2094.77	7.52601	100	4	1	1
2	4	0	9.79595	-751.68	-114.89	760.41	9.02013	9.15337	4	1	1
2	6	0	7.98325	-251.85	-77.194	263.416	11.0741	0.72611	4	1	1
0	8	0	7.70074	-767.67	-66.537	770.553	11.4817	2.88768	2	1	1
2	8	0	6.58405	209.808	42.3422	214.038	13.4373	0.32396	4	1	1
4	0	0	6.34735	954.273	47.4506	955.452	13.9409	2.99516	2	1	1
4	2	0	6.21674	-399.51	-9.8048	399.634	14.2353	1.00437	4	1	1
4	4	0	5.86851	478.925	61.4956	482.857	15.0847	1.30293	4	1	1
2	10	0	5.54243	242.154	47.2985	246.73	15.9779	0.3025	4	1	1

Table S4. The interplanar lattice distances of some planes.

h	k	l	d (Å)
2	2	0	11.74
0	8	0	7.7
2	3	1	2.87

Table S5. Time-resolved photoluminescence decay components of MAPI reference, surface, and bulk-treated MAPI films.

Sample	A_1(%)	τ_1 (μs)	A_2 (%)	τ_2 (μs)	$\tau_{ave.}$ (μs)
3D MAPI Control	58.19	0.050	41.81	0.114	0.076
Surface passivated 3D/1D	38.14	0.068	61.86	0.214	0.158
Bulk-passivated 3D	36.06	0.055	63.94	0.154	0.118
3D control with MACl	50.12	0.049	49.88	0.087	0.068

Table S6. Photovoltaic Parameters for the champion devices (reverse scan values are reported in parentheses)

Device	Jsc (mA\cm^2)	PCE %	Voc (V)	FF	Integrated Photocurrent (mA\cm^2)	Hysteresis Index %
3D Control	22.35(22.17)	18.08(17.01)	1.09(1.07)	0.74(0.72)	21.305 (Jsc -4,7%)	5.92
3D/1D Surface	22.69(22.79)	19.60(19.53)	1.11(1.10)	0.78(0.78)	21.692 (Jsc -4,4%)	0.35
3D control with MACl	17.81(16.54)	12.53(9.68)	1.03(1.02)	0.66(0.55)	16.09 (Jsc-9.6%)	16.9
Bul- 3D MAPI	18.98(18.94)	13(14.10)	1.02(1.01)	0.72(0.74)	18.00 (Jsc-5.11 %)	2.55

3.5 References

[1] Q. Jiang, Y. Zhao, X. Zhang, X. Yang, Y. Chen, Z. Chu, Q. Ye, X. Li, Z. Yin, J. You, *Nat. Photonics* **2019**, *13*, 460.

[2] N. Torabi, A. Behjat, Y. Zhou, P. Docampo, R. J. Stoddard, H. Hillhouse, T. Ameri, *Mater. Today Energy*, **2019**, *12*, 70

[3] W. Zhang, G. E. Eperon, H. J. Snaith, *Nat. Energy* **2016**, *1*, 1.

[4] G. Xing, N. Mathews, S. Sun, S. S. Lim, Y. M. Lam, M. Graẗzel, S. Mhaisalkar, T. C. Sum, *Science* **2013**, *342*, 344.

[5] H. S. Kim, C. R. Lee, J. H. Im, K. B. Lee, T. Moehl, A. Marchioro, S. J. Moon, R. Humphry-Baker, J. H. Yum, J. E. Moser, M. Grätzel, N. G. Park, *Sci. Rep.* **2012**, *2*, 1.

[6] N. G. Park, M. Grätzel, T. Miyasaka, K. Zhu, K. Emery, *Nat. Energy* **2016**, *1*, 1.

[7] X. Li, D. Bi, C. Yi, J. D. Décoppet, J. Luo, S. M. Zakeeruddin, A. Hagfeldt, M. Grätzel, *Science* **2016**, *353*, 58.

[8] S. de Wolf, J. Holovsky, S. J. Moon, P. Löper, B. Niesen, M. Ledinsky, F. J. Haug, J. H. Yum, C. Ballif, *J.Phys. Chem. Lett.* **2014**, *5*, 1035.

[9] C. C. Stoumpos, C.D. Malliakas, M.G. Kanatzidis, *Inorg. Chem*. **2013**,*52*, 9019.

[10] X. Li, M.I. Dar, C. Yi, J. Luo, M. Tschumi, S. M. Zakeeruddin, M. K. Nazeeruddin, H. Han, M. Grätzel, *Nat. Chem.* **2015**, *7*, 703.

[11] E. Khorshidi, B. Rezaei, D. Blätte, A. Buyruk, M. A. Reus, J. Hanisch, B. Böller, P. Müller-Buschbaum, T. Ameri, *Sol. RRL*, **2022**, *6*, 2200023.

[12] E. Khorshidi, B. Rezaei, J. Hanisch, B. Böller, M. A. Reus, P. Müller-Buschbaumde, T. Ameri, *ACS Appl. Mater. Interfaces,* **2022,** *14*, 54623.

[13] L. Wang, H. Zhou, J. Hu, B. Huang, M. Sun, B. Dong, G. Zheng, Y. Huang, Y. Chen, L. Li, Z. Xu, N. Li, Z. Liu, Q. Chen, L. D. Sun, C. H. Yan, *Science* **2019**, *363*, 265.

[14] C. Ortiz-Cervantes, P. Carmona-Monroy, D. Solis-Ibarra, *ChemSusChem*, **2019**,*12*, 1560.

[15] C. Li, S. Tscheuschner, F. Paulus, P. E. Hopkinson, J. Kießling, A. Köhler, Y. Vaynzof, S. Huettner, *Adv. Mater*. **2016**, *28*, 2446.

[16] C. Eames, J. M. Frost, P. R. F. Barnes, B. C. O'regan, A. Walsch, M. F. Islam, *Nat. Commun.*, **2015**, *6*, 7497.

[17] M. I. Saidaminov, J. Kim, A. Jain, R. Quintero-Bermudez, H. Tan, G. Long, F. Tan, A. Johnston, Y. Zhao, O. Voznyy, E. H. Sargent, *Nat. Energy*, **2018**, *3*, 648.

[18] A. S. R. Bati, M. Batmunkh, J. G. Shapter, *Adv. Energy Mater.* **2020**, *10*, 1902253.

[19] H. Zhang, Y. Wu, C. Shen, Er. Li, C. Y, W. Zhang, H. Tian, L. Han, W. Zhu, *Adv. Energy Mater.* **2019**, *9*, 1803573.

[20] E. H. Jung, N. J. Jeon, E. Y. Park, C. S. Moon, T. J. Shin, T. Y. Yang, J.H. Noh, J. Seo, *Nature* **2019**, *567*, 511.

[21] E. Aydin, M. de Bastiani, S. de Wolf, *Adv. Mater.* **2019**, *31*, 1900428.

[22] F. Gao, Y. Zhao, X. Zhang, J. You, *Adv.Energy Mater.* **2020**, *10*, 1902650.

[23] Y. Huang, H. Luo, B. Zhang, K. Su, W. Chen, G. Sui, L. Liang, B. Zhang, J. Song, P. Gao, *Appl. Mater.Today*. **2022**,*28*, 101550.

[24] A. Krishna, S. Gottis, M. K. Nazeeruddin, F. Sauvage, *Adv. Funct. Mater.* **2019**, *29*, 1806482.

[25] L. Mao, C. C. Stoumpos, M. G. Kanatzidis, *J. Am. Chem. Soc.* **2018**, *141*, 1171.

[26] H. Tsai, W. Nie, J. C. Blancon, C. C. Stoumpos, R. Asadpour, B. Harutyunyan, A. J. Neukirch, R. Verduzco, J. J. Crochet, S. Tretiak, L. Pedesseau, J. Even, M. A. Alam, G. Gupta, J. Lou, P. M. Ajayan, M. J. Bedzyk, M. G. Kanatzidis, A. D. Mohite, *Nature* **2016**, *536*, 312.

[27] J. Qian, Q. Guo, L. Liu, B. Xu, W. Tian, *J. Mater. Chem. A* **2017**, *5*, 16786.

[28] W. Fu, J. Wang, L. Zuo, K. Gao, F. Liu, D. S. Ginger, A. K. Y. Jen, *ACS Energy Lett.* **2018**, *3*, 2086.

[29] Y. Chen, Y. Sun, J. Peng, J. Tang, K. Zheng, Z. Liang, *Adv. Mater.* **2018**, *30*, 170348.

[30] J. Fan, Y. Ma, C. Zhang, C. Liu, W. Li, R. E. Schropp, Y. Mai, *Adv. Energy Mater.* **2018,** *8*, 1703421.

[31] P. Chen, Y. Bai, S. Wang, M. Lyu, J. Yun, L. Wang, *Adv. Funct. Mater.* **2018**, *28*, 1706923.

[32] C. C. Stoumpos, L. Mao, C. D. Malliakas, M. G. Kanatzidis, *Inorg. Chem.* **2017**, *56*, 56.

[33] D. Bi, P. Gao, R. Scopelliti, E. Oveisi, J. Luo, M. Grätzel, A. Hagfeldt, M. K. Nazeeruddin, *Adv. Mater.* **2016**, *28*, 2910.

[34] N. Yang, C. Zhu, Y. Chen, H. Zai, C. Wang, X. Wang, H. Wang, S. Ma, Z. Gao, X. Wang, J. Hong, Y. Bai, H. Zhou, B.B. Cui, Q. Chen, *Energy Environ. Sci.* **2020**, *13*, 4344.

[35] H. Lin, C. Zhou, Y. Tian, T. Siegrist, B. Ma, *ACS Energy Lett.* **2018**, *3*, 54.

[36] C. Zhou, Y. Tian, M.Wang, A. Rose, T.Besara, N. K. Doyle, Z. Yuan, J. C. Wang, R. Clark, Y. Hu, T. Siegrist, S. Lin, B. Ma, *Angew. Chem., Int. Ed.* **2017**, *56*, 9018.

[37] T. Kong, H. Xie, Y. Zhang, J. Song , Y. Li, L. Lim, A. Hagfeld, D. Bi, *Adv.Energy Mater.*

2021, *11*, 2101018.

[38] J. Im, C. C. Stoumpos, H. Jin, A. J. Freeman, M. G. Kanatzidis, *J. Phys. Chem. Lett.* **2015**, *6*, 3503.

[39] L. Gao, I. Spanopoulos, W. Ke, S. Huang, I. Hadar, L. Chen, X. Li, G. Yang, M.G. Kanatzidis, *ACS Energy Lett.* **2019,** *4*, 1763.

[40] P. Liu, Y. Xian, W. Yuan, Y. Long, K. Liu, N. U. Rahman, W. Li, J. Fan, *Adv. Energy Mater.* **2020**, *10*, 1903654.

[41] M. Pratheek, T. Abhinav, S. Bhattacharya, G. K. Chandra, P. Predeep, *Mater Sci.Technol.* **2021**, *4*, 282.

[42] S. Gharibzadeh, P. Fassl, I. M. Hossain, P. Rohrbeck, M. Frericks, M. Schmidt, T. Duong, M. R. Khan, T. Abzieher, B. A .Nejand, F. Schackmar, O. Almora, T. Feeney, R. Singh, D. Fuchs, U. Lemmer, J. P. Hofmann, S. A. L. Weber, U. W. Paetzold, *Energy Environ.Sci*. **2021**, *14*, 5875.

[43] G. Kim, H. Min, K. S. Lee, D. Y. Lee, S. M. Yoon, S.I. Seok, *Science* **2020**, *370*, 108.

[44] M. Jeong, I. W. Choi, E. M. Go, Y. Cho, M. Kim, B. Lee, S. Jeong, Y. Jo, H. W. Choi, J. Lee, J. H. Bae, S. K. Kwak, D. S. Kim, C. Yang, *Science* **2020**, *369*, 1615.

[45] C. Zhang, S. Wu, L. Tao, G. M. Arumugam, C. Liu, Z. Wang, S. Zhu, Y. Yang, J. Lin, X. Liu, R. E. I. Schropp, Y. Mai, *Adv. Energy Mater.* **2020**, *10*, 2002004.

[46] Z. Liu, F. Cao, M. Wang, M. Wang, L. Li, *Angew. Chem., Int. Ed.* **2020**, *59*, 4161.

[47] C. Ma, N. G. Park, *ACS Energy Lett.* **2020**, *5*, 3268.

[48] F. Li, X. Deng, F. Qi, Z. Li, D. Liu, D. Shen, M. Qin, S. Wu, F. Lin, S. H. Jang, J. Zhang, X. Lu, D. Lei, C. S. Lee, Z. Zhu, A. K. Y. Jen, *J. Am. Chem. Soc.* **2020**, *142*, 20134.

[49] L. Liu, S. Huang, Y. Lu, P. Liu, Y. Zhao, C. Shi, S. Zhang, J. Wu, H. Zhong, M. Sui, H. Zhou, H. Jin, Y. Li, Q. Chen, *Adv. Mater.* **2018**, *30*, 1800544.

[50] J. Peng, D. Walter, Y. Ren, M. Tebyetekerwa, Y. Wu, T. Duong, Q. Lin, J. Li, T. Lu, M. A. Mahmud, O. L. C. Lem, S. Zhao, W. Liu, Y. Liu, H. Shen, L. Li, F. Kremer, H. T. Nguyen, D. Y. Choi, K. J. Weber, K. R. Catchpole, T. P. White, *Science* **2021**, *371*, 390.

[51] X. Lin, D. Cui, X. Luo, C. Zhang, Q. Han, Y. Wang, L. Han, *Energy Environ. Sci.* **2020**, *13*, 3823.

[52] Y. Kuang, K. H. M. van der Werf, Z. S. Houweling, R. E. I. Schropp, *Appl. Phys. Lett.* **2011**, *98*, 113111.

[53] B. M. Kayes, H. A. Atwater, N. S. Lewis, *J. Appl. Phys.* **2005**, *97*, 114302.

[54] T. M. Koh, V. Shanmugam, J. Schlipf, L. Oesinghaus, P. Müller-Buschbaum, N.

Ramakrishnan, V. Swamy, N. Mathews, P. P. Boix, S. G. Mhaisalkar, *Adv. Mater.* **2016**, *28*, 3653.

[55] C. Fei, L. Guo, B. Li, R. Zhang, H. Fu, J. Tian, G. Cao, *Nano Energy*. **2016** *27*, 17.

[56] A. Buyruk, D. Blätte, M. Günther, M. A. Scheel, N. F. Hartmann, M. Döblinger, A. Weis, A. Hartschuh, P. Müller-Buschbaum, T. Bein, T. Ameri, *ACS Appl. Mater. Interfaces* **2021**, *13*, 32894.

[57] H. Gökce, S. Bahceli , *Spectrochim. Acta A Mol. Biomol. Spectrosc.* **2012,** *96*, 139.

[58] R. Szostak, J. C. Silva, S. H. Turren-Cruz, M. M. Soares, R. O. Freitas, A. Hagfeldt, H. C. N. Tolentino, A. F. Nogueira, *Sci. Adv.* **2019**, *5*, eaaw6619.

[59] M. A. Pérez-Osorio, Q. Lin, R. T. Phillips, R. L. Milot, L. M. Herz, M. B. Johnston, F. Giustino, *J. Phys. Chem. C* **2018** *122*, 21703.

[60] H. Gökce, S. Bahceli, *J. Mol. Struct.* **2011**, *1005*, 100.

[61] W. S. Yang, B. W. Park, E. H. Jung, N. J. Jeon, Y. C. Kim, D. U. Lee, S. S. Shin, J. Seo, E. K. Kim, J. H. Noh, S. il Seok, *Science* **2017**, *356*, 1376.

[62] M. H. Li, H. H. Yeh, Y. H. Chiang, U. S. Jeng, C. J. Su, H. W. Shiu, Y. J. Hsu, N. Kosugi, T. Ohigashi, Y. A. Chen, P. S. Shen, P. Chen, T. F. Guo, *Adv- Mater.* **2018**, *30*, 1801401.

[63] D. H. Cao, C. C. Stoumpos, O. K. Farha, J. T. Hupp, M. G. Kanatzidis, *J. Am. Chem. Soc.* **2015**, *137*, 7843.

[64] M. Yavari, F. Ebadi,S. Meloni , Z. S. Wang , T. C. J. Yang, S. Sun, H. Schwartz, Z. Wang, B. Niesen , J. Durantini, P. Rieder, K. Tvingstedt, T. Buonassisi, W. C. H. Choy, A. Filippetti, T. Dittrich, S. Olthof, J. P.

[65] W. Wang, M. Cai, Y. Wu, K. Ji, B. Cheng, X. Liu, H. Lv, S. Dai, *Symmetry* **2022**, *14*, 1099.

[66] T. J. Jacobsson, J. P. Correa-Baena, E. Halvani Anaraki, B. Philippe, S. D. Stranks, M. E. F. Bouduban, W. Tress, K. Schenk, J. Teuscher, J. E. Moser, H. Rensmo, A. Hagfeldt, *J. Am. Chem. Soc.* **2016**, *138*, 10331.

[67] B. Wu, H. T. Nguyen, Z. Ku, G. Han, D. Giovanni, N. Mathews, H. J. Fan, T. C. Sum, *Adv. Energy Mater.* **2016**, *6*, 1600551.

[68] P. Chen, Y. Bai, S. Wang, M. Lyu, J. H. Yun, L. Wang, *Adv. Funct. Mater*. **2018**, *28*, 1706923.

[69] R. H. Bube, *J.Appl. Phys.* **2004**, *33*, 173.

[70] APEX, Bruker, and Bruker AXS SAINT. Inc.: Madison, Wisconsin, USA, **2012**

[71] G. M. Sheldrick, *SADABS, Empirical Absorption Correction Program*, University of

Göttingen, Germany,**1997**.

[72] Sheldrick, G. M. *Acta Cryst.*, **2015**. *A71*, 3.

[73] Farrugia, L. J. J. *Appl. Cryst*., **2012**. *45*, 849.

[74] TOPAS V4.2, General Profile and Structure Analysis Software for Powder Diffraction Data. In Tutorial; Bruker AXS: Karlsruhe, Germany, 2009.

4. The Role of Fluorine-Functionalized Organic Spacers for Defect Passivation and Low-Dimensional Phase Formation in 3D MAPI Perovskite Solar Cells

This chapter is based on the following manuscript in preparation:

Ali Semerci, Javier Urieta-Mora, Sander Driessen, Ali Buyruk, Rik Hooijer, Agustín Molina-Ontoria, Bülent Alkan, Seckin Akin, Mattia Fanetti, Harishankar Balakrishnan, Achim Hartschuh, Shuxia Tao, Nazario Martin, Peter Müller-Buschbaum, Saim Emin, Tayebeh Ameri

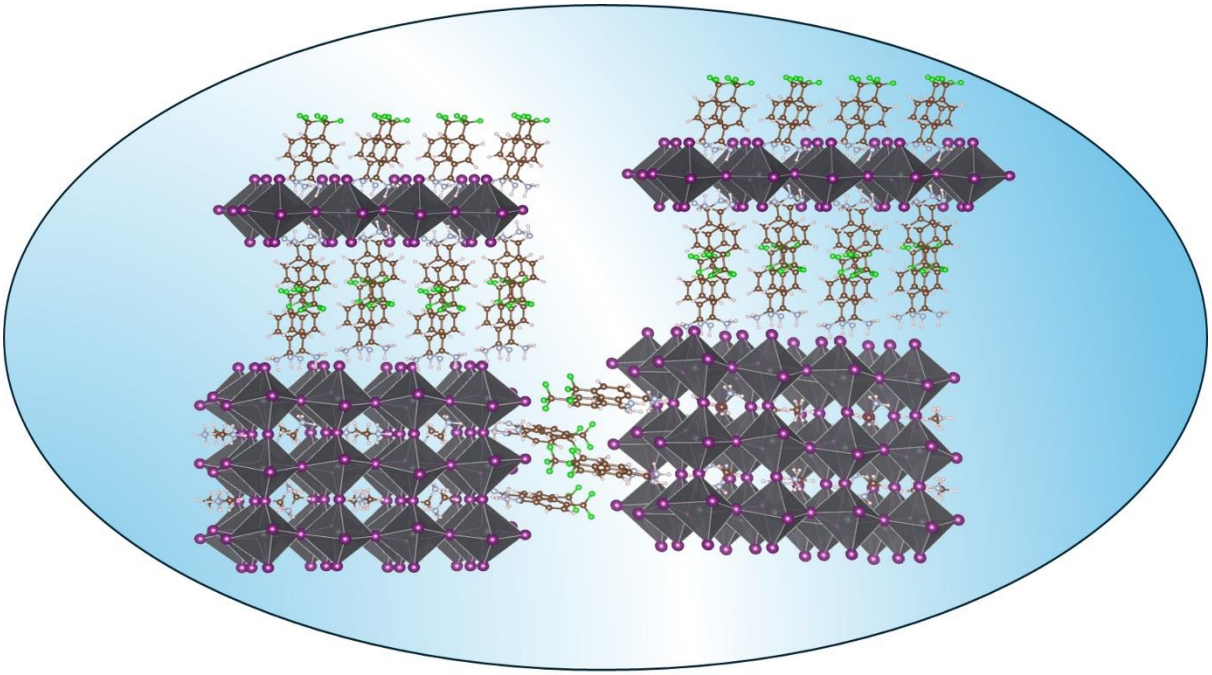

Keywords

Perovskite solar cell, passivation, mixed-dimensional perovskite, fluorinated organic spacers

4.1 Introduction

In recent years, organic-inorganic 3D halide perovskites (OIHP) have gained prominence as a top contender in advanced thin film photovoltaic (PV) technology, demonstrating significant advancements.[1-3] The power conversion efficiency (PCE) of 3D OIHP has risen considerably, increasing from 3.8% to 25.73% (certified).[4-5] OIHP is a potential material for low-cost PV due to its unique features, which include a high absorption coefficient, low binding energy, long charge carrier diffusion length, high carrier mobility, and adjustable bandgap.[6-10] The industrial use of 3D perovskite solar cells (PSCs) continues to be hampered by their poor intrinsic stability against moisture and temperature under ambient operating conditions, despite the significant progress that has been made in PCE.[10-14]

The film quality of perovskite material is an important factor in the high performance and stability of PSCs. When perovskite films are produced using the conventional solution technique, there is a high probability that defects will occur at the surfaces and grain boundaries (GBs).[15-16] It is common knowledge that the defect sites that are present at either the surface or the GBs are the typical starting point for the degradation of perovskite. Therefore, the presence of GBs makes it easier for moisture and oxygen from the surrounding environment to penetrate into perovskite films, which in turn speeds up the process of perovskite decomposition.[17-19] Previous studies have shown that the instability of PSCs is mainly caused by trapped charges. Organic cations such as $CH_3NH_3^+$ (MA^+) or $NH_2CH{=}NH_2^+$ (FA^+) have limited freedom for ion migration at higher temperatures, thus contributing to the instability of 3D perovskite frameworks. The defects result in decreased efficiency by affecting charge carrier dynamics due to an imbalanced distribution of charges and the unstable nature of the PSCs.[20-24] Defects arise when perovskite sheet crystallizes in-situ, leading to non-radiative recombination losses in device operations. Common point defects with low formation energies in MAPI thin films include uncoordinated Pb^{2+}, uncoordinated halide ions, Pb clusters, and Pb-I antisite defects. Hence, it is essential to eliminate imperfections in perovskite films to enhance stability without compromising the efficiency of PSCs.[25-31]

Low-dimensional PSCs have drawn increasing interest over the past couple of years.[32] A commonly employed approach to reduce non-radiative recombination in 3D MAPI perovskites is to either treat surface defects with properly functionalized molecules or introduce low-dimensional perovskites (1D or 2D).[33-36] A wide range of substances, including Lewis bases, and acids, metal cations, metal anions, and alkylammonium halogenides, have been employed

as passivation agents to mitigate the structural defects in perovskites.[37] Moreover, when introduced into 3D perovskite frameworks, LDPs act as passivating agents, minimizing the influence of defects. Additionally, the LDPs act as heterojunctions, enhancing the fluorescence lifetimes inside the perovskite framework.[38] In comparison to their 3D counterparts, the presence of large organic spacer cations greatly increases the moisture resistance of LDP structures. However, the LDP PSCs typically exhibit a comparatively diminished PCE due to the limited charge transport capabilities, high exciton binding energies, and wider band gap, acting as insulators.[39-40]

Mixed-dimensional perovskites (3D/LDP) are considered a promising strategy for PSCs. Thus, the advantages of two different perovskite derivatives are combined. The 3D perovskite controls optical absorption and charge transport qualities, while a thin hydrophobic LDP seals defects on the surface and protects the 3D perovskite from moisture. The LDP also aligns the energy bands and regulates the film quality of the 3D perovskite structure.[41-42] For example, advancements in 3D/LDP PSCs have mostly focused on modifying the optoelectronic characteristics of 2D Ruddlesden-Popper phases by altering the organic spacers.[43] LDP often exhibit a significantly higher exciton binding energy due to their robust quantum and dielectric confinement.[44] To decrease the dielectric confinement leading to low charge transfer in perovskite devices, an effective strategy is to create organic spacers with a high dielectric constant through enhancing molecular dipole moments. Functional groups with high electronegativity are utilized to create an appropriate organic spacer for this purpose. Fluorine (F) as the most electronegative element is often used as a functional unit to design organic spacers to raise the dipole moment and dielectric constant.[45-48] Wie et al. were among the pioneers who introduced F atoms into lead-based PSCs.[49] Following that, organic spacers 4-Trifluoromethyl-phenethylammonium (CF_3-PEA), 4-(trifluoromethyl)benzylammonium iodide (TFMBAI), 4-(trifluoromethyl) benzylamine (4TFBZA), 3-fluoro-benzyl ammonium iodide (3FBAI), and 2-[4-phenyl]ethanamine were utilized in 2D and 3D/2D PSCs.[50-55] The fluorinated substances are reported to improve device performance. In general, organic spacers that incorporate amine ($-NH_2$) functional groups are extensively employed to supplement the 3D perovskite film with an LDP protective layer.[56] Conversely, when compared to the amine groups, the formamidinium (FA) functional group interacts more strongly with Pb-I octahedrons and demonstrates superior charge transport capability.[57-58] To fabricate an LDP perovskite structure, organic spacers containing FA group (e.g., benzamidine (PhFA), 2-

thiopheneformamidinium (ThFA), and para-fluorobenzamidine (p-FPhFA)) have been the subject of very few investigations.[59-60] Given this knowledge, it is clear that a systematic study is required for building organic spacers to obtain insight into the mix-dimensional perovskite formation, which influences the passivation mechanism and efficiency of PSCs.

In this study, 3,5-difluorobenzene-1-carboximidamidium iodide, 4-(trifluoromethyl)benzene-1-carboximidamidium iodide, and 2,3,4,5,6-pentafluorobenzene-1-carboximidamidium iodide from the same family containing F atoms and FA functional groups, referred to as 2F, 3F, and 5F, were utilized to create an LDP on 3D MAPI PSCs. The acronyms 2F, 3F, and 5F represent the number of F atoms contained in the molecules. The study examined how the dipole moment of organic spacers affects the performance of PSCs by the passivation of trap states. Cathodoluminescence (CL) investigations, a powerful technique, also reveal certain aspects of LDP generation on perovskite surfaces. High-resolution transmission electron microscopy (HR-TEM) observations provided additional evidence for the existence of LDP, as seen by the significant lattice spacings obtained. To gain more insight into the effect of these fluorinated spacers, we conduct DFT calculations to examine the interactions between the passivation species and the 3D MAPI surface. The stability investigation involves calculating the binding energy (E_b) of fluorinated organic molecules on the Pb-I terminated perovskite surfaces. The DFT calculations show that the bonding strength between fluorinated molecules and MAPI surfaces is significantly increased. The strongest binding is found for the 3F spacer, due to its largest dipole moment. This enhancement plays a major role in the passivation of the perovskite surface.

4.2 Results and Discussion

Figure 1a–c depicts the molecular structure of the organic spacers 2F, 3F, and 5F utilized in this study. Nuclear magnetic resonance (^{1}H-, ^{19}F-NMR) and mass spectroscopy were used to characterize the compounds (**Figure S1-S4**, Supporting Information). All three organic spacers possess FA and F as functional groups, which are either directly or indirectly connected to a benzene ring. Previous studies have shown that fluorinated organic spacer cations with high polarity can increase the dielectric constant.[61] This results in a reduction of the coulomb force between the exciton's electron and hole pair, thereby promoting effective charge separation. Research indicates that the use of fluorinated spacers enhances several characteristics of low-dimensional perovskites, mostly due to their tunable dipole moments.[62]

Dipole moments of organic spacers were calculated to comprehend how the number of F atoms

and their position in the aromatic ring affect the dipole moment as illustrated in **Figure 1d-e**. The respective dipole moments of molecules 2F, 5F, and 3F are calculated in DFT calculations, and values of 3.55, 3.76, and 4.56 D, were obtained, respectively. The differences in dipole moments have a significant impact on the quality of the modified perovskite films and the performance of the devices.

The 3D/LDP PSCs device was fabricated by spin-coating organic spacers to form an LDP perovskite structure on 3D MAPI films. Scanning electron microscopy (SEM) studies were conducted to assess the morphology of 3D control with 5% of excess lead iodide (PbI_2), 2F, 3F, and 5F-3D/LDP MAPI perovskite films. The top-view SEM images in **Figures 2a–d** demonstrate that the active MAPI layers fully coat the substrate surface. Additionally, there is excess PbI_2 along grain boundaries, which appear in the form of small particles (yellow circles) in the 3D control (**Figure 2a**).

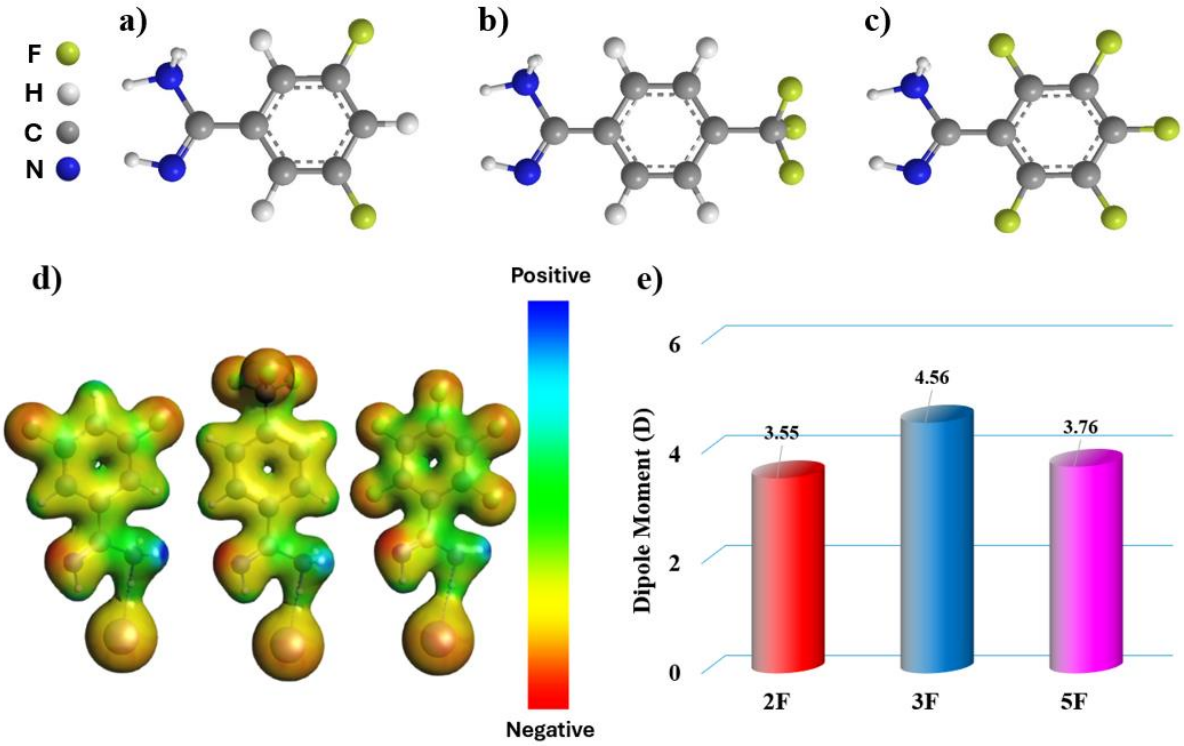

Figure 1. a-c) Molecular structure of 2F, 3F, 5F organic spacer, respectively. **d)** Electrostatic potential (ESP) analysis of the xF-organic spacers (x=2, 3, 5). The color bar indicates the self-consistent field coulomb potential (SCF-Coulpot): negative (red) and positive (blue); **e)** Calculated molecular dipole moments of 2F, 3F and 5F molecules.

The crystal grains of the 3D control with clear boundaries vary from several hundred nanometers to a micron range size as depicted in **Figure 2a**. On the other side, the modified

perovskite films display less obvious grain boundaries, as shown in **Figure 2b-d**, suggesting the occurrence of surface passivation.[52] The size of the grains remains similar when compared to the 3D control film. A small-size conglomeration was found on the surface of 2F-treated films as presented in **Figure 2b**. Upon analyzing the perovskite phase treated with 3F, one can observe larger and more clearly defined conglomerated formations along the grain boundaries as shown in **Figure 2c.** It demonstrates that 5F follows a similar pattern in **Figure 2d**. Moreover, the excess PbI_2 situated at the interfaces of the perovskite grains undergoes partial consumption when treated with 2F, while experiencing a more substantial consumption in the case of perovskite treated with 3F and 5F (as shown below in CL part). The FA^+ functional group of these spacers is expected to react with uncoordinated surface Pb atoms.[58] The conglomerations can influence the charge transfer across the grains due to changes in the interfacial dipole caused by this interaction.[63] SEM analysis was also performed on perovskite film surfaces treated with various concentrations of corresponding organic spacers (**Figure S5a-c**, Supporting Information). SEM images captured with a backscattered electron detector (BED) unveil the presence of distinct phases exhibiting different contrast (**Figure S6a-d**, Supporting Information). Structures with a brighter color are smaller in size compared to the MAPI grains, primarily appearing between the grains as nanoparticles with irregular shapes. The brighter structures observed at the grain boundaries in the 3D control sample, which includes excess PbI_2 (5%), are attributable to PbI_2. In the treated samples, the alterations in shape, size, and distribution density of these agglomerates indicate that they are not the same excess PbI_2 particles observed in the 3D control film (**Figure S6b-d,** Supporting Information). The hypothesis is that, in the sample exposed to 2F and 3F, the concentration of PbI_2 diminishes, allowing for the emergence of LDP. In contrast, the 5F passivated sample undergoes complete conversion of PbI_2, resulting in the formation of LDP on the surface of MAPI grains. Additionally, small spots are observed on the MAPI grains, especially in the 2F- and 3F-treated films. In the case of the 5F-treated sample, there are fewer tiny formations, and most of the agglomerates are situated between the MAPI grains. However, the analysis with backscattered electrons cannot unambiguously distinguish between PbI_2 and LDP phases.

CL has proven to be an effective tool for studying the recombination behavior of charge carriers in PV materials, with sub-micrometer spatial resolution. Moreover, for highly emitting materials (such as MAPI), CL can be useful in distinguishing different phases, when X-ray microanalysis or backscattered electron imaging encounter unfavorable conditions (e.g.

materials very sensitive to irradiations). Xiao et al. thoroughly investigated the effect of accelerating voltage and incident electron beam current on the emission parameters of MAPI perovskite films.[64] Their extensive research dives into the changes in emission intensity and spectrum caused by various e-beam excitation settings. A comparison of MAPI emission spectra at various accelerating voltage and beam current settings revealed unique influences on emission properties with time and found that irradiation with low beam energy (such as 2 KeV) at low beam current (<4 nA) are suitable to detect a clear signal without degradation of the sample. We analyzed the surface of specimens with 2 KeV beam energy and ~0.06 nA beam current. In these conditions, the sample was not visibly degrading, and the CL signal was high enough for analysis. The CL intensity measurement of solution-cast MAPI films developed on ITO-coated glass slides with a SnO_2 layer (about 40 nm) on top of the ITO is shown in **Figure 2e**. The most intense emission is localized at the PbI_2 grains (two of them indicated with yellow circles in Figure **2e**). We observed that the intensity of the different features is subject to a time-dependent process (**Figure S7**, Supporting Information). At the beginning (i.e. after minimum exposition to e-beam) the most intense emission come from the MAPI grains (**Figure S7b,** Supporting Information), and in many cases there is an intensity difference between the grains (see also **Figure 2f**). This indicates that different grains have varied nonradiative recombination rates near the film surface. We hypothesize that the intensity variation can be attributed to different concentrations of surface defects among distinct grains. Longer exposure results in a decrease in perovskite CL intensity , whereas the PbI_2 grains preserve a pronounced CL emission (**Figure S7c-e**, Supporting Information). In treated perovskite films, there are also darker spots exhibiting much lower (or none) emission as shown in **Figure 2f-h** (some of them indicated by circles). The appearance of darker spots in the treated films support the disappearance of PbI_2 and validate the formation of a new phase that could be assigned to LDP. In the SEM image captured with a SED detector (**Figure 2a-d**), these formations appear white. The average size of these structures in the 2F-treated perovskite is less than 100 nm, while the LDP agglomerates in the 3F and 5F typically range between 100 and 300 nm.

Utilizing an atomic force microscope (AFM), the passivated perovskite films were further investigated for changes in their surface roughness. The root mean square (RMS) roughness of the 3D control film is determined to be 10.7 nm. On the other hand, after the treatment the 2F, 3F, and 5F perovskite thin films show RMS values of 7.6 nm, 7.2 nm, and 7.7 nm, respectively (**Figure S8,** Supporting Information). The lower RMS values are favorable for the deposition

of hole transport material (HTM). In addition, the decreased surface roughness of the mixed 3D/LDP film can be accepted to have a positive impact on charge carrier transport resulting in an enhanced performance of derived PSCs.

X-ray diffraction (XRD) was used to analyze the crystallinity of 3D control, and 3D/LDP perovskite films as shown in **Figure 2i**. The primary XRD peaks of the 3D control are observed at 14.19º and 28.50º 2θ, corresponding to the (110) and (220) planes of MAPI, respectively.[36] The diffraction peak corresponding to excess PbI_2 was noted at 12.7°. This peak exhibited a decrease in the 2F, 3F, and 5F-treated perovskite films compared to the 3D control, suggesting the conversion of excess PbI_2 to LDP. So that, extra peaks are observed at low 2θ angles of 6.1, 5.4, and 8.2° in the XRD pattern of the 3D/LDP perovskite films treated with 2F, 3F, and 5F, respectively. It was determined that these new signals did not originate from the corresponding organic spacers, as evidenced by the comparison with the XRD analysis of pure organic spacers (**Figure S9**, Supporting Information). Therefore, the extra peaks are associated with the combined new phases on the 3D perovskite surface as illustrated in **Figure 2b-d**. The weak reflections at the low 2θ angle (<10°) suggest the presence of LDP formed during annealing, as reported in prior research.[52, 65]

X-ray photoelectron spectroscopy (XPS) investigation was conducted to study the surface composition of the treated perovskite films. The passivated samples were found to have the F element from the corresponding organic spacers. The distinct photoemission peak of F atom in core level F1s was detected in the treated perovskite films (**Figure S10** Supporting Information). The binding energies of the Pb $4f_{5/2}$ and Pb $4f_{7/2}$ orbitals in the 3D control perovskite, at 143.0 and 138.2 eV are associated with the Pb^{+2}, as illustrated in **Figure 2j**. The binding energies of $I3d_{3/2}$ and $I3d_{5/2}$ in the pure perovskite are 630.6 and 619.1 eV, respectively, as shown in **Figure 2k**. In all treated films with the 2F, 3F and 5F organic spacers, both peaks of Pb and I shifted towards lower binding energy compared to the 3D control film (**Table S1**, Supporting Information). These downward shifts in binding energies suggest that the corresponding organic spacers interact with the uncoordinated Pb^{2+} ions and iodine atoms.[66] In addition, the downward shift in binding energy indicates that LDP facilitates charge transfer in the perovskite structure because the core level signals in the treated films are located closer to the Fermi level.[16,67] The most notable decrease in binding energies within the Pb4f and I3d spectra was observed in the perovskite film treated with 3F, as compared to those treated with 2F and 5F. This suggests that ($-NH_3$) in the 3F perovskite film may be in closer proximity to

the $[PbX_6]^{4-}$ octahedron because of enhanced hydrogen bond interactions caused by the electron-withdrawing impact of X-positioned F atoms.[68]

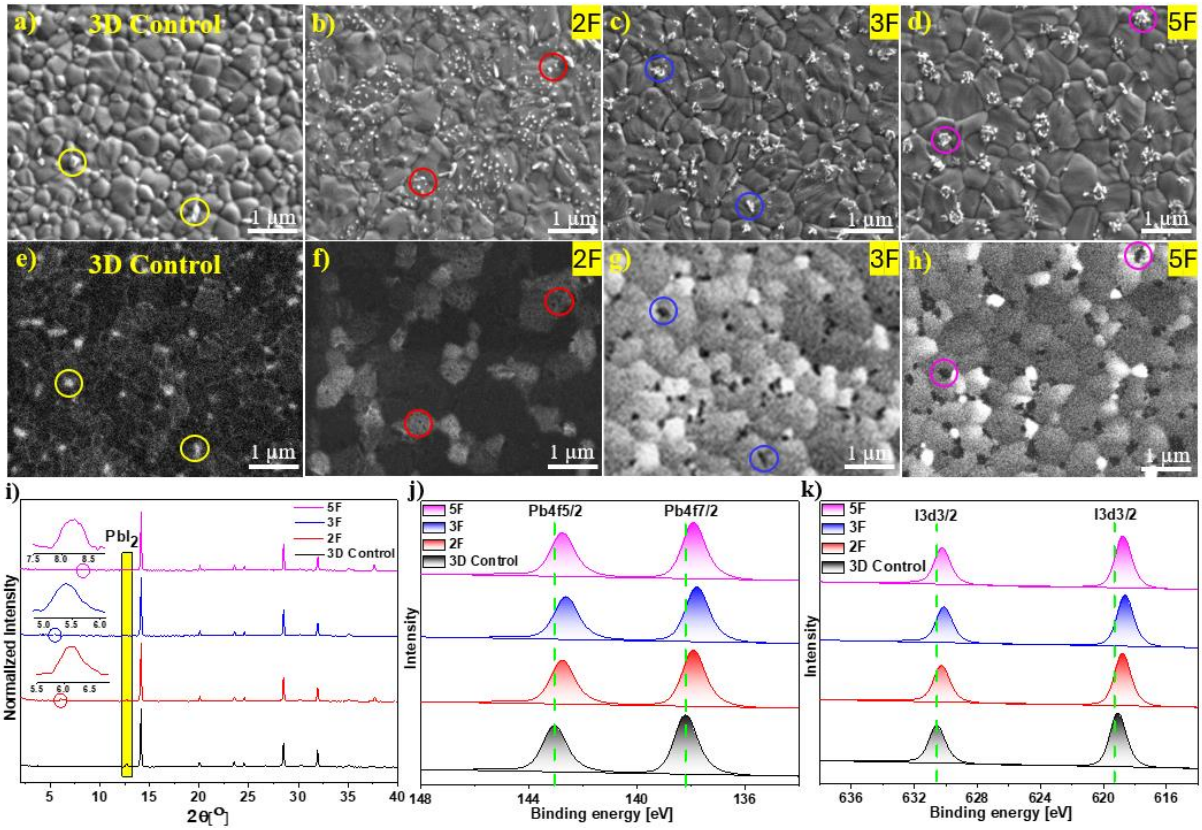

Figure 2. SEM images of 3D MAPI control film, 2F-3D/LDP, 3F-3D/LDP, and 5F-3D/LDP MAPI perovskite films were recorded using **a-d)** SED and **e-h)** CL detectors. **i)** XRD patterns and **j)** Pb 4f core level, **k)** 3d core level XPS spectra of 3D MAPI control film, 2F-3D/LDP, 3F-3D/LDP, and 5F-3D/LDP perovskite films**.**

Nuclear magnetic resonance (^{1}H-NMR) was employed to verify NH−I hydrogen-bonding interactions between organic spacers and inorganic lead iodide species (e.g. $[PbI_4(H_2O)_2]^{2-}$ or $[PbI_6]^{4-}$]) (**Figure S11**, Supporting Information). To indirectly support this observation, ^{1}H-NMR analysis was performed by mixing 3F molecule, containing -CF_3 group, with PbI_2, the building block of $[PbI_6]^{4-}$ octahedral in the 3D perovskite crystal. When the spacer and PbI_2 are combined, the protons of the formamidinium -NH_2 group in the organic cation that interact with PbI_2 experience a shift towards higher magnetic field values (shielding effect) compared to the ^{1}H-NMR spectrum of the pure 3F molecule. This indirectly indicates that the organic cation interacts with PbI_2 via the FA^+ cation end.[69]

Grazing incidence wide-angle X-ray scattering (GIWAXS) was employed to assess the

orientation of perovskite crystallites to the substrate in both the 3D control film and the treated perovskite film with 2F, 3F, and 5F organic spacers. The 3D reference material shows a random orientation, which can be seen through the diffraction rings displayed in **Figure 3a**.[70] The reflection at the azimuthal angle near 0°, beneath the first reflection ring related to 3D MAPI, corresponds to the (001) plane of PbI_2. 3D Control MAPI thin films commonly have an excess of PbI_2 due to surface deterioration of the perovskite layer and the excessive usage of PbI_2 in the perovskite precursor solution.[71] All other materials show similar reflections and random orientation for the 3D MAPI phase. In the 2F and 3F samples, the intensity of the PbI_2 reflections is reduced whereas it is not observable anymore for 5F as shown in **Figure 3b-d**, demonstrating the partial (2F and 3F) and complete (5F) consumption of the excess PbI_2. Furthermore, additional reflections in the low q region, below the first 3D MAPI reflection ring, can be observed for all three treated materials. For comparison with the XRD and TEM results, a pseudo 2 Theta plot of the low q scattering region is given (**Figure S12**, Supporting Information).

While the origin of these low-angle reflections was shown not to originate from the pure organic spacer materials, we cannot assign them unambiguously to a solved structure. Nonetheless, the large unit cell parameters required for the low q region scattering point towards the formation of low-dimensional phases on the surface of the 3D MAPI thin film. The lattice planes of the observed reflections of these LDPs are predominantly oriented parallel to the substrate, as seen by the reflections being located around the azimuthal angle of 0° as shown in **Figure 3b-d**. Lastly, for 3F the different orientation profiles of the additional reflections, i.e. a broad reflection ring at q_r = 3.37 nm^{-1} (4.76° 2θ) and a sharp reflection at q_r = 4.08 nm^{-1} (5.72° 2θ) could point to more than one new phase being present.

HR-TEM studies were conducted to clarify the structural features of the 3D/LDP MAPI samples treated with 3F, as depicted in **Figure 3e, f**. The interplane spacings, which are assessed from the Fast Fourier transform (FFT) images and correlate to the fingerprint of LDP lattice fringes, are visible in the HR-TEM images. The HR-TEM images from certain areas validate the presence of different lattice spacings. The small distance between adjacent crystal planes of 3.2 Å is associated with the (220) diffraction peak of the 3D MAPI tetragonal phase (COD file: 1548467) as shown in **Figure 3e**.[72] Furthermore, the 3F-treated perovskite films show interplanar *d*- spacing of 7.1, 7.7 and 11.8 Å, which are correlated with the LDP (**Figure 3e, f)**. The observed interplanar d-spacings in HR-TEM are mainly consistent with those of 2D

LDP as reported in previous studies in the literature.[73-74] Furthermore, The XRD and GIWAXS studies also support the 2D LDP formation within the 3D MAPI structure.[47, 75] These results indicate that the final structure we obtained is potentially a mixed-dimensional 3D/2D PSCs.

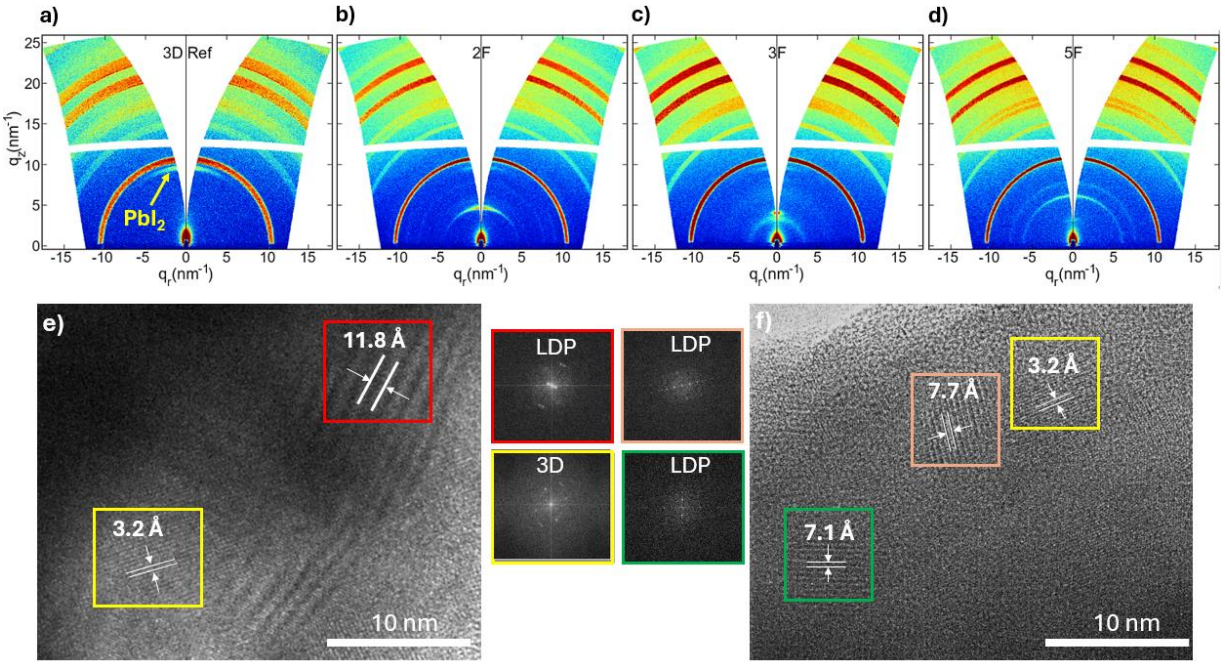

Figure 3. GIWAXS data of **a)** 3D control MAPI (with +5% excess PbI_2), **b)** 2F- 3D/LDP, **c)** 3F- 3D/LDP, **d)** 5F- 3D/LDP perovskite films. **e, f)** TEM images of 3D/LDP perovskite film treated with 3F and corresponding fast Fourier transforms (FFT) taken from the marked areas.

Our experimental results suggest that the treatment with the fluorine-functionalized organic cations has the potential to improve the efficiency as well as the stability of the MAPI-based solar cells, as a result of LDP formation. We hypothesize that these fluorinated organic spacers passivate also defects on grain boundaries and surfaces of the perovskite film at molecular level, as shown schematically in **Figure 4a**. To gain more insight into the effect of these fluorinated spacers, we conduct DFT calculations to examine the interactions between the used agents and the 3D MAPI surface.

We started with an MA-I terminated perovskite surface and replaced MA cations with xF cations to compare the stability of these modified perovskite surfaces relative to that of 3D MAPI, shown as in **Figure 4b**. In addition to the xF cations studied experimentally in this work, we also investigated the effect of the NH group in passivating the surface by substituting it with a CH_2 group in the 3F cation. This organic spacer will be referred to as 3FC, amphiphilic

4-(trifluoromethyl)benzylammonium iodide (TFMBAI), which is often reported as a passivation agent previously in literature.[52] To assess the stability of adsorbed molecules, we performed calculations of the binding energy (E_b) for the MA-I ion pair and xF-I structures on the Pb-I terminated perovskite surface. Details of the structural models and the calculations can be found in supporting information note for DFT calculations. The calculations were done both for full coverage and low coverage (25%) of the surface with xF organic spacers, as shown in **Figure 4b**.

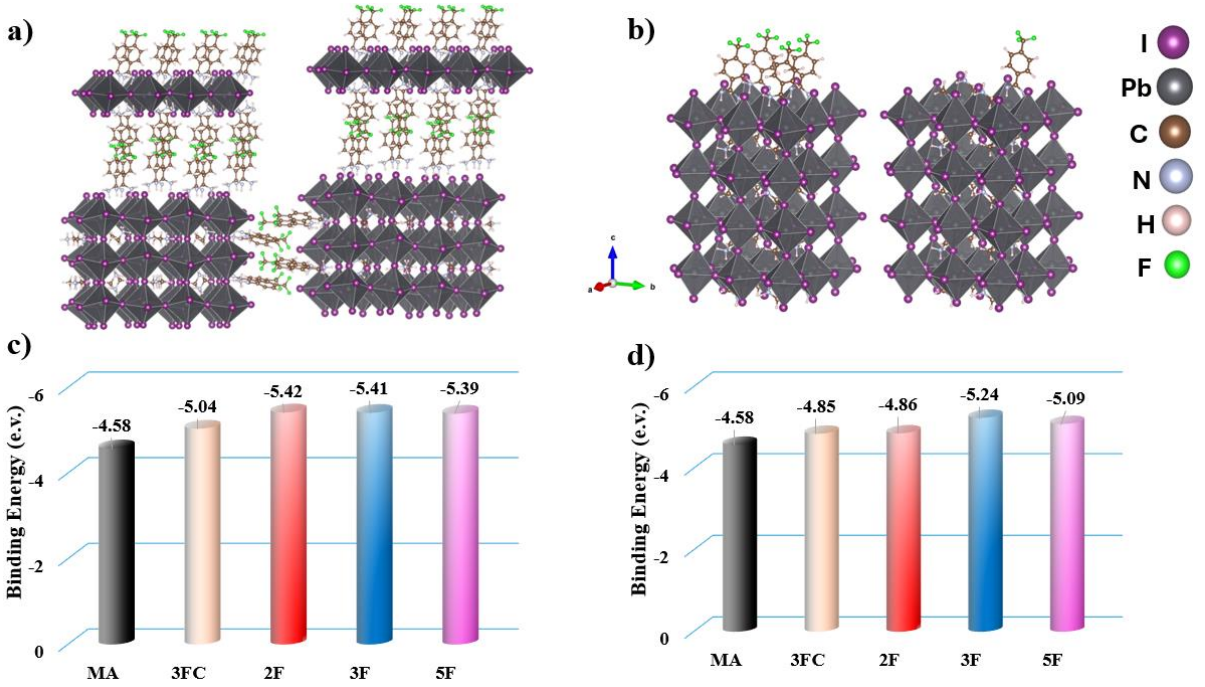

Figure 4. a) A schematic illustration showing how an LDP layer is formed on top of a 3D MAPI, with a perovskite grain boundary passivated by fluorinated organic spacers.; **b)** a diagram showing the perovskite surface with partially fluorinated organic spacers decoration on the right and full organic spacer decoration on the left.; **c)** the binding energy for the perovskite surface fully covered with fluorinated organic cations; **d)** the binding energy for the perovskite surface with a low coverage of fluorinated organic cations.

The E_b calculation results for the surface fully and partially covered with fluorine-functionalized organic cations are shown in **Figure 4c** and in **Figure 4d** respectively. When considering the entire coverage, it is evident that the perovskite surface has a better passivation effect because all the fluorinated organic cations bind to the Pb-I ended surface more firmly than the MA and 3FC organic spacer. Whereas 2F, 3F, and 5F cations have approximately the same Eb, interestingly, a more distinct trend becomes apparent when reducing the coverage. 3F forms the strongest bond with the surface, followed by 5F and 2F as shown in **Figure 4d**.

This trend can be explained by the dipole moments of the fluorinated molecules themselves, in **Figure 1e**, where the larger dipole moment of the molecule corresponds to stronger binding to the surface. This trend is the same as the one experimentally established for the PCE, confirming the most effective defect passivation effect of the 3F organic spacer.

It is important to mention that only very small amounts of the organic cations were used in our experiments. This suggests that it is unlikely for the passivation with organic spacers to fully cover the surface, therefore 3F emerges as the best passivator at low coverage. However, using a large amount of organic cations may also have drawbacks. The insulating character of the organic spacers can be attributed to their predicted band gaps, which exceed 3 eV in according to DFT calculations. Among the organic spacers, 5F has the highest insulation (**Figure S13,** Supporting Information). Applying high concentration of the organic spacers can therefore hinder the charge transport, since the insulating properties of the fluorinated compounds would be more dominant than the beneficial effect of passivation. We highlight that the passivation effect of these organic cations also improves the stability and performance of the perovskite films and devices, by immobilizing surface halide species and passivating dangling Pb bonds. Here, with the largest surface binding energies, both 3F and 5F significantly improve the long-term stability of the solar cells, with 5F being slightly superior to 3F due to its more hydrophobic nature, as demonstrated in **Figure 6a.**

UV-vis absorption spectroscopy was used to study the optoelectronic properties of the perovskite films shown in **Figure 5a**. Compared to the 3D MAPI control film, surface-modified 3D/LDP films (approximately 550 nm thick, **Figure S14,** Supporting Information) exhibit no notable absorption differences. It indicates that the presence of the LDP phase atop the 3D structure does not cause a significant change in the absorption characteristics of the photoactive film.

As depicted in **Figure 5b-c**, steady-state photoluminescence (SSPL) and time-resolved photoluminescence decay (TRPL) measurements were performed on the 3D MAPI control and treated 3D/LDP perovskite samples to elucidate the charge recombination processes. The passivated film including 2F shows slightly increased peaks in PL emission, while the pristine perovskite films modified with 3F and 5F demonstrate elevated PL emission peaks, as depicted in **Figure 5b**.

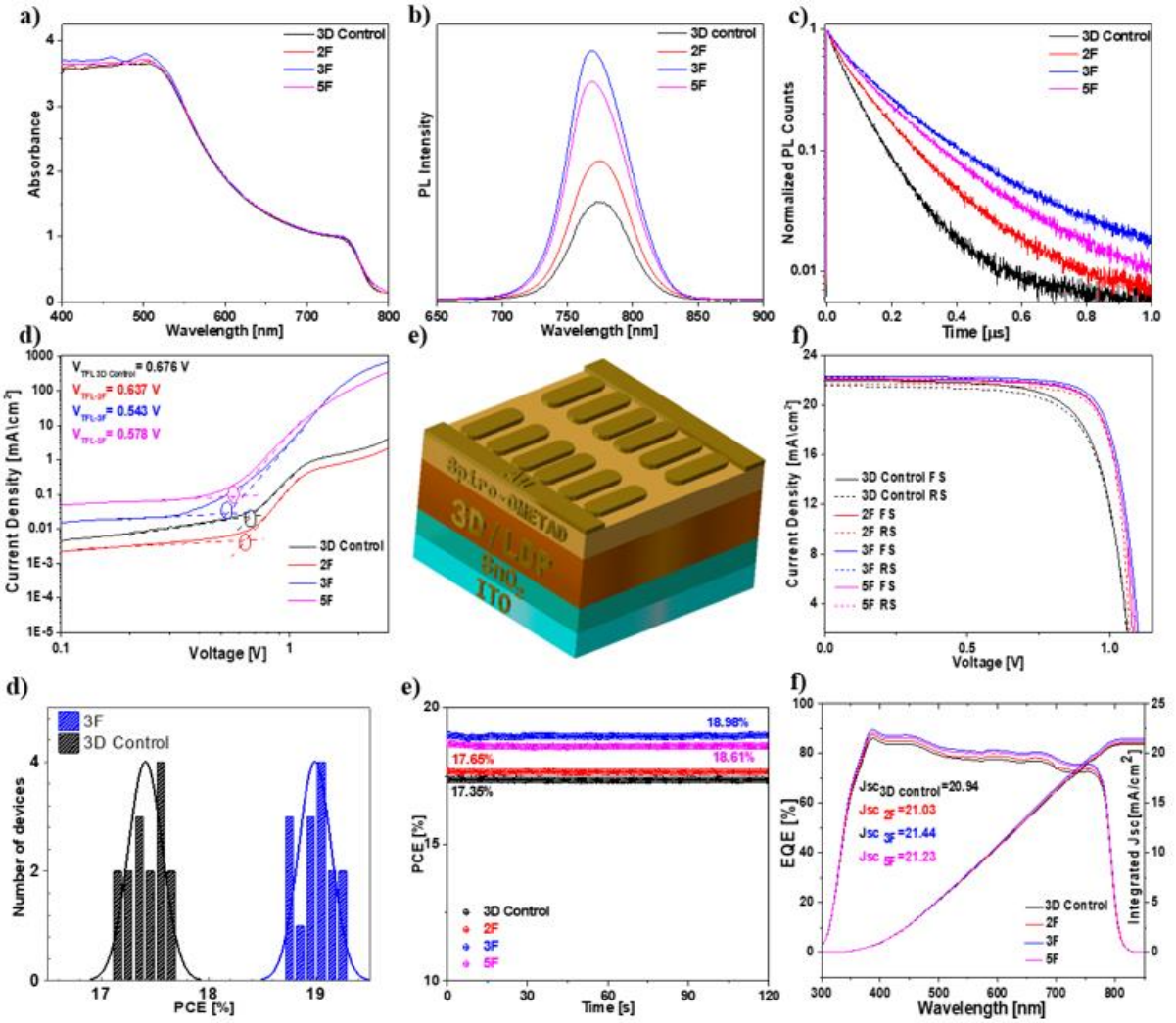

Figure 5. a-c) Absorption, SSPL and TRPL spectra of 3D MAPI control, 2F-3D/LDP, 3F-3D/LDP, and 5F-3D/LDP perovskite films on glass substrate. **d)** SCLC curves of the Electron only devices for 3D MAPI control, 3D/LDP with 2F, 3F and 5F. **e)** Device structure of corresponding PSCs reported in this study. **f)** *J-V* curves of champion devices of 3D control 2F-3D/LDP, 3F-3D/LDP, and 5F-3D/LDP perovskite films respectively. **g)** Histograms display the distribution of PCE for both the 3D control and 3F-3D/LDP PSCs, for 15 devices each. **h)** The MPP of PSCs under AM 1.5G light. **i)** EQE of corresponding devices.

The high PL intensity serves as an indicator of the elimination of defect-related sub-bandgap states in perovskite films.[76] The observed high PL emissions in 3D/LDP perovskite films treated with 3F and 5F can be attributed to ability of the surface defect passivation and LDP phase formation to inhibit non-radiative recombination losses. **Figure 5c** illustrates the TRPL decay spectra of the films that were prepared on glass substrates. The TRPL curve was fitted with the biexponential equation (1) given below:

$$y = A_1 exp\,(\frac{-t}{\tau_1}) + A_2\, exp(\frac{-t}{\tau_2}) + y_0 \qquad (1)$$

where A_1 and A_2 denote the signal amplitudes. The symbols τ_1 and τ_2 represent, the short and long charge carrier recombination times, respectively. In essence, τ_1 is linked to nonradiative trap-assisted recombination taking place at the perovskite grain boundaries, while τ_2 is associated with bulk carrier recombination, conversely.[67,77]

A compilation of the charge carrier lifetimes of the perovskite films is provided in **Table S2**, Supporting Information. The respective τ_1 and τ_2 values in the 3D control film are 50 and 114 ns, respectively. There is no major change in these values in the film treated with 2F. In particular, the 3F-treated 3D/LDP perovskite films exhibit considerably longer τ_1 and τ_2 values than the control sample. The diminished τ_1 value signifies that in the passivated 3F and 5F 3D/LDP, radiative recombination of carriers predominates over trap-assisted nonradiative recombination. Reduced nonradiative recombination is likely linked to a lower defect density, as indicated by the extended lifetimes. This, in turn, promotes charge carrier transport and contributes to an increased open-circuit voltage (V_{oc}).[78]

The trap-state density of the corresponding films was determined using the space-charge-limited current (SCLC) method, which is applicable to electron/hole-only devices. The equation (2) for this calculation is as follows:

$$N_t = 2\varepsilon\varepsilon_0 V_{TFL}/qL^2 \quad (2)$$

Where N_t represents the electron or hole trap-state density, ε is the relative dielectric constant of MAPI perovskite (ε = 25), ε_0 represents the vacuum permittivity (8.85×10^{-12} F m^{-1}), V_{TFL} signifies the trap-filled limit voltage, q is the fundamental charge (1.602×10^{-19} C), and L symbolizes the thickness of the perovskite film. For this experiment, electron-only devices were produced and current density-voltage (J-V) curves in the dark were collected as shown in **Figure 5d**.[79] The ohmic region is the linear segment observed in the dark J-V curve at low bias voltage. The region characterized by an intermediate bias, where charge carriers occupy traps, is termed the trap-filled region. The region devoid of traps is established at the high-bias voltage. The bias voltage at the inflection points between the ohmic region and the trap-filled region is used to calculate the V_{TLF}. The calculated trap state density of the 3D MAPI control device is 6.17×10^{15} cm^{-3}. The trap-state density of the 3D/LDP perovskite the 2F device is measured at 5.88×10^{15} cm^{-3}. Although the trap density value of the 2F-modified device is lower compared to the 3D control, there is no significant difference. The trap-state densities of 3F and 5F-designed 3D/LDP perovskites were determined to be 4.97×10^{15} cm^{-3} and 5.26×10^{15}

cm^{-3}, respectively. The 3D/LDP perovskite device with 3F demonstrates the least trap-state density. This confirms the passivation impact of the fluorinated organic spacers and LDPs , reducing nonradiative recombination and facilitating efficient charge transfer. These factors are pivotal for improving the photovoltaic performance of PSCs.

To assess the impact of the molecular passivation and LDPs on the photovoltaic performance, the *n-i-p* planar (ITO/SnO_2/3D or 3D/LDP/Spiro-OMeTAD/Au) PSCs with 3D MAPI and 3D/LDP mix-dimensional were fabricated as shown in **Figure 5e**. The results of the best performing devices, as determined through *J-V* characterization at an Air Mass (AM) of 1.5G (1000 W/m^2), are depicted in **Figure 5f** and detailed in **Table S3** (Supporting Information). Furthermore, statistical distributions are provided for the photovoltaic parameters to demonstrate the reproducibility of the corresponding devices within acceptable limits as well as to define the best concentration value of LDP film. (**Figure S15-S17**, Supporting Information).

The 3D MAPI control perovskite device achieved a short-circuit current density (J_{sc}) of 21.99 mA/cm², an V_{oc} of 1.07 V, and a fill factor (FF) of 74%. Consequently, the best-performing control device attained a PCE of 17.62%. As can be seen in the forward and reverse scans, the 3D control unit suffers from hysteresis. When optimizing with 2F, the efficacy of 3D/LDP PSCs does not increase significantly (17.91%) in comparison to the 3D control. Concerning the 3D/LDP devices treated with 5F, there is an observed improvement in PCE to 18.93% with an increased V_{oc} of 1.09 V, a higher J_{sc} of 22.13 mA/cm², and an elevated *FF* of 76%. The highest performance of 19.22% was achieved by 3D/LDP PSCs treated with 3F, outperforming other devices. The 3F-treated 3D/LDP devices have the following photovoltaic parameters: V_{oc} = 1.10 V, J_{sc} = 22.34 mA/cm^2, and *FF* = 77%. The observable rise in V_{oc} suggests that the trap-assisted recombination associated with defects is alleviated through the surface defect passivation and formation of the low-dimensional LDP phase at the grain boundaries of the 3D perovskite, achieved with 3F and 5F organic spacers. Additionally, the improvement in V_{oc} and *FF* is further facilitated by the acceleration of charge transport induced by surface dipoles. The higher dipole moment and lower band gap (3.26 eV) of 3F molecule, as determined by DFT, can be attributed to its superior PV performance compared to the 5F (3.54 eV) (**Figure S13**, Supporting Information).

Moreover, the reproducibility of PSCs devices is assessed by conducting tests on 15 cells to determine the influence of the 3F passivation on the performance of the devices, as depicted in

Figure 5g. The optimal power output at the maximum power point (MPP) is achieved by the top-performing devices when operating under 40-45% relative humidity (RH) conditions within the initial 2-minute period, as illustrated in **Figure 5h**. The average PCE of the PSCs treated with 3F is calculated to be 18.98%, which closely matches the PCE obtained from J-V measurements.

The external quantum efficiency spectra (EQE) of the PSCs were measured due to their identical optical absorption spectrum as shown in **Figure 5i**. Given their identical optical absorption spectrum slight change has been observed in the range from 300 to 850 nm. The 2F-treated 3D/LDP hybrid device exhibits an integrated J_{sc} response of 21.03 mA/cm^2, similar to the 20.94 mA/cm^2 of the 3D MAPI control. The integrated J_{sc} values for the 3F and 5F modified 3D/LDP PSCs samples surpass those of the control device, with values of 21.44 mA/cm² and 21.23 mA/cm², respectively. After treatment with the corresponding organic cations of the perovskite layer, the PSCs show improved efficiency in converting the absorbed light into electrical energy, which is even more evident for 3F-3D/LDP-PSCs.

The stability of unencapsulated devices was examined in ambient air conditions (room temperature, RH (40–45%), as depicted in **Figure 6a**. Perovskite devices treated with 2F and 3F kept 74% and 85% of their PCE following a 1000 h stability test in the dark respectively. In comparison, the PCE of the untreated 3D control device decreased to 70% of its initial value. The 5F-modified 3D/LDP PSCs exhibited superior environmental stability compared to other devices, retaining 88% of their initial PCE after 1000 h under a N_2 atmosphere (dark), which is quite comparable with 3F-modified 3D/LDP PSCs (retaining 85% of their initial PCE after 1000 h). In contrast, the long-term stability of the 2F-treated perovskite films was negligible, similar to that of the 3D control device.

A light-thermal stability test was also performed on the devices by exposing them to one sun at 60 °C for 800 mins in an N_2 environment. The 3D/LDP perovskite device treated with 5F exhibited the highest light-thermal stability, maintaining 80% of its initial efficiency after 12 h of continuous light soaking, as depicted in **Figure 6b**, followed with 3F-treated device maintaining 75% of its initial efficiency. The PCE of 3D MAPI control and 2F-treated 3D devices reduced to 52% and 58% of their initial values, respectively. The increased stability observed in the 5F- and 3F-modified devices is attributed to several factors such as the formation of LDP phase and higher hydrophobicity, which is believed to impede ion migration and moisture infiltration, improve film quality, and reduce defects in the perovskite layer.

Although the 3F molecule has higher E_b, the increased hydrophobicity of the 5F molecule provides slightly better stability, hence preserving the PCE performance. On the other hand, the lower stability in 2F treated films can be explained with the smaller binding energy and lower hydrophobicity. The rapid degradation of all devices under light-thermal stress can be attributed to the presence of the spiro-OMeTAD layer in the device architecture.[80]

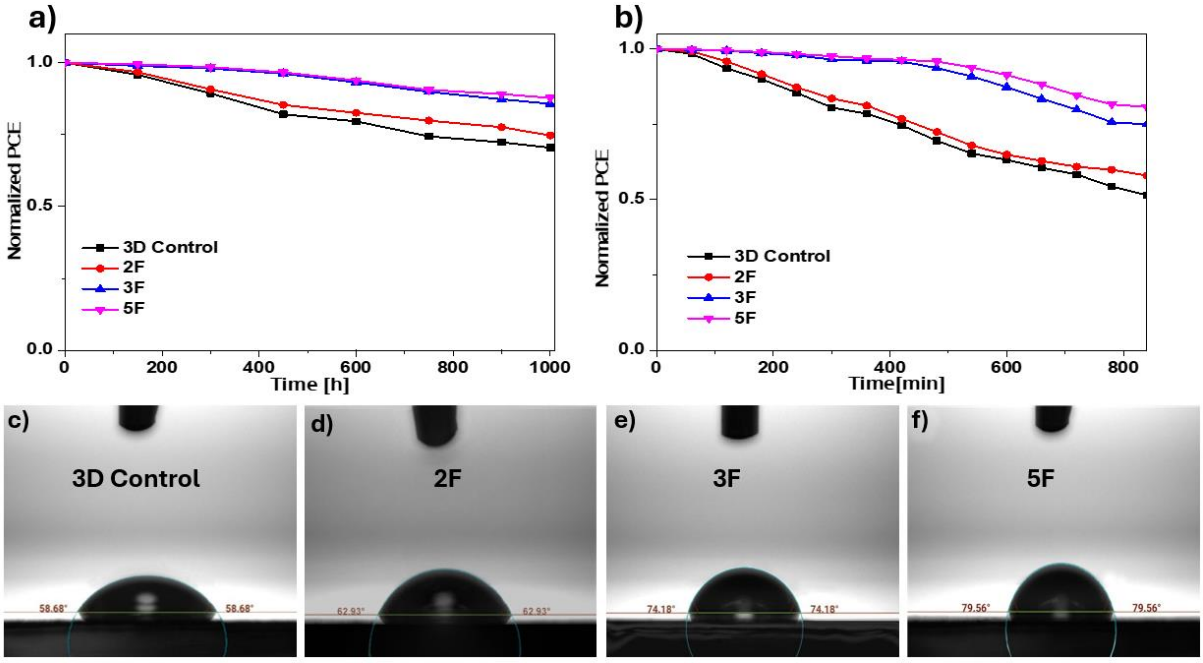

Figure 6. a) Long-term stability tests, and **b)** light-thermal stability curves of 3D control, 2F-3D/LDP, 3F-3D/LDP, and 5F-3D/LDP. Contact angle measurements of **c)** 3D MAPI control, **d)** 2-F, e) 3F-, and **f)** 5F-treated 3D/LDP perovskite film.

To investigate the effect of the hydrophobic nature of the F atom on stability, in conjunction with the F-number of the organic spacers, the water contact angles of 3D/LDP perovskite films treated with 2F, 3F, and 5F were evaluated in comparison to the 3D MAPI control film as shown in **Figure 6c-f**. The 5F-modified 3D/LDP structure has the largest water contact angle, measuring around 79°, followed with 3F-modified 3D/LDP perovskite film with contact angle of around 74°. In contrast, the water contact angle of the 2F-modified 3D/LDP perovskite film is roughly 62°, quite close to that of the 3D MAPI control film (58°). We can deduce that LDP passivation in general has a favorable effect on the water contact angle, resulting in hydrophobic surface.

4.3. Conclusion

In summary, fluorine functionalized organic spacers were used to reduce defects and to fabricate mixed-dimensional 3D/LDP MAPI perovskite devices. DFT calculations showed that the 3F has the highest molecular dipole moment, followed by the 5F and 2F. When considering partial coverage, the calculated E_b of these fluorinated organic spacers on the Pb-I-terminated perovskite surface, follows an increasing trend in the sequence: 2F, 5F, and 3F. The efficacy of the passivating organic spacers and LDP was demonstrated by SSPL and TRPL studies, which suggested possible decreases in non-radiative recombination losses in treated perovskite films. CL analysis was utilized to provide a more comprehensive understanding of the emission characteristics of both the untreated and treated perovskite films. Although the 3D control displayed emission from both MAPI and excess PbI_2, the treated films that formed LDP exhibited non-emissive properties from the agglomerates and emitted a signal from the 3D MAPI. Low-dimensional phases were revealed by additional investigations using XRD, GIWAXS, and HR-TEM. These analyses also revealed changes in crystallinity, surface composition, and crystallite orientation of the passivated films.

Among these fluorinated spacers, the 3F structure showed the highest PCE. Firstly, its higher dipole moment potentially increases the dielectric constant, reducing the Coulomb force between the exciton's electron and hole pair in the formed low-dimensional perovskite phases, thereby promoting effective charge separation. Secondly, the molecular structure of 3F, with its higher flexibility and trifluoromethyl unit located in the para position of the benzene ring rather than a direct attachment of F atoms to the benzene ring, gives rise to larger molecular dipole and facilitates more effective interaction between its amino group and the perovskite surface. This leads to enhanced defect passivation and, consequently, improved device performance. In addition, the presence of three F atoms in 3F provides an optimal balance that gives the perovskite layer sufficient hydrophobicity to protect it from moisture without compromising the electronic properties of the material. Therefore, 3F emerges as the most promising structure, offering an ideal combination of efficiency and stability.

Our study highlights the intricate relationship between surface morphology, molecular structure, and optoelectronic characteristics in PSCs, providing valuable insights for optimizing and improving device performance, while also emphasizing the key role of molecular design in tuning these properties through comparative analyses of these organic spacers within the same family group.

4.4 Experimental Section

Materials and reagents

The SnO_2 colloid precursor, containing tin (IV) oxide at 15% in H2O colloidal dispersion, was procured from Alfa Aesar. Prior to spin-coating as an electron transport layer (ETL), the SnO_2 nanoparticles were diluted with deionized water (DI) to a concentration of 2.67 wt.%. The organic spacer precursor 2-(2-thienyl) pyridine (98% unprotonated form), as well as PbI_2 and methyl ammonium iodide (MAI), were sourced from TCI. Solvents such as dimethyl sulfoxide (DMSO), N,N-dimethylformamide (DMF), and others, along with freshly delivered hydroiodic acid (HI ~57 wt.%), were obtained from Sigma-Aldrich. The hole transport layer (HTL) material, 2,2′,7,7′-tetrakis-(N,N-di-4-methoxyphenyl amino)-9,9′-spirobifluorene (Spiro-OMeTAD), was purchased from Borun Chem. 4-(trifluoromethyl)benzonitrile, 3,5-difluorobenzonitrile, 2,3,4,5,6-pentafluorobenzonitrile, Trimethylaluminum ($Al(CH_3)_3$), NH_4I, and toluene were purchased from commercial suppliers and used as received. All solvents were dried according to standard procedures. Air-sensitive reactions were carried out under nitrogen atmosphere. Analytical thin-layer chromatography (TLC) was performed using aluminum-coated Merck Kieselgel 60 F254 plates.

Synthetic details and characterization

The corresponding fluorinated benzene-1-carboximidamidium iodide was synthesized with a slight modification of a previously reported procedure. All the compounds showed identical spectroscopic properties to those reported therein.[1-5]

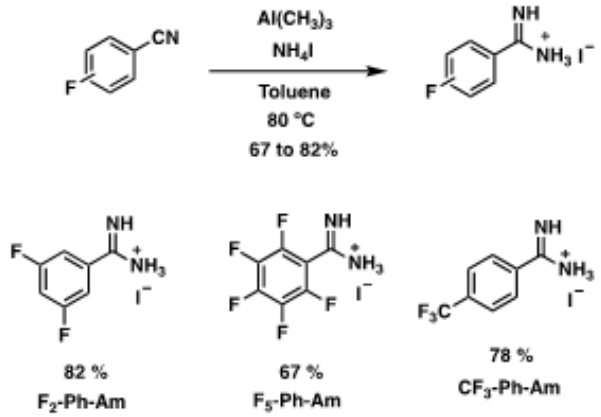

Figure S1. Synthetic pathway for the preparation of fluorinated benzene-1-carboximidamidium iodide.

Over a suspension of NH_4I (3 eq) in dry toluene (15 mL), a 2M solution of $AlMe_3$ in toluene (3 eq) was added dropwise at 0 ºC using an ice bath under N_2 atmosphere. After the addition,

the mixture was warmed to r. t. and stirred for 1 h until gas evolution ceased. Then, the corresponding fluoro-substituted benzonitrile (1 eq) was added to the mixture dissolved in additional dry toluene (15 mL). The mixture was heated at 80 ºC during 48h. After cooling down to r. t., the reaction the reaction was quenched with the addition of MeOH and a white precipitate was formed. The white solid was removed by filtration and washed with additional MeOH. The organic solvents were removed under reduced pressure and the remaining solid was suspended in diethyl ether, filtered and washed with additional diethyl ether and pentane to afford the fluorinated benzenecarboximidamidium iodide as off-white solids, yielding from 67 to 82%. The organic cations were used for device fabrication without further purification.

Synthesis of 3,5-difluorobenzene-1-carboximidamidium iodide (2F)

Following the general procedure, 3,5-difluorobenzonitrile (1 g, 7.19 mmol), $AlMe_3$ (21.57 mmol, 10.8 mL) and NH_4I (3.13 g, 21.57 mmol) were mixed to give rise the desired benzenecarboximidamidium iodide salt (1.67 g, mmol, 82 % yield). ^{1}H NMR (400 MHz, DMSO-d_6) δ/ppm: 8.54 (s, 1H), 8.50 (s, 2H), 7.84 (br, 4H); ^{19}F NMR (376 MHz, DMSO-d_6, 298 K) δ/ppm: -61.27 (s) ppm; Mass analysis calcd for $C_7H_7F_2N_2^+$ [M^+], 157.05; found 157.0.

(trifluoromethyl)benzene-1-carboximidamidium iodide (3F)

Following the general procedure, 4-(trifluoromethyl)benzonitrile (1 g, 5.84 mmol), $AlMe_3$ (17.53 mmol, 8.8 mL) and NH_4I (2.54 g, 17.53 mmol) were mixed to give rise the desired benzenecarboximidamidium iodide salt (1.44 g, mmol, 78 % yield). ^{1}H NMR (400 MHz, DMSO-d_6) δ/ppm: 8.03 (m, 4H), 7.81 (br, 4H); ^{19}F NMR (376 MHz, DMSO-d_6, 298 K) δ/ppm: -61.68 (s) ppm; Mass analysis calcd for $C_8H_8F_3N_2^+$ [M^+], 189.06; found 189.0.

2,3,4,5,6-pentafluorobenzene-1-carboximidamidium iodide (5F)

Following the general procedure, 2,3,4,5,6-pentafluorobenzonitrile (1 g, 5.18 mmol), $AlMe_3$ (15.54 mmol, 7.8 mL) and NH_4I (2.25 g, 15.54 mmol) were mixed to give rise the desired benzenecarboximidamidium iodide salt (1.17 g, mmol, 67 % yield). ^{1}H NMR (400 MHz, DMSO-d_6) δ/ppm: 7.57 (br, 4H); ^{19}F NMR (376 MHz, DMSO-d_6, 298 K) δ/ppm: -138.84 (m), -147.15 (t, J = 17 Hz), -160.21 (m) ppm; Mass analysis calcd for $C_7H_4F_5N_2^+$ [M^+], 211.03; found 211.0.

Fabrication of 3D/LDP Perovskite Solar Cells

Prior to further processing, the ITO substrates measuring 3 cm x 3 cm underwent a sequence of cleaning procedures. Initially, they were etched using a solution consisting of 3 M

hydrochloric acid (HCl) and Zn powder and then cleaned by washing with deionized water. Afterwards, the substrates underwent sequential sonication in a 2% detergent (Hellmanex™ III) solution, DI water, ethanol, and isopropanol, with each step lasting 15 minutes. Subsequently, the specimens were subjected to nitrogen flow drying and subsequently exposed to nitrogen plasma for 15 minutes. The ITO substrate was spin-coated with a diluted solution of SnO_2 nanoparticles (2.67 wt% in water) at 4000 rpm for 35 seconds in air, followed by 30 minutes of annealing at 150°C in air. Before perovskite coating, the SnO_2-coated substrates were subjected to an additional 10-minute cleaning stage in a UV-O_3 environment. To deposit perovskites, the precursors employed in the one-step "anti-solvent" method were PbI_2 (1.68 M, 5% excess), MAI (1.60 M), and DMSO (1.60 M) in 1 mL DMF. These precursors were applied to the SnO_2 layer. After 10 seconds of deposition at 1000 rpm, the material was rapidly spun at 3500 rpm for 20 seconds. Anti-solvent ethyl acetate was introduced onto the perovskite film in the final 10 s of the spinning process. The sample was subsequently annealed at 130°C for ten minutes. To apply surface treatment to the perovskite films, a solution containing 2 mg/ml of each organic spacers in isopropanol was spin-coated onto the films at 4000 rpm for 30 seconds. Subsequently, the substrate was subjected to heat treatment at 100°C for 5 minutes. A solution consisting of 72.3 mg spiro-OMeTAD, 35 µl bis(trifluoromethane) sulfonimide lithium salt (LiTFSI) stock solution (270 mg LiTFSI in 1 ml acetonitrile), 30 µl 4-tert-butylpyridine, and 1 ml chlorobenzene was spin-coated to deposit the hole transport material (HTM). The process lasted 30 seconds at 3000 rpm. A 70 nanometer thin film of Au was subsequently thermally evaporated onto the HTM layer under a high vacuum.

General characterization techniques:

Nuclear Magnetic Resonance spectroscopy (NMR): was recorded on a Bruker Advance 300 (^{1}H: 400 MHz; ^{13}C: 101 MHz) spectrometer at 298 K using partially deuterated solvents as internal standards. Coupling constants (J) are denoted in Hz and chemical shifts (δ) in ppm. Multiplicities are denoted as follows: s = singlet, d = doublet, t = triplet, m = multiplet.

FTIR spectra: were recorded on a Bruker Tensor 27 (ATR device) spectrometer.

Mass spectra: were performed using a Mass Spectrophotometer QTOF Bruker Impact II using electrospray ionization (ESI).

UV–vis absorption (UV-vis)*:* measured using a Perkin Elmer Lambda 1050 spectrometer equipped with an integrating sphere.

Photoluminescence (PL): spectroscopy utilized a Picoquant Fluotime 300 spectrofluorometer, employing an excitation wavelength of 375 nm. Current-voltage (J-V) characteristics were measured under ambient conditions using a Newport OrielSol 2A solar simulator (AM 1.5G - 100 mW cm^{-2}) in conjunction with a Keithley 2400 source meter.

The solar simulator: The solar simulator was calibrated using a silicon cell certified by Fraunhofer ISE with KG5-filtered light. The active area of the solar cells was defined by a square metal aperture mask, with an area equal to 0.0831 cm^2. J-V curves were recorded by scanning the input bias from -0.1 V to 1.2 V (forward scan) at a scan rate of 0.1 V/s after maintaining the devices at 1.2 V for 5 seconds under illumination. For light intensity-dependent J-V measurements, a white light LED served as the light source, with intensity adjusted using a Keithley 2200-20-5 Power Supply. A highly linear photodiode controlled the light intensity within the range of 0.1 – 1.2 suns, and J-V curves were measured using a Keithley 2401 source meter.

External Quantum Efficiency (EQE): For acquiring EQE spectra, the photovoltaic cells underwent illumination with modulated light from a tungsten lamp, directed through a monochromator. The light beam was then divided to simultaneously illuminate the sample and a reference silicon photodetector (Hamamatsu S2281-01). The wavelength-dependent current responses of both devices were recorded concurrently using two lock-in amplifiers (Signal Recovery 7265, Stanford Research Systems 830) at a chopping frequency of 14 Hz. The incident illumination power, determined through the reference photodetector, was utilized to calculate the EQE response of the perovskite solar cell.

X-Ray Diffraction (XRD): was conducted using a Bruker D8 Discover X-ray diffractometer, operated at 40 kV and 30 mA. The diffracted X-ray beam passed through a Ni filter, and Cu Kα1 radiation (λ = 1.5406 Å) along with a position sensitive LynxEye detector was employed.

Powder X-Ray Diffraction (P-XRD): measurements were performed using a STOE STADI P diffractometer in Debye–Scherrer geometry, operating at 40 kV and 40 mA. The system utilized monochromated Cu-Kα1 radiation (λ = 1.5406 Å) with a Ge(111) single crystal monochromator and a DECTRIS MYTHEN 1K detector.

Grazing-incidence wide-angle X-ray scattering (GIWAXS): Measurements of GIWAXS data were conducted using an Anton-Paar Saxspoint 2.0 equipped with a Primux 100 microfocus source utilizing Cu-Kα1 radiation (λ = 1.5406 Å) and a Dectris Eiger R 1M 2D Detector.

Scanning Electron Microscopy (SEM) Cathodoluminescence (CL): SEM/CL analysis was carried out through a field-emission scanning electron microscope (JSM-7100f, JEOL) equipped with secondary electron detector (SED), backscattered electron detector (BED) and cathodoluminescence (CL) detector (MonoCL4, GATAN). CL maps have been acquired in panchromatic mode. Beam parameters for SED/BED imaging: beam energy 5 KeV; probe current 0.1 nA. For SEM/CL mapping: beam energy 2 KeV; probe current ~0.06 nA.

Atomic Force Microscopy (AFM)**:** measurements were conducted in NeaSNOM instrument (AFM mode) from attocube systems AG. Silicon tips (Arrow-NcPt) were used at a resonant frequency (R.F ~ 258 kHz) in intermittent contact mode and at a tapping amplitude of 80 nm before landing. Gwyddion software was used for image processing and the images shown were flattened by plane subtraction and background polynomial removal**.**

HR-TEM studies**:** Transmission Electron Microscopy (TEM) investigations were performed using a JEOL 2100F instrument operating at 200 kV. MAPI perovskite thin films served as the source material. Sample preparations involved removing the perovskite from the substrate and transferring it onto the surface of a lacey coated copper TEM grid.

Space-Charge Limited Current (SCLC): To assess the impact of surface passivation on trap-density using the SCLC technique, electron-only devices consisting of ITO/SnO_2/MAPI with or without ThPyI/PCBM/Au were fabricated. The electron-only device configuration for bulk-passivated 3D MAPI is ITO/SnO_2/Perovskite with 2F (or 3F or 5F)/PCBM/BCP/Ag.

X-ray Photoelectron Spectroscopy (XPS): analyses were taken with a Thermo Scientific XPS microprobe using monochromatic Al Kα X-ray.

DFT Calculations: DFT calculations were performed using the Projector Augmented Wave (PAW) method as implemented in the Vienna Ab-initio Simulation Package (VASP).[6-8] The Perdew, Burke, and Ernzerhof (PBE) functional was used as the exchange-correlation functional within the generalized gradient approximation.[9] To account for van der Waals (VdW) interactions, the D3 correction was employed.[10] The force and energy convergence criteria in the calculations were set to 0.02eV/Å and 10^{-5}eV, respectively.

For the geometry optimization, and the calculations of the binding energies, MAI-terminated $MAPbI_3$ slabs were used, composed of a 2x2x3 super cell and a vacuum region of ~ 20Å to separate the slabs. The primitive unit cells used are cubic with a lattice parameter of a=6.37Å. A 3x3x1 Monkhorst-Pack k-point mesh was used.[11] The plane-wave basis cutoff energy was

set to 500 eV. During the geometry optimization, the atomic positions of the top and the bottom layers were allowed to relax, and the middle layer remained fixed.

To study the effect of passivation ligands, the surface of the slab is changed from MA-I to xF-I layers, after which the slab is relaxed again. The binding energy of low coverage of the xF-I on the Pb-I terminated surface was calculated using the equation:

$E_b = E(\mathrm{MAPbI_3\ slab, xFI\ terminated}) - E(\mathrm{MAPbI_3\ slab, PbI\ terminated}) - E(\mathrm{xFI}) - 3E(\mathrm{MAI})$, and for full coverage, it was calculated using

$E_b = E(\mathrm{MAPbI_3\ slab, xFI\ terminated}) - E(\mathrm{MAPbI_3\ slab, PbI\ terminated}) - 4E(\mathrm{xFI}).$

The xFI ligand-halide ion pairs have been relaxed in VASP in a 30Åx30Åx30Å box. The electrostatic potential and the dipole moment of these systems were evaluated using a TZP basis set incorporated in the Amsterdam Density Functional (ADF) program.[12] This was done using Becke's three-parameter hybrid method and the Lee-Yang-Parr's correlation functional (B3LYP).[13-14] Besides the projected density of states (pDOS) was calculated for the bare molecules without the I-H group of which the results are shown below in Figure S13.

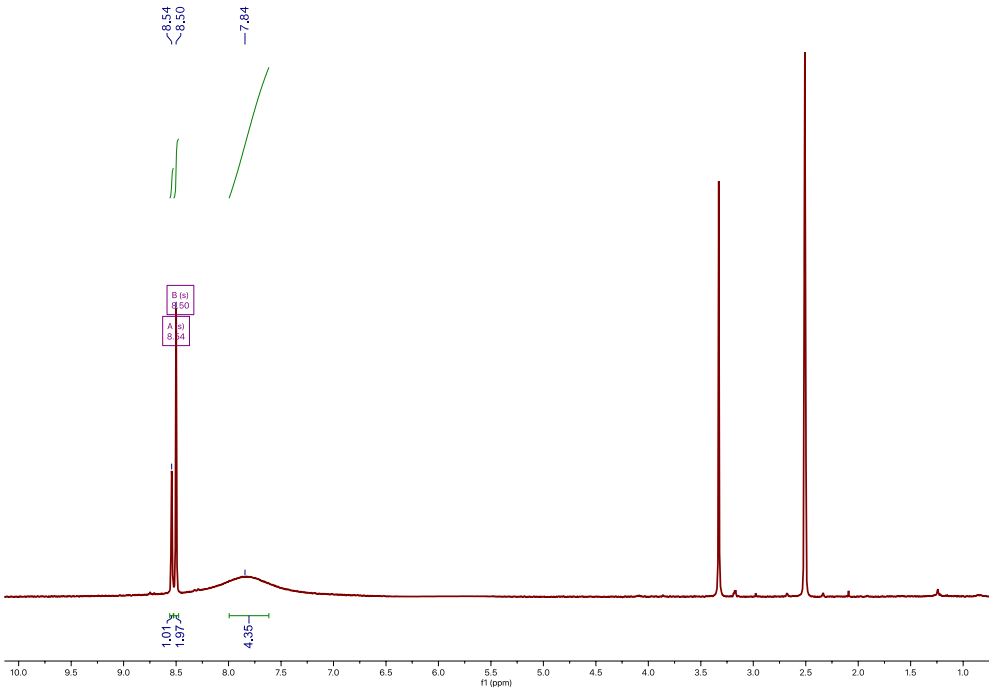

Figure S2a. ^{1}H NMR (400 MHz, DMSO-d_6, 298 K) of 2F. 3,5-difluorobenzene-1-carboximidamidium iodide (2F).

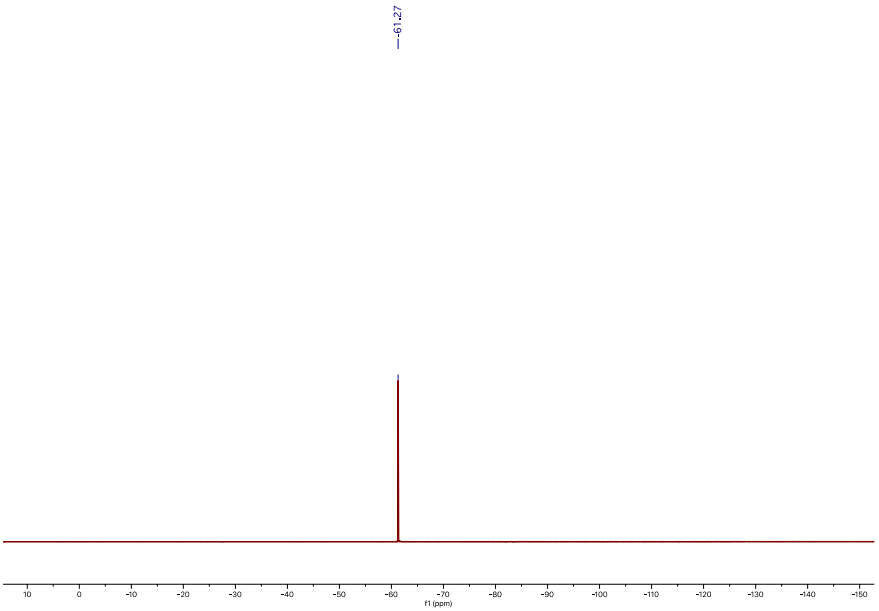

Figure S2b. ^{19}F NMR (376 MHz, DMSO-d_6, 298 K) of 2F. 3,5-difluorobenzene-1-carboximidamidium iodide (2F).

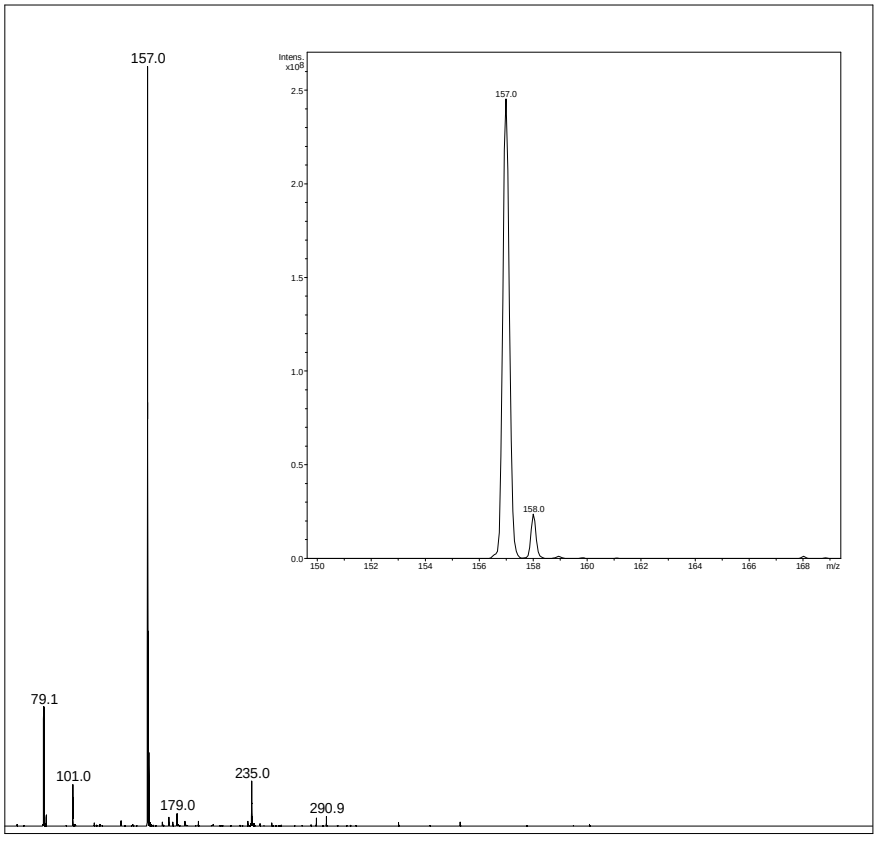

Figure S2c. MS-ESI mass spectrum of 3,5-difluorobenzene-1-carboximidamidium iodide (2F).

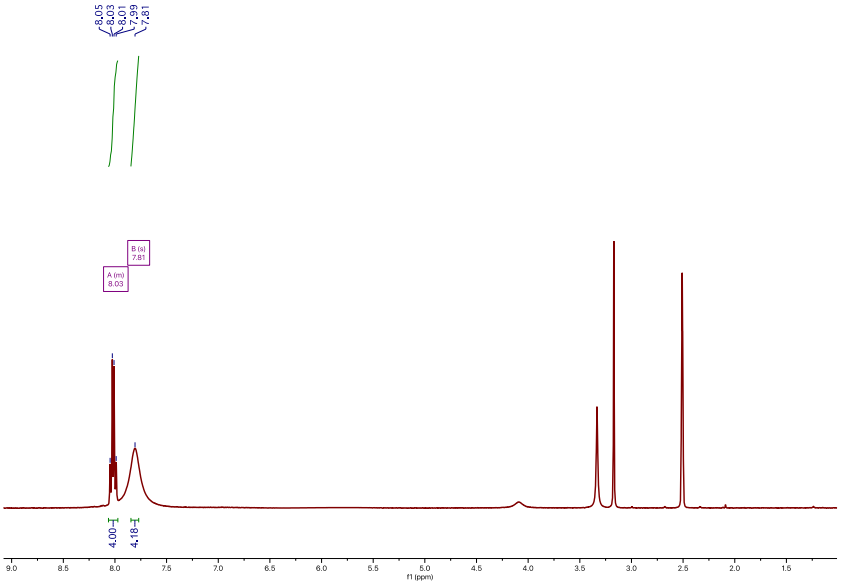

Figure S3a. [1]H NMR (400 MHz, DMSO-d_6, 298 K) of (trifluoromethyl)benzene-1-carboximidamidium iodide (3F).

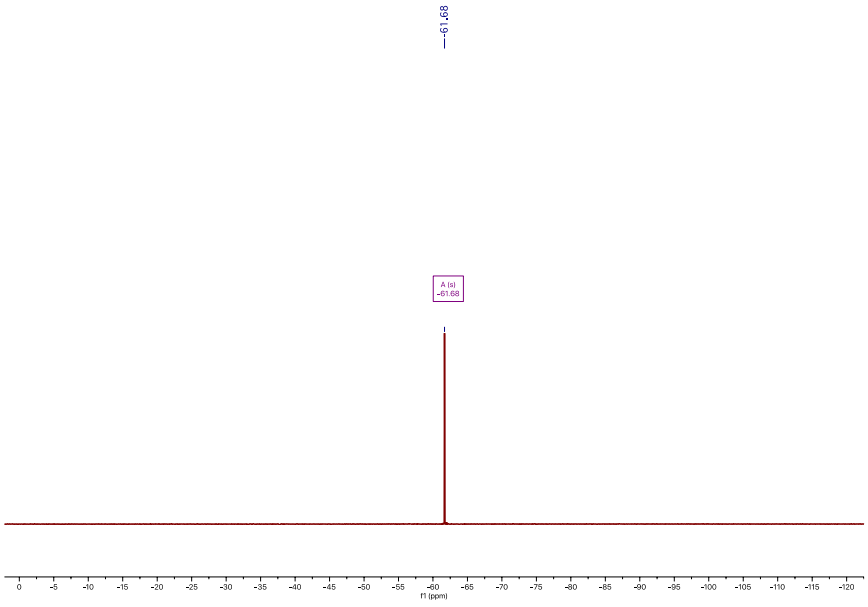

Figure S3b. [19]F NMR (376 MHz, DMSO-d_6, 298 K) of (trifluoromethyl)benzene-1-carboximidamidium iodide (3F).

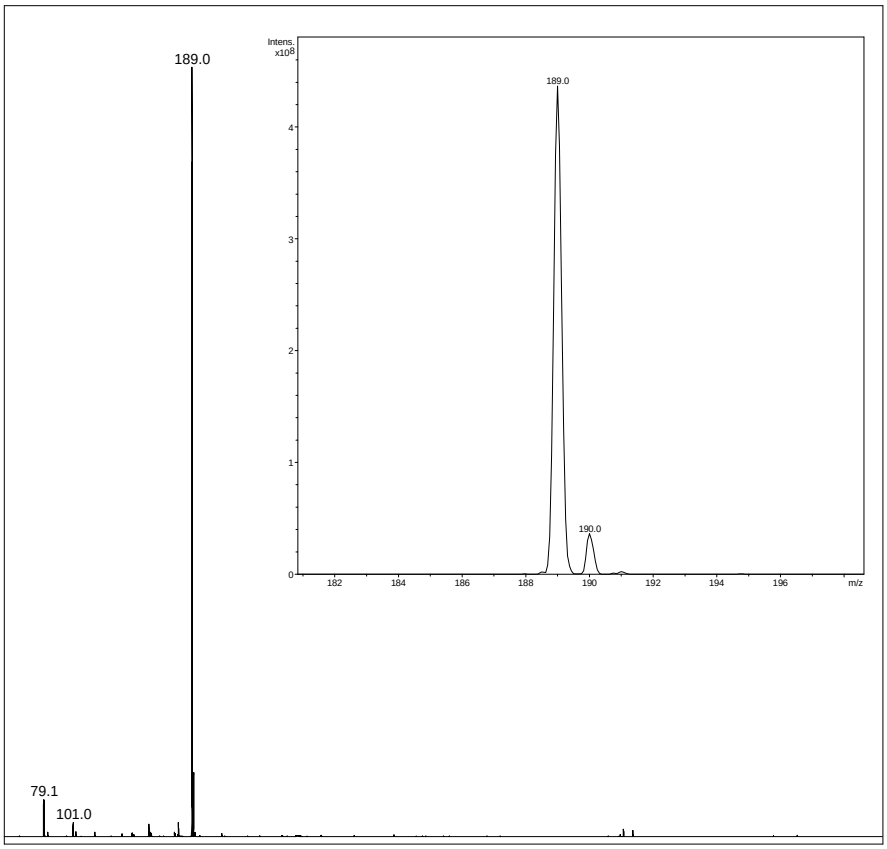

Figure S3c. MS-ESI mass spectrum of (trifluoromethyl)benzene-1-carboximidamidium iodide (3F).

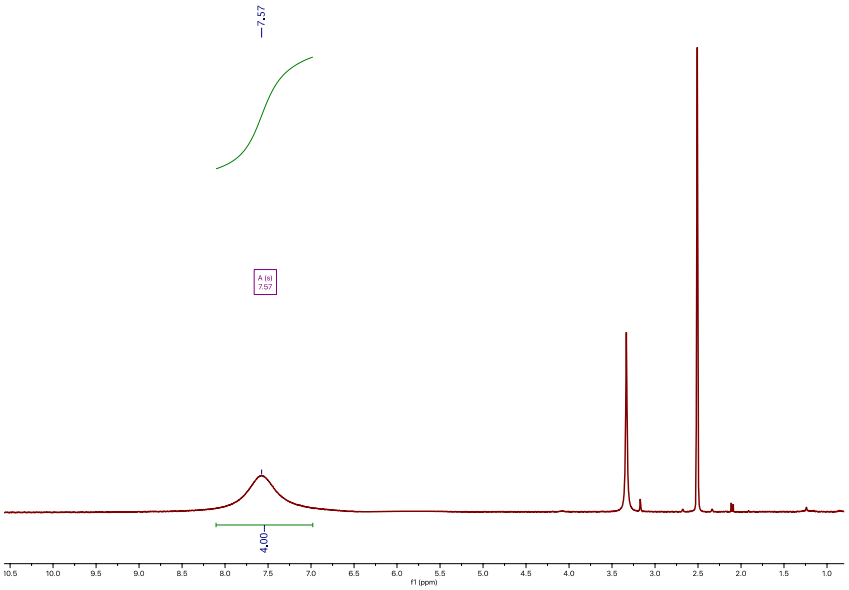

Figure S4a. ^{1}H NMR (400 MHz, DMSO-d_6, 298 K) of 2,3,4,5,6-pentafluorobenzene-1-carboximidamidium iodide (5F).

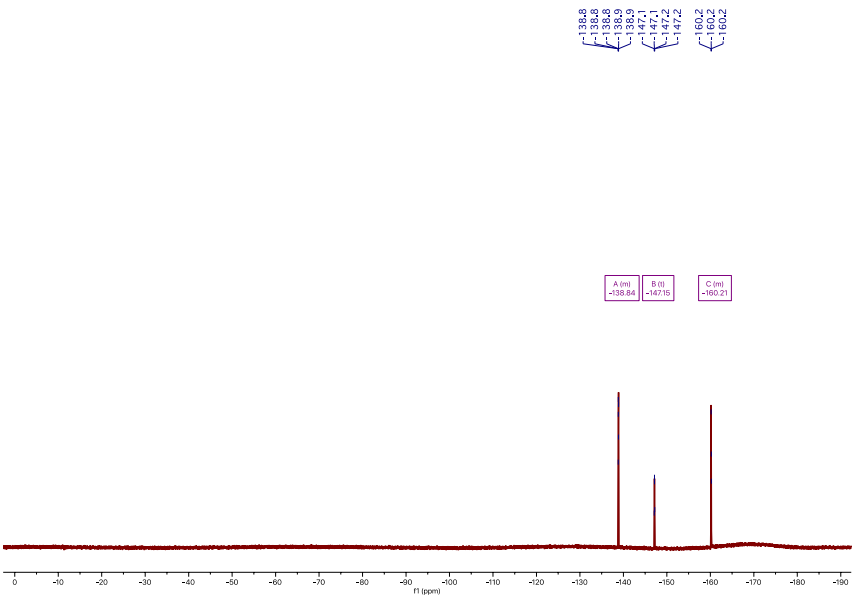

Figure S4b. ^{19}F NMR (376 MHz, DMSO-d_6, 298 K) of 2,3,4,5,6-pentafluorobenzene-1-carboximidamidium iodide (5F).

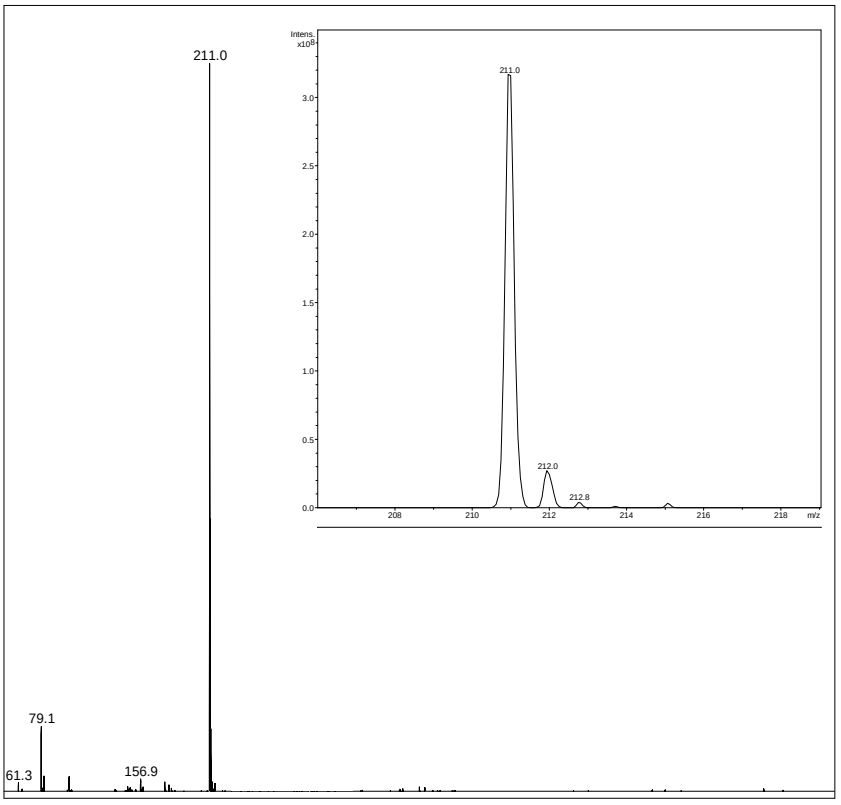

Figure S4c. MS-ESI mass spectrum of 2,3,4,5,6-pentafluorobenzene-1-carboximidamidium iodide (5F).

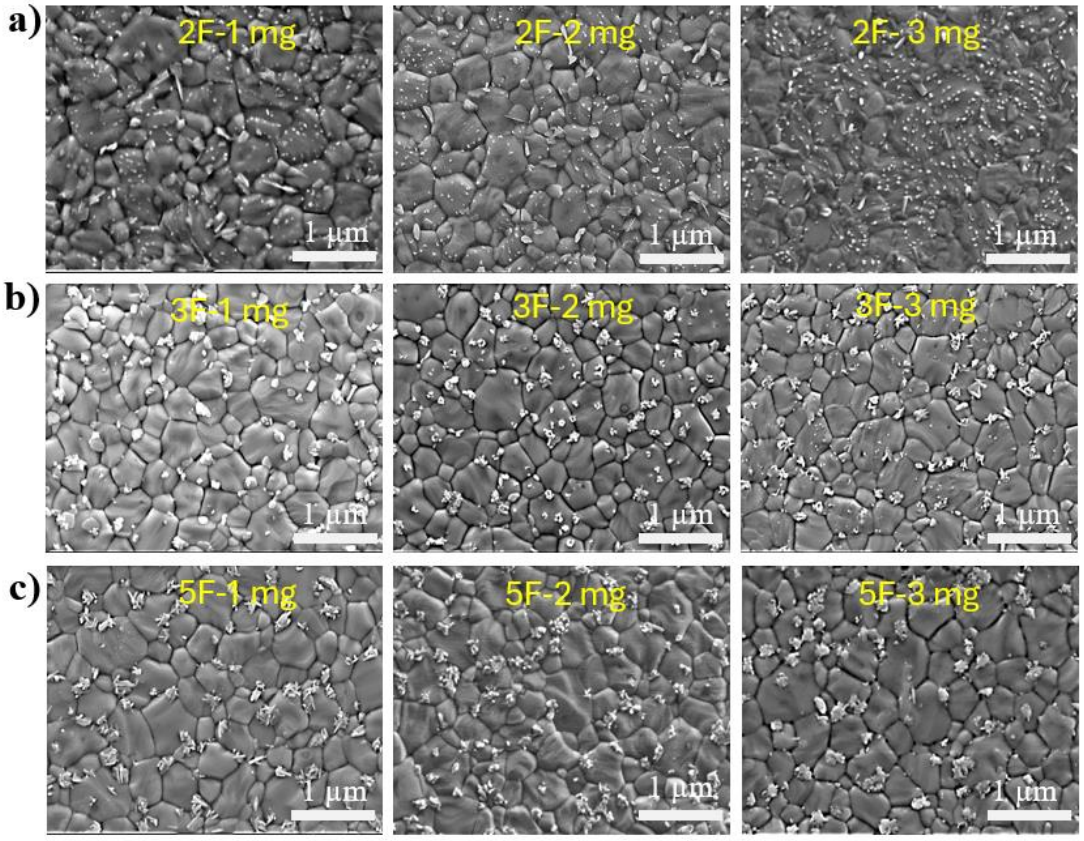

Figure S5. SEM images (SED) of a, b, c) 2F, 3F, 5F- treated 3D/LDP perovskite films.

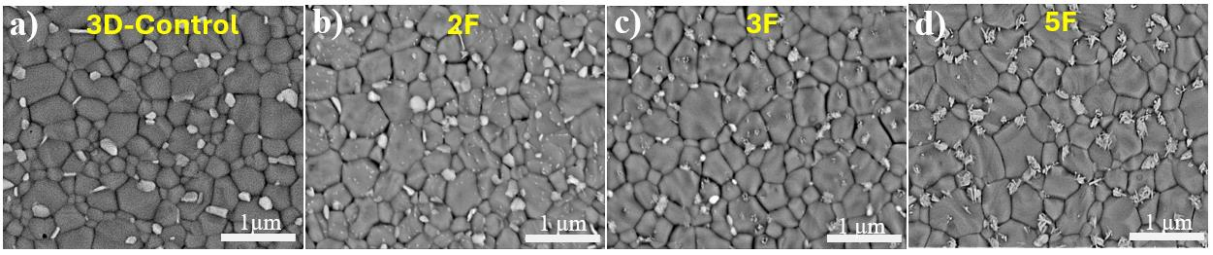

Figure S6. SEM images of a-d) 3D MAPI control film, 2F-3D/LDP, 3F-3D/LDP, and 5F-3D/LDP MAPI perovskite films were recorded using BED detectors respectively.

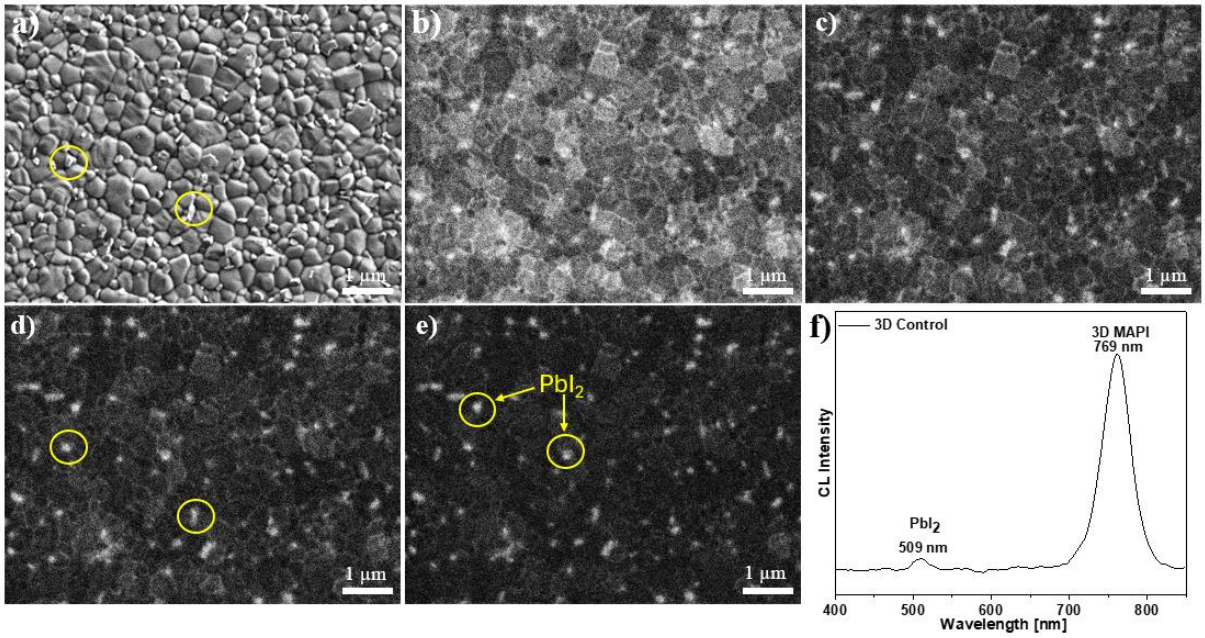

Figure S7. SEM image of 3D Control recorded using (a) SED and (b-e) CL detectors. The CL images are recorded with 2 min delay time (b = 0 min). (f) Spectrum recorded from 3D control.

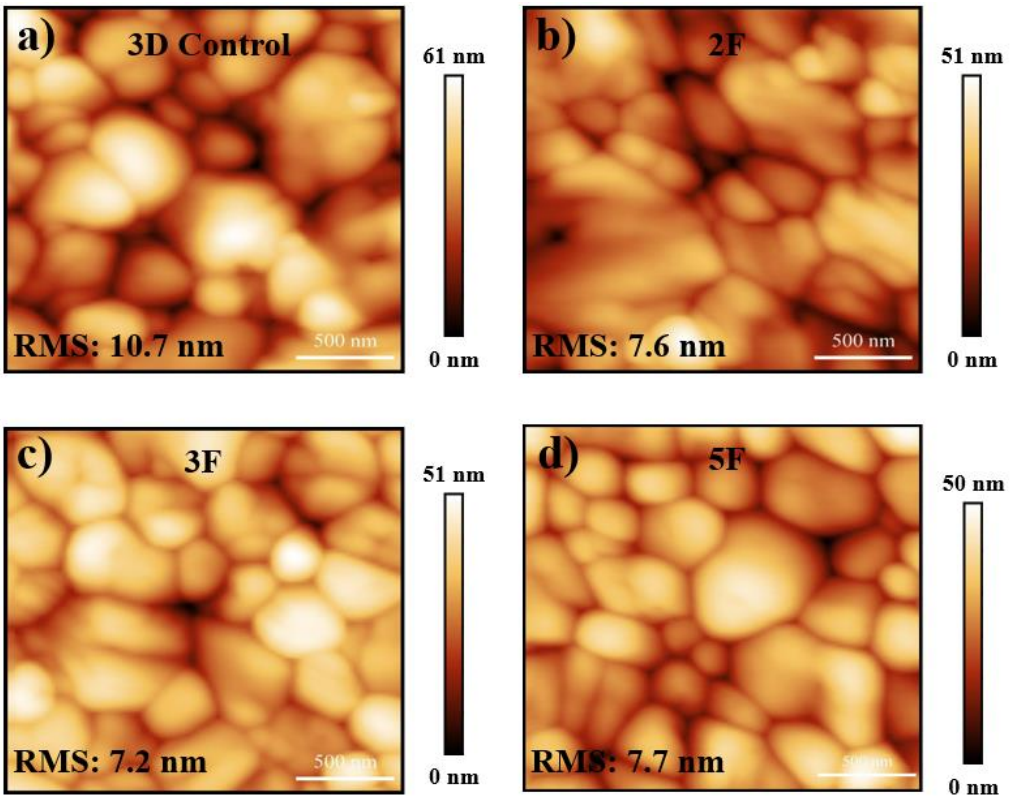

Figure S8. AFM surface morphologies and roughness (RMS values) a) 3D Control, b)2F-, c) 3F-, d) 5F- treated 3D/LDP perovskite films.

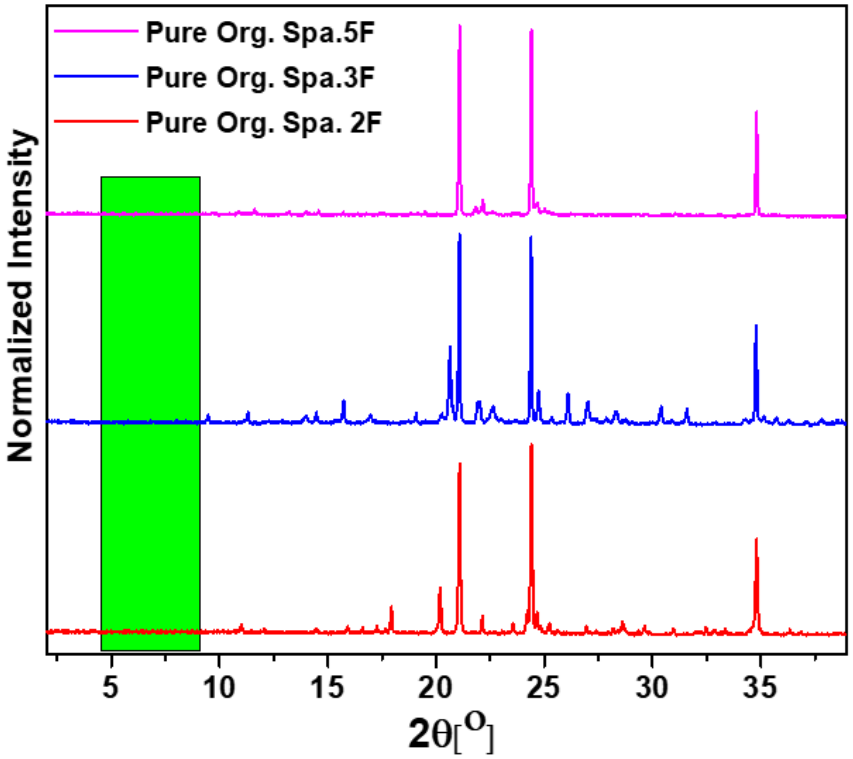

Figure S9. Powder XRD patterns of pure organic spacers 2F, 3F, 5F respectively.

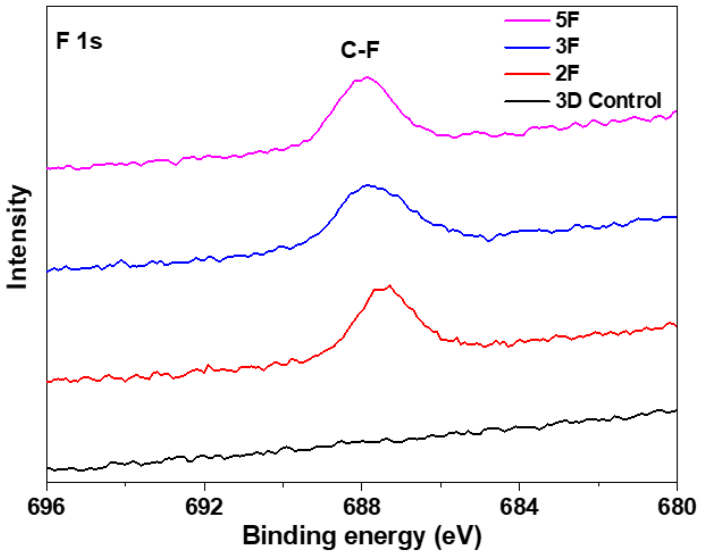

Figure S10. F1s core level XPS spectra of 3D MAPI control film, 2F-3D/LDP, 3F-3D/LDP, and 5F-3D/LDP MAPI perovskite films.

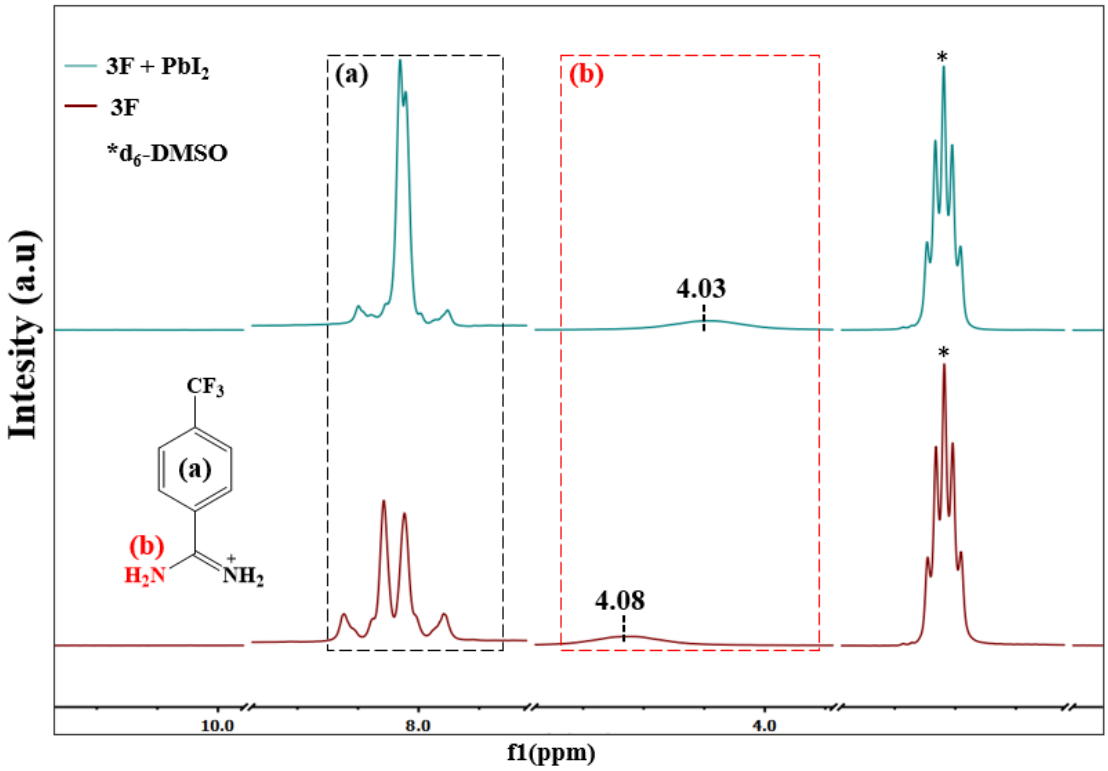

Figure S11. ^{1}H-NMR spectra of 3F organic spacer with and without PbI_2 in d_6- DMSO.

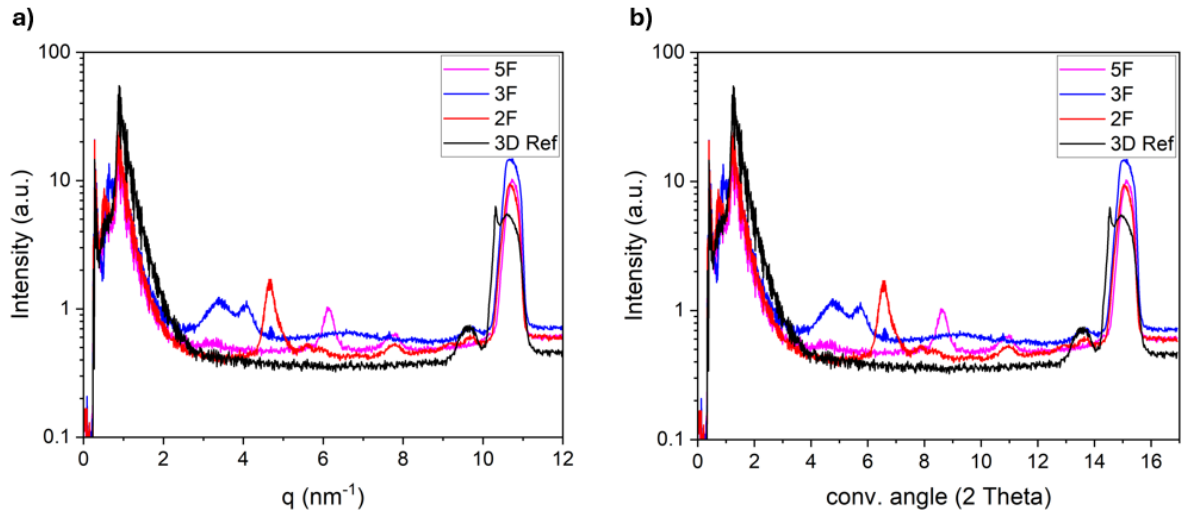

Figure S12. Pseudo-XRD data extracted by integrating the intensity 2D GIWAXS data for corresponding perovskite films in a) q space and b) angular space.

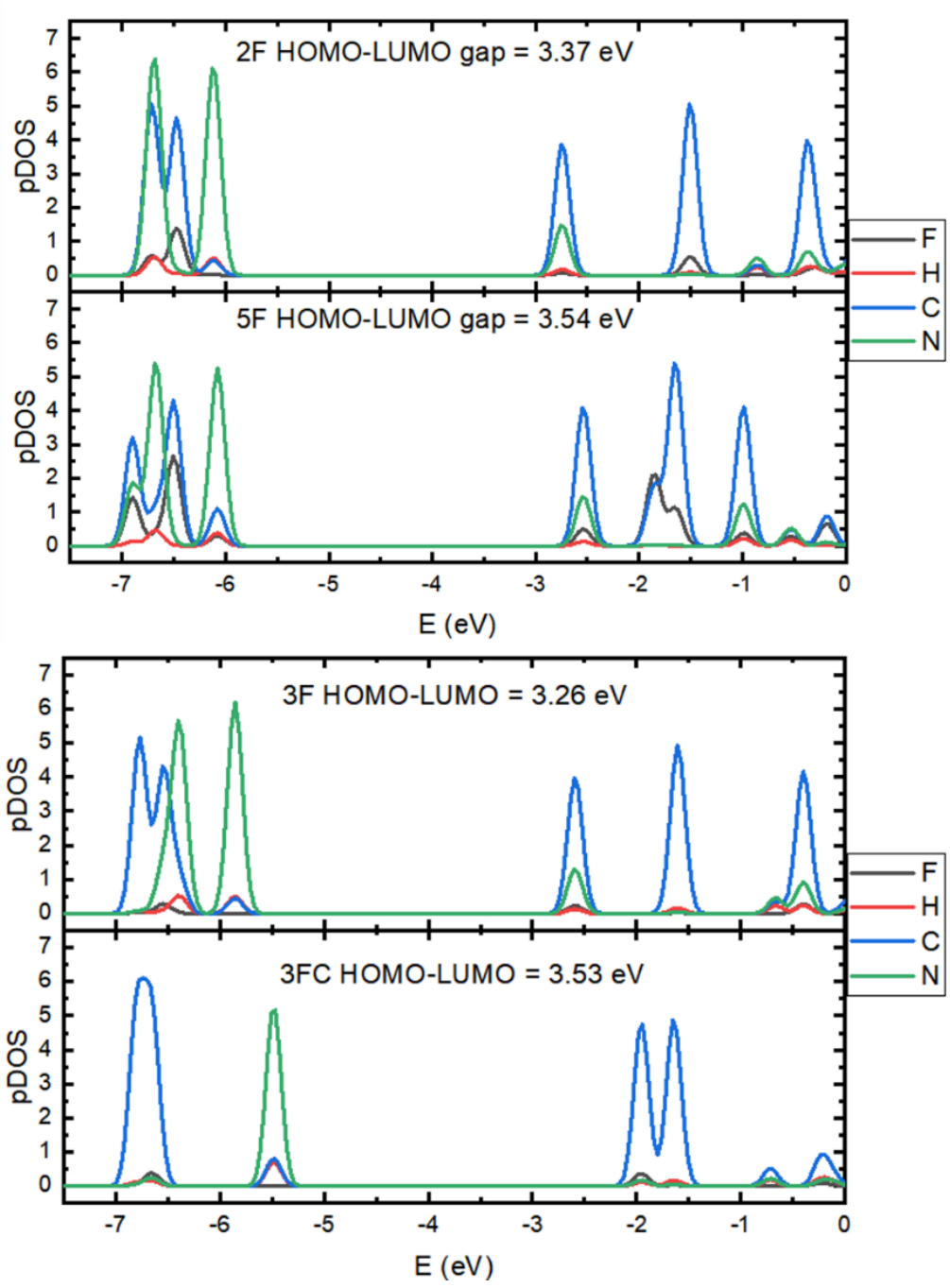

FigureS13. Projected density of states of xF molecules (2F, 3F, 5F, 3FC), calculated by DFT. The PDOS of 3F and 3FC were aligned with respect to the core levels of Pb, and the 2F and 5F are aligned with respect to the core levels of the fluorine atoms.

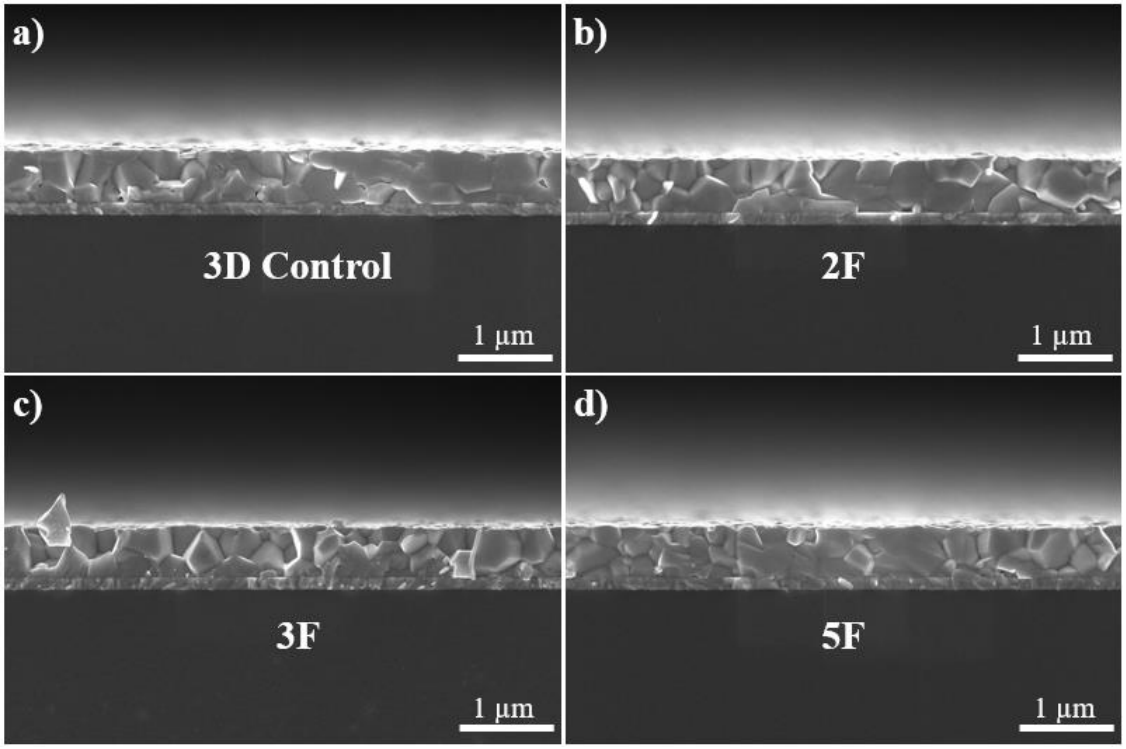

FigureS14. a-d) SEM-crossection view of the corresponding perovskite films on ITO/SnO_2.

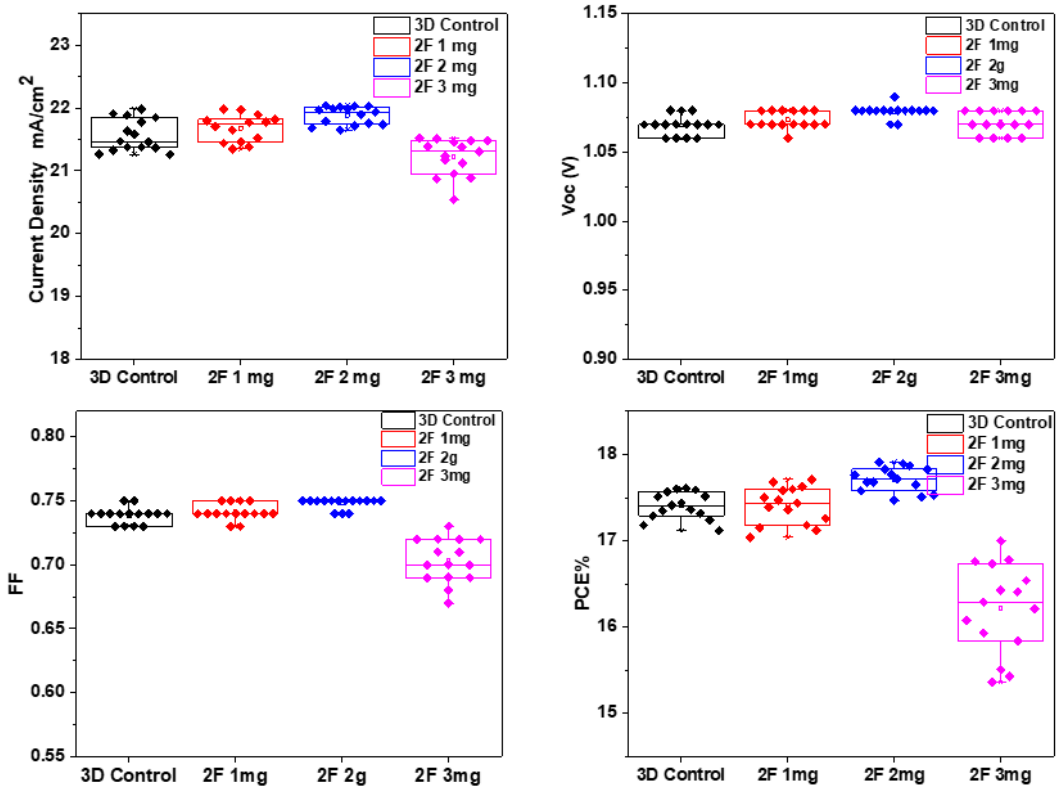

Figure S15. The statistical distribution of 3D Control and 2F-treated 3D/LDP photovoltaic parameters.

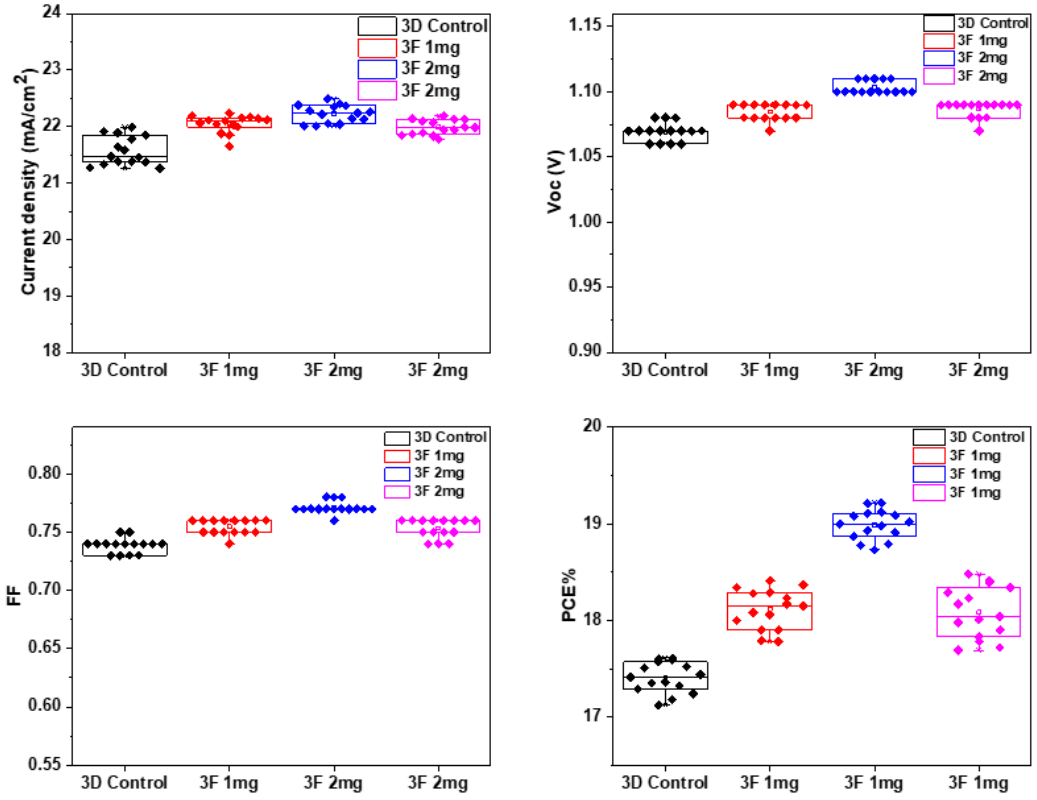

Figure S16. The statistical distribution of photovoltaic parameters of the 3D Control, 3F-treated 3D/LDP.

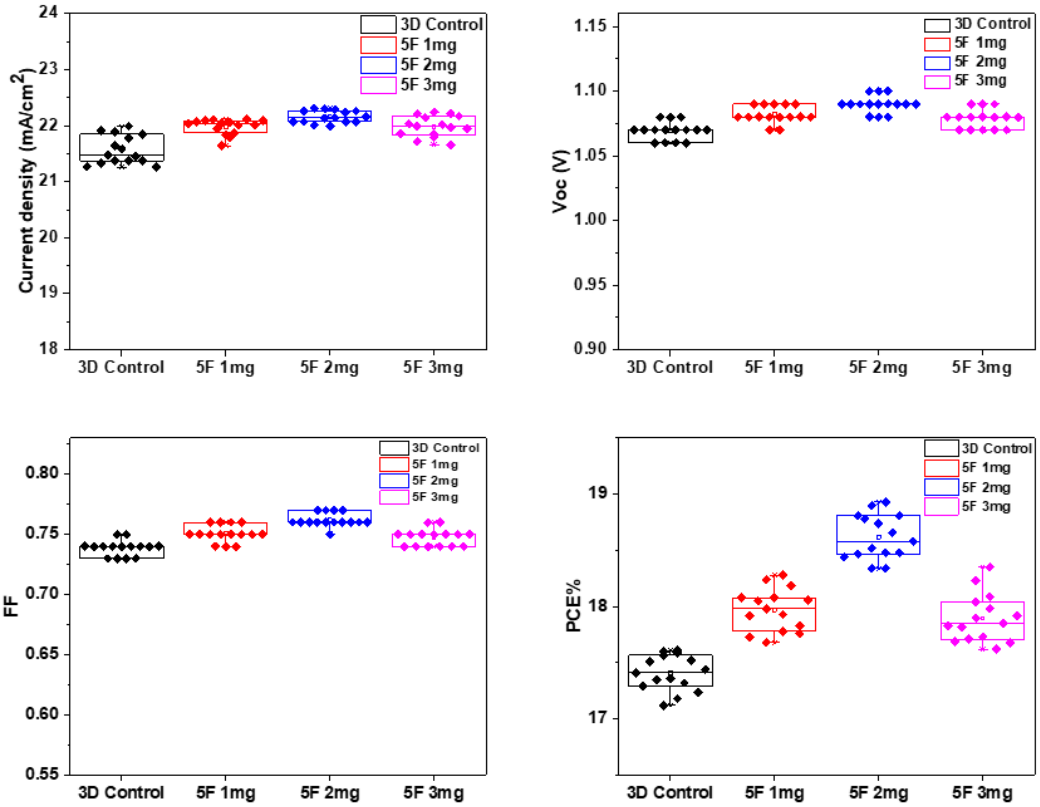

Figure S17. The statistical distribution of photovoltaic parameters of the 3D Control, 5F-treated 3D/LDP.

Table S1. Binding energies of the $Pb4f_{5/2}$, $Pb4f_{7/2}$, $I3d_{3/2}$ and $I3d_{5/2}$ orbitals of corresponding perovskite films.

Sample	$Pb_{5f/2}$ (eV)	$Pb_{7f/2}$ (eV)	$I_{3d/2}$ (eV)	$I_{5d/2}$ (eV)
3D MAPI Control	**143**	**138.2**	**630.6**	**619.1**
2F	**142.7**	**137.9**	**630.3**	**618.8**
3F	**142.6**	**137.8**	**630.1**	**618.6**
5F	**142.7**	**137.9**	**630.2**	**618.7**

Table S2. Time-resolved photoluminescence decay components of 3D MAPI reference, and treated 3D/LDP perovskite films.

Sample	A_1(%)	τ_1 (µs)	A_2 (%)	τ_2 (µs)	$\tau_{ave.}$ (µs)
3D MAPI Control	**57.92**	**0.049**	**42.08**	**0.112**	**0.075**
2F	**48.16**	**0.052**	**51.84**	**0.142**	**0.088**
3F	**38.48**	**0.057**	**61.52**	**0.213**	**0.156**
5F	**39.09**	**0.061**	**60.91**	**0.190**	**0.140**

Table S3. PV parameters for the champion devices. The values obtained from the reverse scan are indicated within parenthesis.

Device	J_{sc} (mA\cm^2)	PCE %	V_{oc} (V)	FF	Integrated Photocurrent (mA\cm^2)	Hysteresis Index %
3D Control	**21.99(21.52)**	**17.61(16.52)**	**1.07(1.06)**	**0.74(0.72)**	**20.94 (J_{sc} -4.77%)**	**6.2**
2F	**22.03(21.72)**	**17.91(17.00)**	**1.08(1.07)**	**0.75(0.73)**	**21.03 (J_{sc} -4.53%)**	**5.1**
3F	**22.34(22.19)**	**19.22(19.05)**	**1.10(1.09)**	**0.77(0.77)**	**21.44 (J_{sc}-4.45%)**	**0.9**
5F	**22.13(22.05)**	**18.93(18.65)**	**1.09(1.08)**	**0.76(0.76)**	**21.23 (J_{sc}-4.10 %)**	**1.5**

4.5 REFERENCES

[1] S. Akin, N. Arora, S. M. Zakeeruddin, M. Grätzel, R. H. Friend, M. I. Dar, *Adv. Energy Mater.* **2019**, *10*, 1903090.

[2] T. Yang, C. Ma, W. Cai, S. Wang, Y. Wu, J. Feng, N. Wu, H. Li, W. Huang, Z. Ding, L. Gao, S.F. Liu, K. Zhao, *Joule* **2023**, *7*, 574.

[3] W. Xiang, Z. Wang, D. J. Kubicki, W. Tress, J. Luo, D. Prochowicz, S. Akin, L. Emsley, J. Zhou, G. Dietler, M. Grätzel, A., Hagfeldt, *Joule* **2019**, *3*, 205.

[4] A. Kojima, K. Teshima, Y. Shirai, T. Miyasaka, *J. Am. Chem. Soc.* **2009**, *131*, 6050.

[5] J. Park, J. Kim, H. S. Yun, M. J. Paik, E. Noh, H. J. Mun, M.G. Kim, T.J. Shin, S. I. Seok, *Nature* **2023,** *616*, 724.

[6] H. J. Snaith, *J. Phys. Chem. Lett.* **2013**, *4*, 3623.

[7] S. D. Stranks, G. E. Eperon, G. Grancini, C. Menelaou, M. J. P. Alcocer, T. Leijtens, L. M. Herz, A. Petrozza, H. J. Snaith, *Science* **2013**, *342*, 341.

[8] W. Nie, H. Tsai, R. Asadpour, J.-C. J. C. Blancon, A. J. Neukirch, G. Gupta, J. J. J. Crochet, M. Chhowalla, S. Tretiak, M. A. Alam, H. L. H.-L. Wang, A. D. Mohite, *Science* **2015**, *347*, 522.

[9] G. E. Eperon, M. T. Horantner, H. J. Snaith, *Nat. Rev. Chem.* **2017**, *1*, 0095.

[10] S. Albrecht, M. Saliba, J. P. C. Baena, F. Lang, L. Kegelmann, M. Mews, L. Steier, A. Abate, J. Rappich, L. Korte, *Energy Environ.Sci.* **2016**, *9*, 81.

[11] Z. Wang, Z. J. Shi, T. T. Li, Y. H. Chen, W. Huang, *Angew. Chem., Int. Ed.* **2017**, *56*, 1190.

[12] S. Yang, Y. Wang, P. Liu, Y.-B. Cheng, H. J. Zhao, H. G. Yang, *Nat. Energy* **2016**, *1*, 15016.

[13] P. Li, C. Liang, X.- L. Liu, F. Li, Y. Zhang, X.- T. Liu, H. Gu, X. Hu, G. Xing, X. Tao, Y. Song, *Adv. Mater.* **2019**, *31*, 1901966.

[14] Y. Rong, L. Liu, A. Mei, X. Li, H. Han, *Adv. Energy Mater.* **2015**, *5*, 1501066.

[15] B. Chen, P. N. Rudd, S. Yang, Y. Yuan, J. Huang, *Chem. Soc. Rev.* **2019**, *48*, 3842.

[16] Q. Zhou, Y. Gao, C. Cai, Z. Zhang, J. Xu, Z. Yuan, P. Gao, *Angew. Chem., Int. Ed.* **2021**, 60, 8303.

[17] E. Akman, S. Akin, *Adv. Mater.* **2021**, *33*, 2006087.

[18] D. Shi, V. Adinolfi, R. Comin, M. Yuan, E. Alarousu, A. Buin, Y. Chen, S. Hoogland, A. Rothenberger, K. Katsiev, Y. Losovyj, X. Zhang, P. A. Dowben, O. F. Mohammed, E. H. Sargent, O. M. Bakr, *Science* **2015**, *347*, 519.

[19] Q. Wang, B. Chen, Y. Liu, Y. Deng, Y. Bai, Q. Dong, J. Huang, *Energy Environ. Sci.* **2017**, *10*, 516.

[20] S. G. Motti, D. Meggiolaro, A. J. Barker, E. Mosconi, C. A. R. Perini, J. M. Ball, M. Gadini, M. Kim, F. De Angelis, A. Petrozza, *Nat. Photon.* **2019**, *13*, 532.

[21] N. Ahn, K. Kwak, M.S. Jang, H. Yoon, B. Y. Lee, J-K. Lee, P. V. Pikhitsa, J. Byun, M. Choi, *Nat. Commun.* **2016**, *7*, 13422.

[22] K. Kwak, E. Lim, N. Ahn, J. Heo, K. Banh, S. K. Kim, M. Choi, *Nanoscale* **2019**, *11*, 11369.

[23] C. Li, S. Tscheuschner, F. Paulus, P. E. Hopkinson, J. Kießling, A. Köhler, Y. Vaynzof, S. Huettner, *Adv. Mater*. **2016**, 28, 2446.

[24] G. J. A. H. Wetzelaer, M. Scheepers, A. M. Sempere, C. Momblona, J. Avila, H. J. Bolink, *Adv. Mater.* **2015**, *27*, 1837.

[25] C. Eames, J. M. Frost, P. R. F. Barnes, B.C. O'Regan, A. Walsch, M. S. Islam, *Nat. Commun.* **2015**, *6*, 7497.

[26] J. M. Azpiroz, E. Mosconi, J. Bisquert, F. D. Angelis, Energy *Environ. Sci.* **2015**, *8*, 2118.

[27] N. Li, S. Tao, Y. Chen, X. Niu, C. K. Onwudinanti, C. Hu, Z. Qiu, Z. Xu, G. Zheng, L. Wang, Y. Zhang, L. Li, H. Liu, Y. Lun, J. Hong, X. Wang, Y. Liu, H. Xie, Y. Gao, Y. Bai, S. Yang, G. Brocks, Q. Chen, H. Zao, *Nat. Energy* **2019**, *4*, 408.

[28] G. Ren, W. Han, Y. Deng, W. Wu, Z. Li, J. Guo, H. Bao, C. Liu, W. Guo, *J. Mater. Chem. A* **2021**, *9*, 4589.

[29] T. Wu, Z. Qin, Y. Wang, Y. Wu, W. Chen, S. Zhang, M. Cai, S. Dai, J. Zhang, J. Liu, Z. Zou, X. Liu, H. Segawa, H. Tan, Q. Tang, J. Fang, Y. Li, L. Ding, Z. Ning, Y. Qi, Y. Zhang, L. Han, *Nano-Micro Lett.* **2021**, *13*, 152.

[30] D. Xin, S. Tie, R. Yuan, X. Zheng, J. Zhu, W. H. Zhang, *ACS Appl. Mater. Interfaces* **2019**, *11*, 44233.

[31] T. Wu, X. Li, Y. Qi, Y. Zhang, L. Han, *Chem.Sus.Chem*. **2021**, *14*, 4354.

[32] Y. Liu, S. Akin, A. Hinderhofer, F. T. Eickemeyer, H. Zhu, J.-Y. Seo, J. Zhang, F. Schreiber, H. Zhang, M. Zakeeruddin, A. Hagfeldt, M. I. Dar, M. Grätzel, *Angew. Chem., Int. Ed.* **2020**, *59*, 15688.

[33] E. Khorshidi, B. Rezaei, D. Blätte, A. Buyruk, M. A. Reus, J. Hanisch, B. Böller, P. Müller-Buschbaum, T. Ameri, *Sol. RRL* **2022**, *6*, 2200023.

[34] E. Khorshidi, B. Rezaei, J. Hanisch, B. Böller, M. A. Reus, P. Müller-Buschbaumde, T. Ameri, *ACS Appl. Mater. Interfaces* **2022,** *14*, 54623.

[35] L. Meng, J. You, Y. Yang, *Nat. Commun.* **2018**, *9*, 5265.

[36] A. Semerci, A. Buyruk, S. Emin, R. Hooijer, D. Kovacheva, D. Mayer, M.A. Reus, D. Blätte, M. Günther, N. F. Hartmann, S. Lotfi, J. P. Hofmann, P. M. Buschbaum, T. Bein, T. Ameri, *Adv. Opt. Mater.* **2023**, *11*, 2300267.

[37] A. Buyruk, D. Blätte, M. Günther, M. A. Scheel, N. F. Hartmann, M. Döblinger, A. Weis, A. Hartschuh, P. Müller-Buschbaum, T. Bein, T. Ameri, *ACS Appl. Mater. Interfaces* **2021**, *13*, 32894.

[38] J. Zhang, X. Yang, H. Deng, K. Qiao, U. Farooq, M. Ishaq, F. Yei, H. Liu, J. Tang, H. Song., *Nano-Micro Lett.* **2017**, *9*, 1.

[39] M. Shao, T. Bie, L. Yang, Y. Gao, X. Jin, F. He, N. Zheng, Y. Yu, X. Zhang, *Adv. Mater.* **2022**, *34*, 2107211.

[40] B. Saparov, D. B. Mitzi, *Chem. Rev.* **2016**, *116*, 4558.

[41] P. Chen, Y. Bai, S. Wang, M. Lyu, J. Yun, L. Wang, *Adv. Funct. Mater.* **2018**, *28*, 1706923.

[42] I. C. Smith, E. T. Hoke, D. Solis-Ibarra, M. D. McGehee, H. I. Karunadasa, *Angew. Chem., Int. Ed.* **2014**, *53*, 11232.

[43] T. D. Gangadharan, D. Ma, *Energy Environ. Sci.* **2019**, *12*, 2860.

[44] C. Katan, N. Mercier, J. Even, *Chem. Rev.* **2019**, *119*, 3140.

[45] R. Hooijer, A. Weis, A. Biewald, M. T. Sirtl, J. Malburg, R. Holfeuer, S. Thamm, A. A. Y. Amin, M. Righetto, A. Hartschuh, L. M. Herz, T. Bein, *Adv. Opt. Mater*. **2022**, *10*, 2200354.

[46] J. S. Shi, Y. R. Gao, X. Gao, Y. Zhang, J. J. Zhang, X. Jing, M. Shao, *Adv. Mater.* **2019**, *31*, 1901673.

[47] Q. Zhou, Q. Xiong, Z. Zhang, J. Hu, F. Lin, L. Liang, T. Wu, X. Wang, J. Wu, B. Zhang, P. Gao, *Sol. RRL* **2020**, *4*, 2000107.

[48] F. Zhang, D. H. Kim, H. Lu, J. S. Park, B. W. Larson, J. Hu, L. Gao, C. Xiao, O. G. Reid, X. Chen, Q. Zhao, P. F. Ndione, J. J. Berry, W. You, A. Walsh, M. C. Beard, K. Zhu, *J.Am.Chem. Soc.* **2019**, *141*, 5972.

[49] Y. Wei, P. Audebert, L. Galmiche, J. S. Lauret, E. Deleporte, J. *Phys. D. Appl. Phys*. **2013**, *46*, 135105.

[50] Y. Liu, S. Akin, L. Pan, R. Uchida, N. Arora, J. V. Milić, A. Hinderhofer, F. Schreiber, A. R. Uhl, S. M. Zakeeruddin, A. Hagfeldt, M. I. Dar, M. Grätzel *Sci. Adv.* **2019**, *5*, eaaw2543.

[51] J. Zhou, M. Li, S. Wang, L. Tan, Y. Liu, C. Jiang, X. Zhao, L. Ding, C. Yi, *Nano Energy* **2022,** *95*, 107036.

[52] H. Zhu, Y. Ren, L. Pan, O. Ouellette, F. T. Eickemeyer, Y. Wu, X. Li, S. Wang, H. Liu, X. Dong, S. M. Zakeeruddin, Y. Liu, A. Hagfeldt, M. Grätzel, *J.Am.Chem. Soc.* **2021**, *143*, 3231.

[53] D. Li, Z. Xing, L. Huang, X. Meng, X. Hu, T. Hu, Y. Chen, *Adv.Mater.* **2021**, *33*, 2101823.

[54] X. Lai, W. Li, X. Gu, H. Chen, Y. Zhang, G. Li, R. Zhang, D. Fan, F. He, N. Zheng, J. Yu, R. Chen, A. K.K. Kyaw, X. W. Sun, *J. Chem. Eng.* **2022**, *427*, 130949.

[55] W. Shi, H. Ye, J.*Phys.Chem.Lett.* **2021,** *12*, 4052.

[56] T. Zhou, H. Lai, T. Liu, D. Lu, X. Wan, X. Zhang, Y. Liu, Y. Chen, *Adv. Mater.* **2019**, *31*, 1901242.

[57] A. Amat, E. Mosconi, E. Ronca, C. Quarti, P. Umari, M. K. Nazeeruddin, M. Grätzel, F. De Angelis, *Nano Lett.* **2014**, *14*, 3608.

[58] J. W. Xiao, L. Liu, D. Zhang, N. De Marco, J. W. Lee, O. Lin, Q. Chen, Y. Yang, *Adv. Energy Mater.* **2017**, 7, 1700491.

[59] Y. Dong, D. Lu, Z. Xu, H. Lai, Y. Liu, *Adv. Energy Mater.* **2020**, *10*,2000694.

[60] Q. Li, Y. Dong, G. Lv, T. Liu, D. Lu, N. Zheng, X. Dong, Z. Xu, Z. Xie, Y. Liu, *ACS Energy Lett.* **2021**, *6*, 2072.

[61] J. S. Shi, Y. R. Gao, X. Gao, Y. Zhang, J. J. Zhang, X. Jing, M. Shao, *Adv. Mater.* **2019**, *31*, 1901673.

[62] J. Hu, I. W. H. Oswald, H. Hu, S. J. Stuard, M. M. Nahid, L. Yan, Z. Chen, H. Ade, J. R. Neilson, W. You, Acs *Mater. Lett.* **2019**, *1*, 171.

[63] Z. Ren, X. Xiao, R. Ma, H. Lin, K. Wang, X. W. Sun, W. C. H. Choy, *Adv. Funct. Mater.* **2019**, *29*, 1905339.

[64] C. Xiao, Z. Li, H. Guthrey, J. Moseley, Y. Yang, S. Wozny, H. Moutinho, B. To, J. J. Berry, B. Gorman, *J. Phys. Chem. C* **2015**, *119*, 26904.

[65] Q. Li, Y. Dong, G. Lv, T. Liu, D. Lu, N. Zheng, X. Dong, Z. Xu, Z. Xie, Y. Liu, *ACS Energy Lett.* **2021**, *6*, 2072.

[66] R. Lin, J. Xu, M. Wei, Y. Wang, Z. Qin, Z. Liu, J. Wu, K. Xiao, B. Chen, S. M. Park, G. Chen, H. R. Atapattu, K. R. Graham, J. Xu, J. Zhu, L. Li, C. Zhang, E. H. Sargent, H. Tan, *Nature* **2022**, *603*, 73.

[67] P. Chen, Y. Bai, S. Wang, M. Lyu, J. H. Yun, L. Wang, *Adv. Funct. Mater.* **2018,** *28*, 1706923.

[68] J. Shi, Y. Gao, X. Gao, Y. Zhang, J. Zhang, X. Jing, M. Shao, *Adv. Mater.* **2019**, *31*, 1901673.

[69] T. Liu, J. Guo, D. Lu, Z. Xu, Q. Fu, N. Zheng, Z. Xie, X. Wan, X. Zhang, Y. Liu, Y. Chen, *ACS Nano*, **2021**, *15*, 7811.

[70] W. S. Yang, B. W. Park, E. H. Jung, N. J. Jeon, Y. C. Kim, D. U. Lee, S. S. Shin, J. Seo, E. K. Kim, J. H. Noh, S. il Seok, *Science* **2017**, *356*, 1376.

[71] M. H. Li, H. H. Yeh, Y. H. Chiang, U. S. Jeng, C. J. Su, H. W. Shiu, Y. J. Hsu, N. Kosugi, T. Ohigashi, Y. A. Chen, P. S. Shen, P. Chen, T. F. Guo, *Adv. Mater.* **2018**, *30*, 1801401.

[72] J. W. Lee, Z. Dai, T. H. Han, C. Choi, S. Y. Chang, S. J. Lee, N. De Marco, H. Zhao, P. Sun, Y. Huang, Y. Yang, *Nat. Commun.* **2018**, *9*, 3021.

[73] W. J. Wei, X. X. Jiang, L. Y. Dong, W. W. Liu, X. B. Han, Y. Qin, K. Li, W. Li, Z. S. Lin, X. H. Bu, P. X. Lu, *J. Am. Chem. Soc.* **2019**, *141*, 9134.

[74] Q. Li, Y. Dong, G. Lv, T. Liu, D. Lu, N. Zheng, X. Dong, Z. Xu, Z. Xie, Y. Liu, *ACS Energy Lett.* **2021**, *6*, 2072.

[75] J. Byeon, S. H. Cho, J. J. Jang, C. Katan, J. Even, J. Xi, M. Choi, Y. S. Lee, *ACS Appl. Mater. Interfaces* **2023**, *15*, 27853.

[76] H. N. Si, Q. L. Liao, Z. Kang, Y. Ou, J. J. Meng, Y. C. Liu, Z. Zhang, Y. Zhang, *Adv. Funct. Mater.* **2017**, *27*, 1701804.

[77] T. J. Jacobsson, J. P. Correa-Baena, E. Halvani Anaraki, B. Philippe, S. D. Stranks, M. E. F. Bouduban, W. Tress, K. Schenk, J. Teuscher, J. E. Moser, H. Rensmo, A. Hagfeldt, *J. Am. Chem. Soc.* **2016**, *138*, 10331.

[78] D. Q. Bi, W. Tress, M. I. Dar, P. Gao, J. Luo, C. Renevier, K. Schenk, A. Abate, F. Gıordano, J-P. C. Baena, J-D. Decoppet, S. M. Zakeeruddin, M. Grätzel, A. Hagfeldt, *Sci. Adv.* **2016,** *2*, e1501170.

[79] X. Zhang, X. Ren, B. Liu, R. Munir, X. Zhu, D. Yang, J. Li, Y. Liu, D-M. Smilgies, R. Li, Z. Yang, T. Niu, X. Wang, A. Amassian, K. Zhao, S. F. Liu, *Energy Environ. Sci.* **2017**, *10*, 2095.

[80] S. Akin, M. Bauer, D. Hertel, K. Meerholz, S. M. Zakeeruddin, M. Graetzel, P. Bäuerle, M. I. Dar, *Adv. Funct. Mater.* **2022**, *32*, 2205729.

[81] R. S. Garigipiati, *Tetrahedron Lett.* **1990**, *31*, 1969.

[82] M. Zhao, W. Guo, L. Wu, F. G. Qiu, *Chemistry Select* **2022**, *7*, e20220372.

[83] S. Oh, R. P. Bisbey, S. Gul, J. Yano, G. L. Fisher, Y. Surendranath, Chem. Mater. **2020**, 32, 8512.

[84] Z. Zhang, A. Huang, L. Ma, J.-H. Xub, M. Zhang, *RSC Adv.* **2022**, *12*, 15190.

[85] J. B. Medwid, R. Paul, J. S. Baker, J. A. Brockman, M. T. Du, W. A. Hallett, J. W. Hanifin, R. A. Hardy, M. E. Tarrant, W. Torley, S. Wrenn, *J. Med. Chem.* **1990**, *33*, 1230.

[86] G. Kresse, J. Hafner, *Phys. Rev. B* **1993,** *47*,558.

[87] G. Kresse, J. Furthmüller, *Comput. Mater. Sci*.**1996,** *6*, 15.

[88] G. Kresse, J. Furthmüller, *Phys. Rev. B* **1996,** *54*,11169.

[89] J. P. Perdew, K. Burke, M. Ernzerhof, *Phys. Rev. Lett.* **1996**, *77*, 3865.

[90] S. Grimme, J. Antony, S. Ehrlich, H. A. Krieg, *J. Chem. Phys.***2010**, *132*, 154104.

[91] H. J. Monkhorst, J. D. Pack, *Phys. Rev. B*, **1976**, *13*, 5188.

[92] G. te Velde, F. M. Bickelhaupt, E. J. Baerends, C. Fonseca Guerra, S. J. A. van Gisbergen, J. G. Snijders, T. Ziegler, *J. Chem. Phys.* **2001**, *22*, 931.

[93] A. D. Becke, *J. Chem. Phys.* **1993**, *98*, 5648.

[94] C. Lee, W. Yang, R. G. Parr, *Phys. Rev. B* **1988,** *37,*785.

5. CONCLUSION

In this thesis, we focused on doing extensive study on the defects that appear at the surfaces, grain boundaries and bulk structure of polycrystalline lead-based 3D MAPI perovskite materials. These defects have a significant negative impact on the performance and long-term stability of PV devices made with these materials. To address these unavoidable defects caused by low-temperature solution-based processing methods, we studied different materials and concepts with the goal of developing feasible solutions to these issues. Among different passivation strategies, incorporation of the low dimensional phase (LDP) into the 3D MAPI structure is a rational approach, and 3D/LDP mixed dimensional PSCs are fabricated to neutralize the defects occurring in the perovskite structure.

Firstly, our research focused on developing and applying a novel thiophene-based organic spacer, ThPyI, with a heterocyclic structure in perovskite solar cells. A new thiophene-based ThPyI organic spacer with a heterocyclic structure was created and used as both a defect passivator and an organic spacer in surface- and bulk-passivated 3D MAPI-based perovskite devices. Our findings show that the ThPyI organic spacer is a viable option for producing 1D perovskitoids in perovskite-based solar cells. TRPL results indicated that the fluorescence lifetimes in both passivated devices increased, contributing to improved performance. Furthermore, ThPyI-based perovskite devices outperformed their 3D counterparts in terms of efficiency and environmental stability. Bulk-passivated 3D PV devices demonstrated much improved environmental and light-thermal stability when compared to surface-passivated devices. Importantly, this unique organic compound significantly triggered the preferential orientation of the 3D perovskite slabs' crystalline orientation (vertical orientation of the (110) planes with respect to the substrate) in the films compared to the MACl additive. This study contributes to the literature on thiophane-based organic spacers and offers a new perspective on organic spacer design. We believe that the above findings will contribute to the development of a logical method for the design of organic agents that serve numerous functions as defect passivators, crystalline orientation promoters, and organic spacers in diverse perovskite-based solar cells.

Then, fluorine-functionalized organic spacers (2F, 3F, and 5F) were successfully implemented to minimize defects and produce mixed-dimensional 3D/LDP MAPI perovskite devices. Dipole moment research (evaluation) reveals how fluorine atoms influence the properties of molecules. Dipole moment study demonstrates the impact of fluorine atoms on molecular

properties. Considering both full and partial coverage, we computed the *Eb* of these chemical structures on the Pb-I terminated perovskite surface. Our DFT results show that the stability and efficiency of MAPI-based solar cells are enhanced by fluorine-functionalized organic cations. The immobilization of fluorine-containing molecules on surfaces, as well as the passivation of exposed Pb bonds by these organic cations, significantly improve the endurance of perovskite- based solar cells. The efficacy of the passivating molecules and LDP was established by SSPL and TRPL analysis, which revealed potential reductions in non-radiative recombination losses in treated films. CL analysis was used to provide a more complete understanding of the emission properties of both untreated and treated perovskite films. Although the 3D control showed emission from both MAPI and excess PbI_2, the treated films that formed LDP showed non-emissive qualities from the agglomerates while emitting a signal from the 3D MAPI. Additional experiments employing XRD, GIWAXS, and HR-TEM revealed LDP structures. These studies of treated films revealed variations in crystallinity and surface composition. These findings provide light on the complex relationship between surface morphology, molecular structure, and optoelectronic properties in PSCs, giving critical information for optimizing and increasing device performance. This study brings up new possibilities for developing organic spacers to reduce the consequences of defects in 3D/LDP PSC.

6. PUBLICATIONS

A Novel Multi-Functional Thiophene-Based Organic Cation as Passivation, Crystalline Orientation, and Organic Spacer Agent for Low-Dimensional 3D/1D Perovskite Solar Cells

Ali Semerci, Ali Buyruk, Saim Emin, Rik Hooijer, Daniela Kovacheva, Peter Mayer, Manuel A Reus, Dominic Blätte, Marcella Günther, Nicolai F Hartmann, Soroush Lotfi, Jan P Hofmann, Peter Müller-Buschbaum, Thomas Bein, Tayebeh Ameri, *Advanced Optical Materials*, **2023**, 2300267.

The Role of Fluorine-Functionalized Organic Spacers for Defect Passivation and Low-Dimensional Phase Formation in 3D MAPI Perovskite Solar Cells

Ali Semerci, Javier Urieta-Mora, Sander Driessen, Ali Buyruk, Rik Hooijer, Agustín Molina-Ontoria, Bülent Alkan, Seckin Akin, Mattia Fanetti, Harishankar Balakrishnan, Achim Hartschuh, Shuxia Tao, Nazario Martin, Peter Müller-Buschbaum, Saim Emin, Tayebeh Ameri, Manuscript in preparation